UNIVERSITY
OF TRENTO - Italy
DEPARTMENT OF INDUSTRIAL ENGINEERING

XXXIV cycle

Doctoral School in Materials, Mechatronics
and Systems Engineering

Additively Manufactured β – Ti Alloy for Biomedical Applications

Alireza Jam

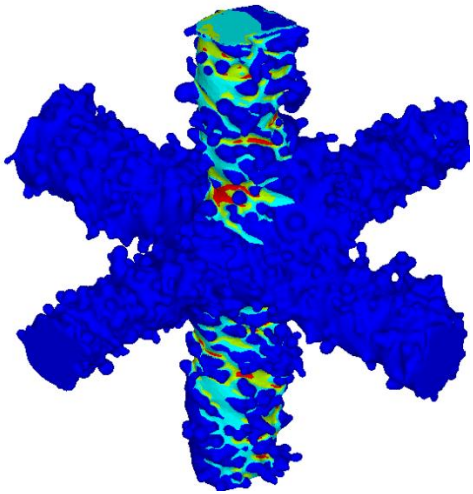

January 2022

ADDITIVELY MANUFACTURED BETA–TI ALLOY FOR BIOMEDICAL APPLICATIONS

Alireza Jam

E-mail: alireza.jam@unitn.it

Approved by:

Prof. Massimo Pellizzari, Advisor
Department of Industrial Engineering
University of Trento, Italy.

Prof. Matteo Benedetti, Advisor
Department of Industrial Engineering
University of Trento, Italy.

Ph.D. Commission:

Prof. Chao Gao,
Department of Mechanical and Industrial Engineering
Norwegian University of Science and Technology, Norway.

Prof. Maurizio Vedani,
Department of Mechanical Engineering
Polytechnic University of Milan, Italy.

Prof. Alberto Molinari,
Department of Industrial Engineering
University of Trento, Italy.

University of Trento,
Department of Industrial Engineering

February 2022

University of Trento - Department of Industrial Engineering

Doctoral Thesis

Alireza Jam - 2022
Published in Trento (Italy) – by University of Trento

To my parents

Abstract

Metallic biomaterials have an essential portion of uses in biomedical applications. Their properties can be tuned by many factors resulting in their process tuneability. Among metallic biomaterials for biomedical and specifically orthopedic applications, titanium and its alloys exhibit the most suitable characteristics as compared to stainless steels and Co-Cr alloys because of their high biocompatibility, specific strength (strength to density ratio), and corrosion resistance. According to their phase constitution, Ti-alloys are classified into three main groups, namely α, β and $\alpha+\beta$ alloys. Depending on the degree of alloying and thermomechanical processing path, it is possible to tune the balance of α and β phases, which permits to tailor properties like strength, toughness, and fatigue resistance. ($\alpha+\beta$) Ti alloys, especially Ti-6Al-4V, are widely used alloys in biomedical applications; however, they have some drawbacks like the presence of toxic elements i.e., V and relatively high elastic modulus to that of bones. In view of the lower elastic modulus of body center cubic β phase (50GPa<E<100GPa) compared to the $\alpha+\beta$, as well as due to their good mechanical properties, excellent corrosion resistance, and biocompatibility, β-Ti alloys have been recently proposed as a valid alternative to $\alpha+\beta$ ones.

The growing interest in additive manufacturing (AM) techniques opens new and very interesting perspectives to the production of biomedical prosthetic implants. AM will prospectively allow implant customization to the patient and produce it on demand, with large savings on times and costs. Moreover, AM is gaining increasing interest due to the possibility of producing orthopedic implants with functionally graded open-cell porous metals. The main advantages of porous materials are the reduction of the elastic modulus mismatch between bone and implant alloy reducing the stress shielding effect and improving implant morphology providing biological anchorage for tissue in-growth.

In this scenario, *the first goal* of the present PhD thesis work was *to identify a high-performance β-Ti alloy formulation suitable to Laser- Powder Bed Fusion (L-PBF) additive manufacturing*. In particular, it explores the potential use of a β-metastable Ti alloy, namely Ti-15Mo-2.7Nb-3Al-0.2Si (Beta Ti21S, 21 wt.% of alloying additions, including Silicon) for biomedical applications. Through microstructural, mechanical, and cytotoxicity analyses, it could be shown that this alloy grade exhibits i) an unprecedented ultra-low elastic modulus, ii) improved cytocompatibility due to the lack of Vanadium, and iii) no martensitic transformation responsible for hard and brittle solidification structures.

A second goal was *to assess the manufacturability of metamaterials made of β-Ti21S via L-PBF*. For this purpose, cubic cellular lattice structures of different unit cell sizes (and therefore different strut thickness) have been fabricated and characterized

through microstructural analysis using different techniques, and computed tomography combined with linear elastic finite element simulations to identify the minimum cell size that can be printed with adequate dimensional and geometrical accuracy. Samples of the selected unit cell size were also tested to determine their static and fatigue properties. The main results show that i) the suitable manufacturing quality is obtained for strut thickness above 0.5 mm, ii) the mechanical tests place the present cellular structures among the best stretching dominated cellular lattice materials investigated to date in the literature, and iii) the fatigue tests showed a normalized fatigue strength at 10^7 cycles of close to 0.8, similar to cubic lattices made of Ti-6Al-4V, and higher than most cellular structures in the literature. In the last part of the thesis, a more complex *octet truss* structure was fabricated in the manufacturable cell size, and its mechanical properties were investigated. The octet truss topology can be beneficial both in terms of mechanical properties and biocompatibility by providing the different types of porosity suitable for bone in-growth.

Table of Contents

List of Figures

List of Tables

Chapter Ⅰ
Literature review

1.1 Introduction

In this chapter, the nature of biomaterials and their main requirements are described. The bone structure, the main types of implants, and the main challenges in achieving an ideal bone substitute are presented. The types and properties of biomaterials are presented. This literature review is focused on metallic biomaterials, especially on the beta-Ti alloys. The additive manufacturing (AM) of metallic biomedical components is discussed focusing on laser powder bed fusion (LPBF) of bulk and cellular metallic materials.

1.2 Biomaterials Need

An ideal performance of human tissue and organs flunk due to disorders, i.e., genetic makeup, age, sickness, or accident. Several minor ailments are healed using drugs, by stimulating the bioactive agents. In some cases, however, the use of materials and devices is vital to treat the illness. For example, depending on the level of bone fracture after a car accident, the surgent decide the healing process either by fixture supporting or by replacing the broken bone. The elderly population (over 65 years old) is growing by 2-3% per year, albeit the total population over the world is decreasing (Figure 1-1). In addition, to increase the life expectancy the humankind has tried to search for materials and tools. This has been achieved either by discovering the instrument and material from nature or synthesis of them to use it in the same way (Hanawa 2010).

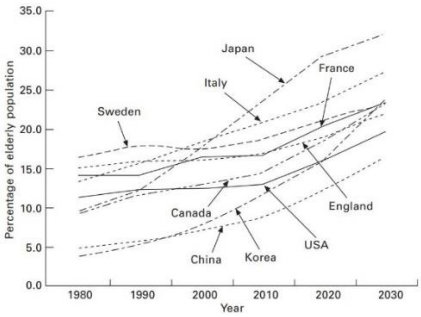

Figure 1-1 : Change and estimation of elderly (over 65 years old) population (Hanawa 2010).

1.3 Definition of Biomaterial

The human body was named *"the symbol of harmony"* by Marcus Vitruvius Pollio, a Roman architect and engineer. He described the human body as a system in which the parts are in harmony with one another. The Vitruvian Man diagram (Figure 1-2) drawn by Leonardo da Vinci is often indicated as the symbol of this harmony. In this context, biomaterial scientists are strikingly attempting to extend this harmony between the natural organs and their artificial counterparts (Naini et al. 2008).

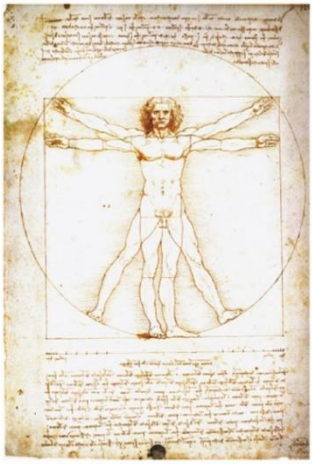

Figure 1-2 : The Vitruvian Man diagram was drawn by Leonardo da Vinci (Naini et al. 2008)**.**

The natural or synthetic materials used to support or take charge of the function of damaged or diseased human body parts are named *biomaterials* ("Biomaterials and Biomedical Materials" 2019). Nowadays, good biomaterials have increased life expectancy and improved life quality. The ever-increasing interest and investment in the biomaterial-development is thus not surprising.

The earliest evidence of prosthetics' is difficult to be proven, as many societies had no transcribed documents and those biomaterials had been in use without being systematically traced. To date the first biomedical usage, one may rely on anthropologists and archaeologists to decode the myths, artworks, and remains. The clear applications of biomaterials date to years BC. The limb and foot, arm and hand, trepanation, ocular, and skull (Figure 1-3) prostheses are examples of discovered biomedical implants (Goguitchaichvili et al. 2017; Naini et al. 2008). The success rate of implantation was quite low due to lack of sterilization leading to the infection and gangrenous, thereby revision surgery was required. Joseph Lister, around the 1870s,

highlighted the non-trivial role of sterilization through the operating theaters. The surgical treatment, thereafter, became more successful (Ladino, Hunter, and Téllez-Zenteno 2013). Sir Jon Charnley designed the initial hip implant headed femoral stem and cup of Teflon at Wrightington Hospital in 1962. In practice, this first experiment was not successful. He improved the lasting time of implant to 10-15 years by changing the material to ultrahigh molecular weight polyethylene (UHMWPE) (Basu, Katti, and Kumar 2009).

Figure 1-3 : Trepanned Inka skull closed with a gold plate showing bone reconstruction and osseointegration. Museo del Oro, Lima (Naini et al. 2008)**.**

1.4 Biocompatibility

There are specific requirements and properties to be fulfilled by a material candidate to become a biomaterial, *in primes* it must be biocompatible. Biocompatibility is a condition met by a biomaterial or medical tool typically based on the tissue response. The biological behaviors comprise of tissue reaction are influenced by implant-related factors, including (Anderson 2011):

1- The dead space formed by the presence of the implant;

2- Soluble agents released by the implant (e.g., ions or molecular fragments);

3- Insoluble particulate material released from the implant (e.g., wear debris);

4- Chemical interaction of biological molecules with implant surface;

5- Alternations in the strain distribution in tissue due to the mismatch in modulus of elasticity between the implant and surrounding tissue, or the

movement of the implant relative to adjacent tissue because of the absence of mechanical coupling.

In addition to the biocompatibility factors, the biomaterial needs to fulfill various requirements, e.g., to have physical and mechanical properties similar to those of the tissue it replaces or is implanted in, should be easily processable, sterilizable, and to be economical and available (Basu, Katti, and Kumar 2009).

1.5 Types and properties of biomaterials

Biomaterials can be obtained from (1) natural materials, (2) synthetic polymers, (3) ceramics, (4) metals, and (5) composites.

The natural materials are deemed as biological polymers and decellularized tissue. The biopolymers are of plants (cellulose), animals (collagen), insects (silk), microorganisms (polyesters), crustaceans (chitosan), and algae (alginate) origin. Their properties are highly controlled since they are made of organisms and enzymes. They are derived from in-expensive sources and are considered biodegradable biomaterials. They cannot be used for most load-bearing applications since they do not provide sufficient strength and stiffness. Given the similar chemistry and mechanical properties, they are a suitable candidate to be used in biological systems. Soft tissue replacement wound dressing, and cartilage substitutes are of those crucial functions (Anderson 2011). Synthetic polymers are also poorly suitable for load-bearing applications. In essence, they are hydrophobic (e.g., PMMA, PVC, Teflon, Dacron, PE), and thus their properties are not comparable with the biological tissues and biopolymers. They are well known as non-degradable materials and can be used in scaffolds for tissue engineering applications. Typically, the polymeric materials (polymeric as either biological or synthesis) can be easily processed into intricate shapes, which is an important benefit in comparison to other biomaterials. In some critical cases, the hard tissue experiences long-term repeated loading. The polymeric biomaterial should be tough enough to resist under this kind of loading. Not cross-linked polymers collapse, whilst the cross-linked ones show higher strength and a linear elastic behavior, like metals. Soft tissue implant, drug delivery systems, contact lenses, bone plates, bone cement, dental filling, and tissue are some typical applications (Chandra Biswas et al. 2021; Kumar Sadasivuni et al. 2019)

Ceramics materials are chemically not degradable nor active. They are characterized by strong covalent bonding which make the hard, brittle, poor heat and electrical conductors, i.e., suitable candidates for bone tissue replacement. In particular for the components like the tooth crown where they are being subjected to the compressive force during chewing and sudden alteration of temperature during eating. Unfortunately, their processing conditions are not mild, and therefore their application is limited (Huang and Best 2007).

Metallic biomaterials are widely used in biomedical applications. Their properties can be modulated in a relatively wide range and, in most cases, they can be also conveniently manufactured. They are crystalline materials with metallic bonds, giving them the capacity to withstand a variety of loading conditions namely, tensile, compressive, shear stress, impact and cyclic. Certainly, no other type of biomaterial could do that. Metals are suitable for orthopedic and dental applications (e.g., bone replacement, knee, joint, screw, pins). Metallic bonding also provides good electrical and thermal conductivity, which can be used for signal-conducting medical devices in implanted sensors and pacemakers. On the other hand, metals are prone to oxidation and are nearly reactive. For instance, limited corrosion resistance and grain boundary ion releasing can limit their application. Some metallic materials, as Ti and its alloys, passivate, i.e., they form a thin and compact oxide layer, which acts as a protection barrier against oxidation, corrosion, and ion releasing (Kuhn 2005).

Composites consist of two or more materials that establish a unified structure by merging the properties of its elements to deliver a much-improved product. Human tissues such as bones, tendons, skin, ligaments, teeth can be also categorized as composite. Composites exhibit properties not achievable by its constituents' materials. Human-made composites can be strikingly used to mimic biological tissues. In addition, they can be designed flexibly since their structure and properties are customized for specific applications. Heart valves of pyrolytic carbon-coated graphite, carbon fiber-reinforced bone plates or tendons, and hydroxyapatite-coated hip implant are several cases of biomedical composites. The latter case is a decent composite biomaterial that can meet the bone replacement requirements because the bioceramic coating on the metallic body has a composition similar to the mineral component of the bone, thus ensuring good biocompatibility (Salernitano and Migliaresi 2003).

One of the main applications of the biomaterial is the bone replacement. To figure out the best candidate materials for this substituting, understanding the bone composition, structure, and properties is of critical importance. The bone is a natural composite material consisting of organic components (collagen and fibrillin) and inorganic crystalline minerals (e.g., hydroxyapatite, HA) (S. Wu et al. 2014; X. Wang et al. 2016). The HA provides strength, while collagen delivers flexibility. The unprecedented mechanical properties of bone are related to its hierarchical structure (shown in Figure 1-4). Each level of the structure plays diverse mechanical, biological, and chemical functions. The bone can be categorized as i) compact (cortical bone) and ii) trabecular (cancellous bone). The former is nearly dense with only 3-5% open spaces while the latter one has a porosity that varies between 50 and 90% (Rho, Ashman, and Turner 1993a). The compact bone is made of osteons in ranging 4 sizes of 10 to 500 μm; the porous network of trabeculae is the submodel of the

trabecular bone. At the micron- and nano-scales, aggregated collagen, and HA create the collagen fibril, whose role is likely linked to bone remodeling. The collagen fiber reinforced with HA is a building element for both compact and trabecular bones.

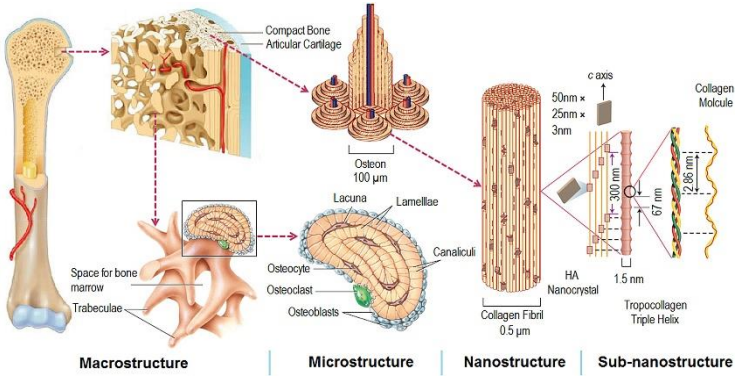

Figure 1-4 : Bone structure (Wegst et al. 2015)**.**

The cortical bone thickness, density, and pore structure of trabecular bone may differ by location in the human body and even inside each part of the bone, depending on the local necessity. The trabecular bone is denser near the joint due to differing mechanical load requirements (strength and angles of loading), while the trabecular bone is less dense and less isotropic (more directionally aligned) in the middle of bone (Endo et al. 2016). Such complex structure is displayed in Figure 1-5 using the micro-CT image of different regions within femur bone and should be carefully considered designing the implant to mimic the bone structure. This is typically achievable by the freedom in the fabrication of the lattice structures.

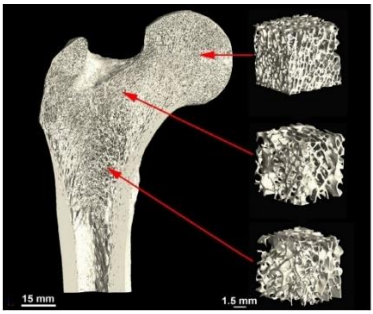

Figure 1-5 : Variation of trabecular bone structure by location, from human femur 26-year-old male (Yadroitsava, du Plessis, and Yadroitsev 2019).

Mechanical properties of the bone differ with age, anatomical feature, and bone quality. Elastic modulus property has drawn the greatest attention of researchers due to its essential significance. However, attention has been paid also to other biomechanical bone properties like strength, creep, and fatigue resistance. Anisotropic behavior in mechanical properties can be seen for both compact and trabecular bones. Compact bone is stronger and stiffer under longitudinal loading along the diaphyseal axis than radial transverse directions (Table 1-1). Trabecular bone shows time-dependent performance as well as damage susceptibility during cycling loading. Its biomechanical properties are dependent on porosity and architectural arrangement of the unit trabeculae. Both types of bone are stronger under compression than under tension (Sharir, Barak, and Shahar 2008; Rho, Kuhn-Spearing, and Zioupos 1998; Rho, Ashman, and Turner 1993b; Choi et al. 1990; Wegst et al. 2015).

Table 1-1. Biomechanical properties of human bones (X. Wang et al. 2016)**.**

Bone	Porosity	Modulus (Gpa)		Strength (MPa)		Poisson's ratio
Compact	3-5%	Longitudinal	17.9 ± 3.9	Tension	135 ± 15.6	0.4 ± 0.16
				Compression	205 ± 17.3	
		Tranverse	10.1 ± 2.4	Tension	53 ± 10.7	0.62 ± 0.26
				Compression	131 ± 20.7	
		Shear	3.3 ± 0.4	shear	65 ± 4.0	
Trabecular	Up to 90%	Vertebra	0.067 ± 0.045		2.4 ± 1.6	
		Tibia	0.445 ± 0.257		5.3 ± 2.9	
		Femur	0.441 ± 0.271		6.8 ± 4.8	

Bone regeneration capability should be also considered as a biomaterial prerequisite since the implant must attach to the existing bone (D. F. Williams 2008). This can be also named *osseointegration*, the direct structural and functional connection between living bone and the surface of a load-bearing artificial implant. Bone regeneration (osseointegration) can be achieved by three processes: osteogenesis, osteoinduction, and osteoconduction. Osteogenesis is the process of bone transforming undifferentiated mesenchymal cells into osteoblasts and the formation of ectopic bone in vivo. Osteoconduction is the process of bone growth on bioinert or physiological matrices, providing new cell colonization, bone in-growth, and blood vessel formation (vascularization) (Hasan et al. 2018).

The bone may form by two different processes: contact and distance osteogenesis. An ideal replaced biomaterial should stimulate bone formation by facilitating high vascularization and direct osteogenesis, the osteochondral

ossification should be promoted as well (Lawrence E. Murr 2019). Since these processes are directly dependent on the surface, the surface topography of the implant is of importance. The surface patterning varies the topology of the implant surface, impacts on the osteoblast adhesion, differentiation, orientation, and final osseointegration (Cheng et al. 2014; M. Wang et al. 2016a). It is worth mentioning that depending on the fabrication method of implants the surface pattering can be turned to the desired level. However, there is general agreement about the optimum surface pattern.

1.6 Metallic biomaterials

1.6.1 Why metal?

Metallic biomaterials have been utilized broadly for surgical implants, approximately 70% of the materials utilized in the implants are metallic. The unique mechanical properties of metallic biomaterial (high strength, and resistance to fracture) offer reliable long-term implant performance in load-bearing conditions such as those experienced in specific orthopedic and dental implant applications. The valuable properties of metallic biomaterials are rooted in their interatomic bonding and their atomic arrangement. Physical and mechanical properties are related to the microstructure which is determined by the metal processing procedures. The insight into properties and processes used to attain these properties is crucial for reaching the favorable performance of implants. They are also characterized by relatively easy, well-established, and largely available fabrication processes (e.g., casting, forging, and machining). More recently, manufacturing techniques like additive manufacturing have pushed the use of metallic biomaterial in the fields of orthopedics, density, and cardiovascular surgery.

A cement-less permanent implant must last for decades and approximate the area of a replaced body part in terms of physical and mechanical properties. The metallic biomaterial must strongly bond to the bone in the early months following implantation, to guarantee that the full osseointegration in the subsequent months follows properly. Osseointegration is defined as the mechanical interlocking process through a linkage between the surfaces of implant and bone. Full host to the implant contact is obtained by the development of an anchorage mechanism that could tolerate natural loading, and therefore the surface features of implants are of interest at various steps of the osseointegration process (Linder et al. 1988; Holzapfel et al. 2013).

1.6.2 Types and properties of metallic biomaterials

The major benefits of the metals compared with ceramics and polymers are generally their higher strength and fracture resistance in high loading conditions. They have an acceptable combination of mechanical and physical properties very useful in the biomedical field. They can be replaced mostly for the function of hard tissues in

orthopedics. Bone fixators, artificial joints, external fixators are such an example of metallic biomaterials. They are being used also as stents and stent-grafts for inserting into the stenotic blood vessels for dilatation due to their high elasticity or plasticity for expansion and rigidity for maintaining dilatation (Wilson 2018). In dentistry, metals are used for orthodontic wire and dental implants. Corrosion resistant metals (e.g., stainless steel, cobalt-chromium-molybdenum alloys, titanium alloys) are very suitable due to their high stability in aggressive environment. For the same reason, noble metals and related alloys (gold and silver alloys) are also used in the dentistry field.

As noted in previous sections, the elastic modulus of biomaterial should match as much as possible that of bone (Table 1-1). Any discrepancy causes a disproportionate share of the load on the implanted biomaterial. Therefore, the real load experienced by the bone will be proportionally lower due to the physical phenomenon known as *stress shielding* (Ibrahim et al. 2017). Under this load distribution condition, the deterioration of the bone quality occurs, leading to the bone thickness decrease, bone mass loss, and osteoporosis (bone resorption), hence the bone loosening occurs eventually. It is essential to understand the definition of elastic modulus and how it can be reduced to a closer value, matching that of bone.

The microstructure is created from crystallites with the same or different crystallographic orientation, named single and poly crystal, respectively. The macroscopic properties of polycrystal can be assumed isotropic when the crystal orientation is random. This is not the case for the material with the continuous crystal lattice or material with a strong morphological texture. For instance, the unique crystal possesses anisotropic behavior in terms of elastic deformation regarding the crystal orientation. When a considerable percentage of crystals is oriented along the preferential direction, the crystallographic texture arises, and it exerts an important influence on the elastic deformation (Callister William D. 2004). The most evident is an anisotropic behavior, which can be useful in applications in which the applied load is uniaxial (e.g., sheet metal) but is harmful in structural applications undergoing multiaxial loading (e.g., implant). Crystalline materials are formed by crystal structures showing peculiar atom arrangement, packing and equilibrium interatomic spacing. Under equilibrium conditions, the net interatomic forces on atoms are zero, as the result of balance between attractive and repulsive force (Figure 1-6). The interatomic force-distance relation is the intrinsic material characteristic. Therefore, applying a stress to the material can represent the unique reaction response of the material. This reaction response can be characterized through the elastic region of the stress vs. strain curve. In this region, the elastic modulus (the slope of the elastic region) is tightly correlated to the atomic bonding energy of crystalline alloys. Thus, it changes with the crystallographic structure of phases and also with the texture of alloys.

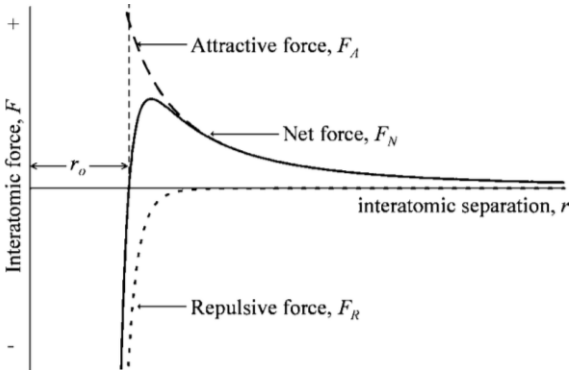

Figure 1-6 : Interatomic force vs. interatomic separation curve (Callister William D. 2004)**.**

1.7 Titanium for biomedical applications

Ti and its alloys were initially designed for the aerospace industry and have also been increasingly used for medical implants because they present good physical (e.g., density) and mechanical (e.g., high specific strength) properties. Similar to aluminum, they form the stable ceramic oxide layer on their surface protecting them from corrosion better than stainless steel and Co-Cr alloys. The lower elastic modulus (100-110 GPa) compared to stainless steel and Co-Cr alloys (200-220 GPa), make them a suitable candidate for bone fixators applications. Ti alloys can also contain fewer toxic elements (depending on the specific Ti alloy grade), which should not reduce osseointegration or introduce cytotoxicity but, in general, they have better biocompatibility compared to their steel counterparts (Narayan 2012).

1.7.1 Pure Ti

At room temperature pure Ti is composed of hexagonal close-packed (α-phase) crystals, while above 883 ºC (the β-transus temperature) it shows a body-centered cubic (β-phase) crystal structure (Kolli and Devaraj 2018). Pure Ti is not present in nature, because it is a highly active element which easily dissolves elements like oxygen, carbon, and nitrogen. Titanium comprising of these impurities is known commercially pure Ti (CP Ti). Depending on the impurity content, CP Ti is classified into four grades (Table 1-2).

Table 1-2. Compositions of commercially pure titanium (Hanawa 2010)**.**

	Grade 1	Grade 2	Grade 3	Grade 4
Element		Composition (mass%)		
Fe	< 0.15	< 0.2	< 0.25	< 0.3
O	< 0.18	< 0.25	< 0.35	< 0.45
N	< 0.03	< 0.03	< 0.05	< 0.05
H	< 0.0125	< 0.0125	< 0.0125	< 0.0125
C	< 0.1	< 0.1	< 0.1	< 0.1
Ti	Balance	Balance	Balance	

A higher-grade number indicates a higher impurity content, which leads to higher tensile strength, hardness, but lower elongation to fracture (Figure 1-7). Depending on the specific impurity level, properties can vary in a considerable way. Ti alloys can be distinguished from CP-Ti due the higher amount of alloying. Maxillofacial prosthetic plates, sternal wire, dental implants, dental restoratives, and dental bases are only some applications of CP Ti in the biomedical section. For some of them, the mechanical properties of CP-Ti can be improved also by cold working: for instance, bone screws exposed to heavy loads are sometimes made of cold forged CP-Ti. It was also recently used in cellular strictures because of the good ductility, necessary for load-bearing orthopedic implants (Kolken et al. 2021a).

The major drawback of CP-Ti is its poor wear resistance important for some biomedical applications like load-bearing articulating surfaces, and hence limits the application of CP-Ti. This can be improved through surface modification to obtain better wear resistance e.g., ion implantation with N^+. The hard TiN film on the surface of the implant can be deposited using physical vapor deposition (PVD). In addition, CP-Ti can be used in the modular implant design, for instance, in Figure 1-8 the modular hip implant is designed for this purpose. In such case, the wear resistant bearing component is made of either Co alloy, ceramic (Al_2O_3, Phase Stabilized ZrO_2), or a ceramic surface-layered alloy (ZrO_2/Zr-Nb), and the stem shaft is typically made of either CP Ti or high strength Ti alloy to have a combination of good wear resistance and good fatigue strength.

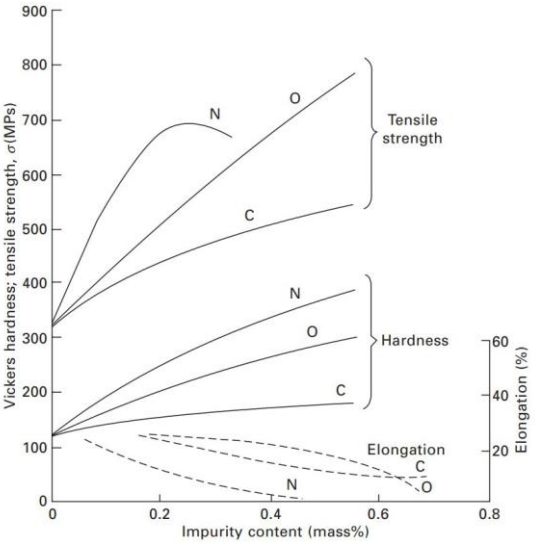

Figure 1-7 : Mechanical properties of CP Ti with varying impurity content (Hanawa 2010).

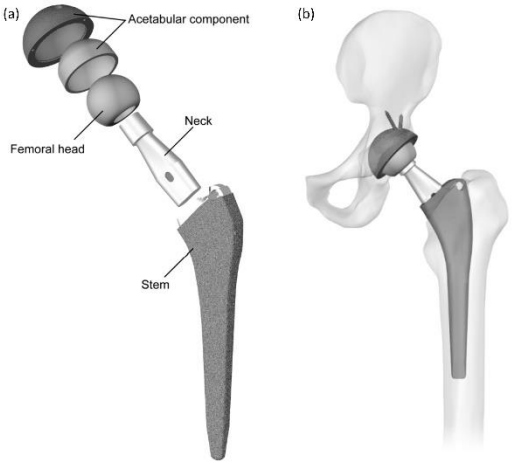

Figure 1-8 : Modular Hip Prostheses (a) and the inserted implant into the bone (Affatato 2014).

1.7.2 Ti alloys

Ti alloys are classified according to the type and amount of alloying elements: depending their influence on the on the β-transus temperature they can be classified as neutral, α-stabilizer, or β-stabilizers (Figure 1-9). Neutral elements (i.e., Sn and Zr) do not significantly affect the β-transus temperature; they are used as additives in β-metastable Ti alloys to reduce the kinetics of hexagonal ω-phase formation during the aging heat treatment. The α-stabilizing elements expand the α phase region to higher temperature whereas the β-stabilizing elements shift the β-phase field to the lower temperature. The α-stabilizer elements (i.e., Al, O, N and C) develop the α+β field; among the α-stabilizer elements, Al is the most effective one. The cumulative amount of α stabilizer is defined by the "*equivalent aluminum {Al}*" weight percent content (Campbell 2008):

$$\{Al\} = Al + 0.3Sn + 0.16Zr + 0.1(O + C + 2N) \quad (1)$$

If the {Al} exceeds 9 wt% it leads to the formation of the brittle intermetallic compounds like Ti_3Al, leading to ductility reduction. This has led to adding more alloying elements, to suppress this formation and to stabilize the β-phase.

The β-stabilizing elements are subdivided into *β-isomorphous* and *β-eutectic*. Mo, V, and Ta belong to the β-isomorphous group, because of their high solubility in Ti. In a similar way, the equivalent molybdenum {Mo} is defined as

$$\{Mo\} = Mo + 0.67V + 0.44W + 0.28Nb + 0.22Ta + 2.9Fe + 1.6Cr - Al \quad (2)$$

Formation of the intermetallic compound is highly possible by introducing very low volume fractions of β-eutectic elements, e.g., Fe, Mn, Cr, Co, Ni, Cu, Si, and H.

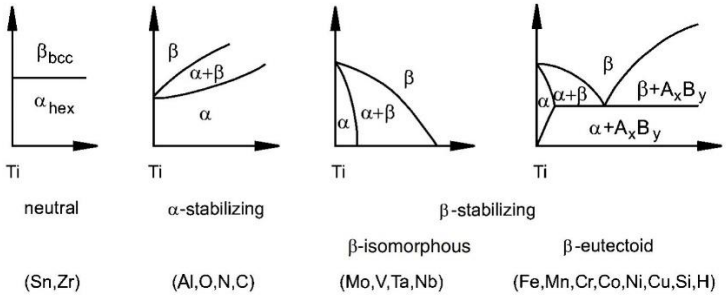

Figure 1-9 : Influence of different alloying elements on phase stability of Ti alloys (Peters et al. 2003)**.**

Generally, Ti alloys are categorized as α, α+β, and β alloys. A further subdivision can be found also in the literature considering also near-α, near-β and metastable β alloys whose compositions place them near the α/(α+β) or (α+β)/ β phase field

boundaries, respectively. Nishimura et al. (Nishimura, Nishigaki, and Kusamichi 1982) have mapped (Figure 1-10) the locations of a series of technical alloys along the abscissa of a "β-isomorphous" binary alloy phase diagram. Their position along the abscissa is controlled by the concentration of β-stabilizers.

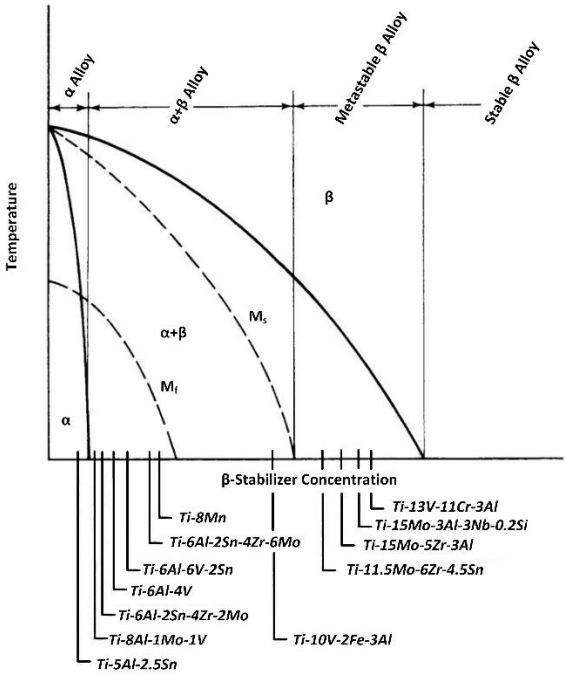

Figure 1-10: Composition of some selected technical Ti alloys mapped onto a pseudobinary β-isomorphous phase diagram (Nishimura, Nishigaki, and Kusamichi 1982).

1.7.3 (α+β) Ti alloys

The α+β alloys are so far the most widely used. These alloys possess higher strength compared with CP Ti, superior corrosion resistance and osseointegration properties.

Many kinds of (α+β) Ti alloys have been established so far but the famous ones, categorized in the ASTM and ISO standards, are Ti-3Al-2.5V, Ti-5Al-2.5Fe, Ti-6Al-7Nb, and Ti-6Al-4V. The last one, accounting for about 65% of all Ti alloys, is the most used also in the biomedical field. This alloy presents good workability, heat treatment ability, and weldability, as well as good corrosion and fatigue resistance. Decreasing the number of interstitial elements (Oxygen, Carbon, Nitrogen, and

Hydrogen) to a minimal amount, allowed to develop the Ti-6Al-4V Extra Low Interstitial (ELI) grade. This alloy shows great toughness and fatigue strength, suitable for biomedical field.

The mechanical properties of the Ti-6Al-4V alloy, fatigue strength mainly, are strongly related to the size and distribution of the α and β phases (Cao et al. 2020). Thermomechanical and heat treatments affect the distribution of the phases. A microstructure consisting of small equiaxed α grains surrounded by fine β-particles can be obtained after a rolling-annealing treatment. In this method, the alloy mechanically work-hardened to the needed shape at temperature just below the β-transus and subsequently rapidly quenched to room temperature to form α' martensite. The annealing in the intercritical α+β region further recrystallize the structure, transforming the martensite into equilibrium α phase. Through this process, the α phase with the retention of some β phases is formed with the unique distribution (α-lamellae separated by β-lamellae), leading to better mechanical properties when compared to the non-heat treated microstructure.

The Ti-6Al-4V alloy is considered cytotoxic, mainly due to the presence of V. Therefore, the Ti-6Al-7Nb alloy has been developed with no toxic element V , which is mostly used in Europe. Ti-6Al-7Nb has the same atomic concentration of Ti-6Al-4V, but V is replaced by Nb. Improved corrosion resistance and biocompatibility are the main advantages of Ti-6Al-7Nb compared to its counterpart. Ti-6Al-2.5Fe has been also developed in Europe for this purpose. Even if many types of alternative alloys are emerging, Ti-6Al-4V alloy is still being mostly used in the biomedical field: it is named the “golden alloy” because of its reliability, properties tunability, and availability around the world.

1.7.4 β-Ti alloys

These alloys are getting growing attention in the last decades due to their unique properties. Their microstructure complexity provides the appropriate strength-toughness combination for many applications (Bania 1994; Boyer and Briggs 2005; Cotton et al. 2015). The introduction of beta alloys allowed an important reduction of production cost in some specific applications. The bcc structure of β-phase shows a larger number of slip planes than hcp structure of α-phase. This contributes in reducing the flow stress, thus allowing plastic deformation at lower temperatures, hence resulting in cost savings. These alloys can be processed even at ambient temperature. The enhanced forgeability of β-Ti alloys also favored the substitution of Ti-6Al-4V alloy because of the ease in achieving near net shape and higher tolerance with the lower necessity of machining. The capability to undergo large plastic deformation enables large size reduction during rolling, so that beta alloys can be fabricated on large scale with lower costs in form of sheets and strips, especially for the aircraft industry. This type of alloys present good weldability as well. The high

percentage of alloying elements prevents severe segregation during welding. The high percentage of β-stabilizer also prevents the formation of any martensite, generally formed during high cooling rate processes (Baeslack, Becker, and Froes 1984).

The mechanical properties of the solution treated or work-hardened β-Ti alloys can be improved through aging. These are comparable and, in some cases, even higher than those of α+β alloys: the ultimate strength is in the range of 1400-1500 MPa, and under controlled laboratory conditions they could reach 1800-1900 MPa (Mantri et al. 2018). This strength associated with the low density of Ti (4.9 g/cm^3) leads to much higher specific strength compared to steels. Therefore, beta-Ti alloys can be used for the light-weighting applications. The heat-treated β-Ti alloys demonstrate higher yield and fatigue strength compared to the α-Ti and (α+ β) Ti alloys, as well (Huda and Edi 2013). For instance, the fatigue strength at 10^7 cycles for the β-Ti alloys is generally in the range of 400-700 MPa while for the α-Ti and α+β Ti alloys are in the range of 200-400 MPa. A higher β-transus temperature enables their use for high-temperature applications. Oxidation and corrosion resistance of β-Ti alloys are influenced by the type and percentage of alloying elements. Vanadium has a marked tendency to react with oxygen and also alloys containing high percentage of V are more susceptible to oxidation. On the other hand, Mo up to 15 wt.%, improves corrosion resistance especially when it is combined with noble metals such as Pt (Freese, Volas, and Wood 2001).

Compared to the (α+β) alloys, the major advantage of β ones for biomedical application is the lower elastic modulus, closer to that of bones. Mechanical properties of several β-alloys are reported in Figure 1-11. Of these, the Ti-15Mo-5Zr-3Al alloy has been specified for the wide used for biomedical applications. It should be noted that the low elastic modulus exhibited by Ti-29Nb-13Ta-4.6Zr can be only obtained introducing a high content of rare and expensive alloying elements, like Nb and Ta. This clearly explains why Ti6Al4V still represent the most popular and widely used Ti alloy on the market.

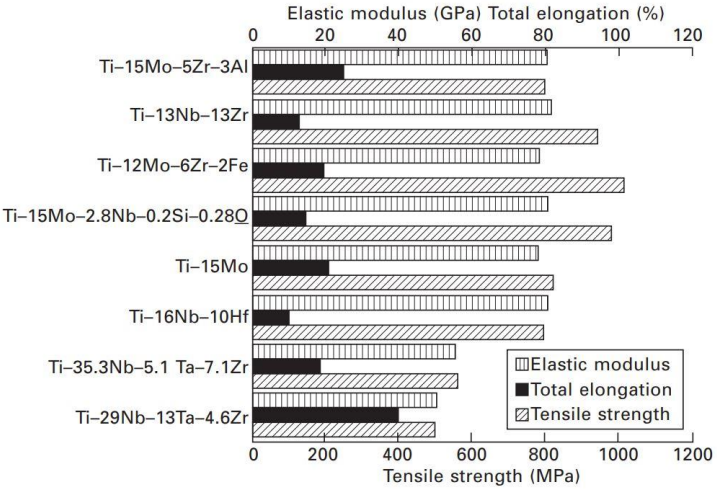

Figure 1-11 : Mechanical properties of some selected β-type titanium alloys (Hanawa 2010)**.**

Environmental conditions can dramatically reduce the predicted mechanical properties measured at room temperature. The human body represents a relatively steady environment. However, this environment can be influenced by changing the temperature, environmental chemistry, and pH caused by some diseases (e.g., inflammation and allergy). An implant surface exposed for long time to a corrosive environment causes a continuous and progressive degradation, which may lead to the loss of structural integrity. The formation of the passive layer in biomedical Ti and its alloy provides good corrosion resistance in various environments. The passive layer in Ti is mainly composed of TiO_2, and it is self-healing, i.e., it can easily reform if it's scratched off or even broken. This contributes toward keeping the mechanical properties of the implant as it is predicted and avoiding premature failure (L.-C. Zhang and Chen 2019). Numerous studies have investigated the corrosion resistance of biomedical Ti and its alloys (mainly CP-Ti, Ti-6Al-4V, and β-Ti alloys).Alves et al (Alves et al. (2009) studied the corrosion behavior of CP-Ti and commercially Ti-6Al-4V alloy in the Simulated Body Fluid (SBF) at room temperature and 37 ºC. They reported that temperature has a direct influence on corrosion resistance: corrosion rates of both materials were lower at 25 ºC. According to (Simsek and Ozyurek 2019), Ti-6Al-4V exhibits duct-shaped pits along the grain boundaries when exposed to SBF, which are deemed to be related to the dissolution of V-rich zones. The oral environment was found to be more detrimental for biomedical implants due to the greater availability of oxygen fluoride solution, and acidic foods. In this condition,

pitting corrosion is easier in Ti-6Al-4V alloy (Geetha et al. 2009). In a similar trend, the corrosion resistance of the β Ti alloy was investigated and widely compared with pure Ti and α+β alloy. (Bai et al. 2012) evaluated and compared the corrosion behavior of the CP-Ti, Ti-6Al-4V, and Ti-24Nb-4Zr-8Sn in simulated physiological environment. They concluded that the β-Ti alloy had a wider passive region and possess a lower corrosion current density, associated with the formation of the stable passive layer with the titanium and niobium oxides layer on its outer surface. Chui et al (Chui et al. 2020) studied the corrosion behavior of the Ti-Zr-Nb-Mo alloy containing different Mo content. Their result showed that the alloy with 15 wt.% Mo showed the lowest passivation current density of 2.31 ± 0.03 μA cm^{-2}. (Kumar and Sankara Narayanan (2009) studied the corrosion behavior of Ti-15Mo, CP-Ti, and Ti-6Al-4V in the Ringer's solution (9g/l NaCl, 0.24 g/l $CaCl_2$, 0.43 g/l KCl, and 0.2 g/l $NaHCO_3$, pH: 7.8). They observed that all alloys had good corrosion resistance while the Ti-15Mo alloy showed a stable passive film, which make it more suitable for biomedical applications. Lin et al (Lin et al. (2017)) manipulated the microstructure of Ti-40Ta-22Hf-11.7Zr by different solutions and aging heat treatments. The as-cast alloy was reported to have β+ω phase constitution. Annealing of this alloy at 900 ºC for 1 h resulted in the stabilization of the single β-phase structure. After aging at 300 ºC for 15 min, 1.5 h, 12 h, and 24 h, the β-phase progressively transforms into the β+α'', β+α''+α, and β+α+ω. These transformations resulted in distinct electrochemical behavior response during the electrochemical tests in Hank's solution. They reported that the solution-heat treated sample with single β-phase demonstrated the lowest current density of 0.49 ± 0.03 μA cm^{-2}. Adding noble elements to β-Ti alloy improves the corrosion resistance proposed by (Zareidoost and Yousefpour 2020). They separately added Fe, Sn, and Ag to the Ti-25Zr-10Nb-10Ta and reported that the Ag addition led to the best corrosion resistance in the Ringer's solution, due to the improved stability of the oxide film. On the other hand, the resistance to fretting-corrosion that occurs at the interface of two contacting surfaces due to small oscillatory movements in the presence of a corrosive medium is probably the most important for load-bearing implants (Simsek and Ozyurek 2019). This type of corrosion usually occurs at the junction of modular implants (i.e., hip) and is reduced by the formation of the protective oxide layer.

Among the different Ti alloys, the β ones demonstrated the best corrosion resistance. Anyway, attention should be paid to the possible precipitation of parasitic phases during heat treatment, since these can significantly reduce the corrosion resistance.

Apart from the mechanical properties and corrosion resistance of β-Ti alloy in the human body environment, the cytotoxicity of this alloy has been investigated in a few studies. Comparing the cytotoxicity of β-type Ti-26Nb and Ni-49.2Ti shape memory

alloys, the β-Ti alloy was found to be less cytotoxic due to the formation of calcium phosphate deposits within surface oxide layers of NiTi, the layer that affected the corrosion and biocompatibility (McMahon et al. 2012). In a similar study (Xue et al. 2015) compared the biocompatibility of Ti-19Zr-10Nb-1Fe and of NiTi. Ion release rates of β-Ti alloy were found to be much lower than that of Ni in NiTi; however, the cytotoxicity of both alloys was similar. Moreover, the Ti-19Zr-10Nb-1Fe exhibited a better hemocompatibility (compatibility of the material with blood) when compared with NiTi. Xie et al. 2013 fabricated the nanocrystalline Ti-36Nb-2.2Ta-3.7Zr-0.30O by high-pressure torsion processing. They pointed out that the enhanced in vitro biocompatibility was due to the increased fibroblast cell attachment and proliferation on nano-grained Ti alloy, which increased nano-roughness. The effect of nano-size α''/α/ω precipitates in the β matrix after heat treatment on the in-vitro biocompatibility of Ti-29Nb-14Ta-4.5Zr investigated by (Haftlang, Zarei-Hanzaki, and Abedi 2020). The polarization tests in the SBF showed the high tendency of appetite formation on the surface of β-matrix contained ω precipitates. The in-vitro test attested the >85% cell viability of the TNTZ alloy reinforced by nano-ω precipitates; the β+ω microstructure exhibited the highest cell adhesion as well. Moreover, the β+ω microstructure demonstrated an extraordinary corrosion resistance compared to the other microstructures (e.g., β+α'' and β+α). Scandium was recently added to the Ti-24Nb-38Zr-2Mo alloy to improve the mechanical properties, corrosion resistance, and wear performance (Tong et al. 2021). Their result exhibited non-cytotoxicity towards MG-63 cells and the Ti-24Nb-38Zr-2Mo alloy showed a higher cytocompatibility than that of the alloy without scandium.

From the biological point of view, Ti alloys surfaces are typically inert. The biological inertness results in the β alloy being safe but not bioactive. Thus, although the β alloys are free of toxic elements, surface treatment should be applied to improve osseointegration (Takematsu et al. 2016; Dikici et al. 2018).

The advantages of β Ti alloy involve their excellent biocompatibility, high strength, good corrosion resistance, and the better manufacturability compared the other high-performance alloys (Kolli and Devaraj 2018). In some β-Ti alloys superelasticity is an important property for some biomedical applications i.e., the stent (D. C. Zhang et al. 2013). The advantages and disadvantages of β-Ti alloys are listed in Table 1-3

Table 1-3. Advantages and disadvantages of β Ti alloy (Peters et al. 2003).

Advantages	Disadvantages
High strength-to-density ratio	High density
Low modulus (biomedical applications)	Low modulus (structural applications)
High strength/high toughness	Poor low-and high-temperature properties
High fatigue strength	Small processing window (some alloys)
Good deep hardenability	High formulation cost
Low forging temperature	Segregation problems
Strip producible-low cast thermomechanical processing (Some alloys)	High stringback
Cold formable (some alloys)	Microstructural instabilities
Excellent corrosion resistance (some alloys)	Poor corrosion resistance (some alloys)
Easy to heat treat	Interstitial elements pick up
Excellent combustion resistance (some alloys)	

1.8 β-Ti21S alloy

1.8.1 History

β-Ti21S alloy is a metastable β-Ti alloy showing high specific strength, and good cold formability which was particularly designed for enhanced oxidation resistance, thermal stability, elevated temperature strength, and corrosion resistance. The Ti-15V-3Cr-3Sn-3Al alloy (Ti 15-3) was earlier developed for foil products and tested for temperature beyond 815 ºC, but it was found that it is susceptible to oxidation at high temperature. In 1989 the β-Ti21S alloy was developed by Timet (commercially name Timetal 21S) to improve oxidation resistance of metal-matrix composites (MMC_s) used by McDonnell Douglas on the national aerospace plane (NASP).

1.8.2 Chemistry and metallurgy

The chemical composition of β-Ti21S alloy was tailored to attain economical forming. The non-labor intensive and inherently a high processability were the keys to making the process inexpensive. In particular, the metastable β alloy was developed to produce foil product by extended cold rolling (Bania 1994). The Ti-V system (e.g., Ti15V-3Cr-3Sn-3Al and Ti-3Al-8V-6Cr-4Zr-4Mo) was already well-established and widely used for metastable β alloys. As already written previously, Vanadium is characterized by a poor oxidation resistance. Therefore, the initial approach was to focus on V-free systems, namely Ti-Mo and Ti-Cr ones. Various types of alloying were added to the Ti-Mo system for improving the oxidation resistance and it was found that aluminum, iron, silicon, niobium, tantalum, palladium, and hafnium had a positive impact while tin, zirconium, cobalt, yttrium were not beneficial. It could be assessed that a %Mo higher than 15% did not provide any

advantage. The corrosion resistance of Ti-Cr system was not improved by alloying.

In view of the considerations above, the β-Ti21S alloy with the composition listed in the Table 1-4 was designed. Different versions of this alloy were also obtained with palladium additions for extremely high-stress corrosion resistance, and without aluminum, for orthopedic devices (Eylon et al. 1993).

Table 1-4. The chemical composition of β-Ti21S (wt.%).

	Composition, wt.%									
	Mo	**Nb**	**Al**	**Si**	**Fe**	**C**	**O_2**	**N_2**	**H_2**	**Ti**
Minimum	14.0	2.4	2.5	0.15	0.2	…	0.11	…	…	…
Maximum	16.0	3.0	3.5	0.25	0.4	0.05	0.15	0.05	0.015	…
Aim	15.0	2.8	3.0	0.20	0.3	…	0.13	…	…	bal

The percentage of β-stabilizing elements in β-Ti21S involves a Mo content around 12.8 %, which classifies the alloy as metastable β-Ti alloy. Mo and Nb are the major β-stabilizing elements. Al which is usually added for α-stabilizing, has a considerable percentage amount. The Al provides solid solution strengthening while reducing the ductility of the alloy. The major reason of adding Al to this system is accelerating the precipitation kinetics of α-phase during the aging treatment. On the other hand, it suppresses the formation of detrimental isothermal ω-phase (J. C. Williams, Hickman, and Marcus 1971). Al also contributes in reducing the M_s (martensite transformation starting point) temperature. Silicon (Si) is added to improve corrosion and creep resistance, but an excessive amount reduces the ductility. Si dissolves in Ti alloys up to 0.10 wt.% and then partially precipitates on the grain boundary in the form of silicide. This phase constrains the grain boundary movements and improves the α/β bonding at high temperatures. The silicide phase is very fine, and its solubility in Ti increase with temperature: at 1025°C it is completely redissolved. Silicides also act as the nucleation sites for the grain boundary precipitation of α-phase during heat treatment. Iron (Fe), belonging to β-eutectoid stabilizing elements, can be considered as an impurity. This element is cost-effective, but it has substantial drawbacks by widening the solidification temperature range. This might cause stronger microsegregation, hard to dissolve even with homogenization heat treatment. The diffusion coefficient of Fe is also high that has detrimental effect on the creep resistance.

Light elements e.g., carbon, oxygen, and nitrogen mainly provide solution hardening of the α-phase; however, they should be kept below a certain limit. Oxygen concentration limit is about 0.25 wt.%, higher values have negative effects on the strength-to-ductility ratio both on the annealed and aged states. In the annealed state,

oxygen reduces the work-hardening capability while increasing the tendency to localized necking. In the aged state, oxygen makes the alloy brittle by contributing toward the formation of the α-phase along the grain boundary. The α-grain boundary phase causes intergranular failure. For these reasons, the oxygen content is limited to 0.17 wt.%. Therefore, processing and heat treatment of the β-Ti21S alloy free of unfavorable phases (results from impurities) are costly (Sansoz, Almesallmy, and Ghonem 2004).

The β-transus temperature of β-Ti21S is in the range of 795-810°C (T. Xu et al. 2019; J. C. Williams, Hickman, and Marcus 1971; T. W. Xu et al. 2016). The M_s temperature is below room temperature, so that brittle martensite formation can be suppressed during manufacturing as well as during heat treatment. The alloy is known for low strain hardening behavior which provides an extreme percentage of reduction, up to 80%, during the cold reduction process. In the solution-treated state this alloy might not be easily work-hardened, and the stress should be uniformly distributed to prevent localized thinning.

Wrought β-Ti21S is produced by triple VAR to promote the dissolution of the refractory metals i.e., Mo and Nb. To fabricate coils and strips, the β-Ti21S forged slabs are rolled to the approximately 4 mm thickness hot band; further reductions may be performed by cold rolling, up to 75%, without annealing. This alloy usually is provided in the solution heat-treated condition. In this state, the alloy consists of a single β phase structure, which can be readily cold formed. The alloy is aged after cold forming to the desired strength level. The typical solution annealing temperature is comprised between 816 and 899 °C for 3 to 30 min. Longer super-transus exposure may cause β grain growth. For service temperatures < 427°C which demand higher strength, the alloy is normally aged at 593°C for 8 h. For higher service temperature applications, a duplex aging at 690°C for 8 h plus 649°C for 8 h is performed, allowing improved thermal stability. Exposure of the sample at high temperature to the air can result in particularly fine α-phase precipitation, demonstrating high strength and low ductility. Surface contamination arising from interstitial oxygen is supposed to occur for thin products, less than 1mm, during prolonged exposure above 900°C. Stress-relieving process is of importance for the complex parts made of β-Ti21S alloy. Any unrelieved thermal stress can cause cracking or warping during the fabrication or during service. The thermal stress is governed by the thermal properties of the alloy i.e., thermal expansion (α), as follows (Zhá\vnal et al. 2018):

$$\Delta L = \alpha . \Delta T + \Delta_{\rho h} \quad (3)$$

Where the ΔL is the strain, ΔT is the temperature change, and Δ_{ph} is the strain component associated to any phase transformation. The stress-relieving temperature should be high enough to release the internal stresses but should be low enough to prevent any unfavorable phase transformation. Generally, for Ti alloys the

temperature is below the β- transus and the cooling phase of treatment has to be carried out at slow cooling rate. In the case of β-Ti21S alloy the stress releaving is combined with the isothermal aging treatment. The reason is that by heating up the β-Ti21S alloy, the ω phase forms below the β-transus and they can be the nucleation site for the α precipitation.

The microstructure of β-Ti21S alloy depends on the possibility to obtain a primary recrystallized β grains before air cooling from the β phase field, and the following α precipitation. Ductility and formability are influenced directly by the β grain size; the attainment of a refined grain size during annealing is thus very important (Ivasishin et al. 2000). The α precipitates size and morphology depend on the cooling rate during solution heat treatment, on the heating rate to the aging temperature, and to the aging temperature. The α phase can precipitate during aging in different sites, primarily at grain boundary and with different morphologies. A sufficiently high cooling rate during solution annealing may prevent α grain boundary nucleation. For instance, the precipitation of this phase at grain boundary cannot be completely avoided during air cooling. A slower cooling rate can contribute toward passing the material through the (β+ω) and (β+α+ω) fields (Lütjering and Williams 2007), as shown in Figure 1-12. This provides a more homogenous distribution of nucleation sites for α during aging treatment. The duplex ageing treatment for elevated temperature applications, is comprised between the β and the α+β curves in Figure 1-12. The first step precipitates 20-30 vol.% of coarse α, and hence the β phase enriches with its major stabilizers e.g., Mo and N (Chaudhuri and Perepezko 1994).

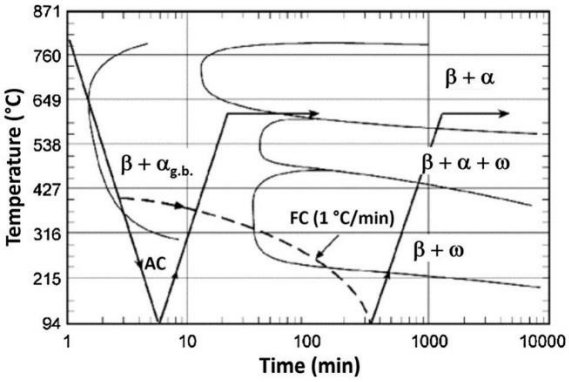

Figure 1-12 : TTT diagram for air-quenched β-Ti21S alloy (Cotton et al. 2015)**.**

1.9 Additive manufacturing of bulk metallic biomaterial

1.9.1 Background and current main technologies

The mechanical properties of metallic biomaterials are crucial since they have to fulfill particular requirements, particularly in the human body environment. For instance, the mechanical properties investigated in the human body environment may be much lower than those measured under the standard laboratory conditions. Most properties are governed by the fabrication methods, i.e., by the microstructure obtained after a specific manufacturing route. Conventional fabrication processes like casting and machining demonstrated some restrictions dealing with the properties required for biomedical devices. Processing of Ti and Ti alloys has been a tremendous challenge rooting in high reactivity at high temperatures of this metal. For the production of these alloys in suitable quality, vacuum casting is needed. The machining of these alloys is also a problematic issue due to their poor thermal conductivity, imposing the use of extreme-speed machining with a proper coolant to avoid galling, an adhesive form of wear occurring between sliding surfaces. On the other hand, Ti and its alloys are highly strain-rate sensitive which makes their plastic deformation (forging, rolling) a challenging task. Compared to the early forging technology for widely use of Ti and its alloys, dated to 1950s, some limitations related to the conventional methods overwhelmed, especially in terms of properties achievable. Not heat treatable alloys are cold forged to improve the strength. An allotropic transformation in the Ti and its alloy is also challenging in fabrication process because they demonstrate the polymorphism and the allotropic transformation temperature (β-transus) varies with the type of alloying elements. While the β-phase can be readily rolled to about 90% reduction in thickness, α and near α alloys exhibit only limited formability at low temperature. On the other hand, α+β alloys have good formability. Therefore, the microstructure plays a significant influence on the deformation behavior and work hardening rate of Ti and its alloys. The most widely used α+β alloy, namely Ti-6A-4V, has very high flow stress at room temperature leading to poor formability. On the other hand, cold processing prevents any contamination caused by high-temperature exposure. Increasing the temperature causes the oxygen and hydrogen pick-up, that may cause embrittlement. Thereby, forging should be performed at a temperature close to the β-transus (980 ºC), to induce higher formability in view of the large number of slip planes in β phase. The forging near to this temperature requires to be carried out in a controlled environment to minimize the contamination, especially oxidation, since the Ti oxide film is broken above 600 ºC causing oxidation, low mechanical properties, and poor surface finishing. This finally means a cost-demanding forming process. The improved microstructure of wrought alloys leads to better mechanical properties than cast ones . Forging of Ti and its alloy followed by machining is not effortless and cost-effective.

Additive Manufacturing (AM) represents a recently developed process to fabricate improved, tailor-made, and intricate biomedical devices. Combined with digital technologies, like medical imaging, it contributes in providing the tailor-made model for individual problems, leading to customized patient implants. Nevertheless, this method is far more expensive than conventional ones. The higher costs can be justified by the tailor-made design and customization, the facilitated surgery, the faster healing process, and the lower strain on the patient and the healthcare system. Moreover, the elastic modulus can be reduced to that of bone by porous design, and, hence, the weight can be scaled down significantly.

AM includes a class of technologies that allows the fabrication of three-dimensional (3D) components by sequentially adding material, usually layer by layer, as opposed to formative manufacturing approaches (casting and work hardening). The ISO/ASTM 52900:2015 standard classifies the AM methods into seven subclasses (Figure 1-13). Powder bed fusion is by far the main widely used process for the biomedical industry. The powder bed fusion is the AM process in which thermal energy selectively melts a powder bed. The thermal energy can be obtained from laser or electron sources that subdivide this category into laser-based powder bed fusion (L-PBF) and electron beam powder bed fusion (E-PBF) processes, respectively. The L-PBF process is conducted by moving the laser beam over the metal powder bed under a protective atmosphere, whereas during the E-PBF an electron beam scans the powder bed in a vacuum after a preheating step (above 600-700 ºC in the case of Ti-based alloys). The different cooling rates of these two PBF methods (lower rate in E-PBF because of preheating) result in different solidification conditions, hence in different microstructure and attendant properties. Most work have been dedicated to AM of Ti-6Al-4V alloy, while a limited research works was published on AM processing of biocompatible β-Ti alloys.

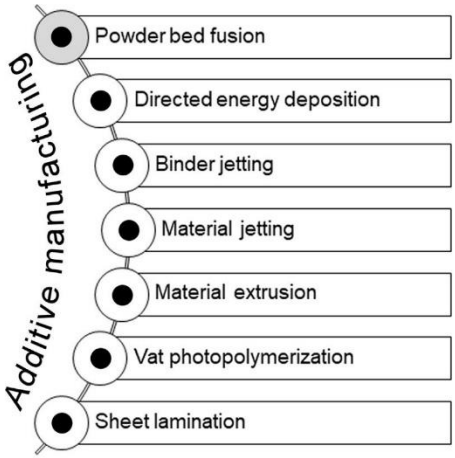

Figure 1-13 : Additive manufacturing process categories according to ISO/ASTM 52900:2015.

1.9.2 Basic of L-PBF

The L-PBF is a process for a 3D printing of the powders. The powdered material is spread across the bed, then selectively melted using a laser beam. The high degree of freedom provided by L-PBF process enables the creation of complex geometries to meet some strategic industry needs:

- light-weighting through topological optimization
- multicomponent systems (e.g., composite)
- tailored gradient structures

These benefits promote the strong growth in this technology these days.

The major variables in the L-PBF processes are: Laser power; layer thickness; scan speed; and hatch spacing (Vandenbroucke and Kruth 2007). The thermal energy delivered to each unit volume of material is influenced by these parameters, which is termed the energy density (ED) defined as:

$$E_{density} = \frac{P_{beam}}{\vartheta_{scan} \cdot S_{hatching} \cdot t_{layer}} \quad (4)$$

$E_{density}$ = energy density

P_{laser} = beam power

V_{scan} = scan speed

$S_{hatching}$ = hatch spacing

t_{layer} = layer thickness.

The function of E determines the solidification behavior and, hence, the quality of L-PBF componentsAdding material layer by layer according to the 3D design is the simple concept of L-PBF. This fabrication technique consists of many various fields of science: physics, material science, mechanic, electrical engineering, programming, design, industrial engineering, etc. The L-PBF can be inferred because of and interaction of numerous subprocesses, including the absorption and reflection of laser radiation, heat and mass transfer, phase transformations, gas and fluid dynamics, chemical reactions, solidification, shrinkage, deformation, etc. (Yadroitsev 2009; Moges, Ameta, and Witherell 2019; Rubenchik, King, and Wu 2018). Figure 1-14 demonstrates the workflow of part fabrication, the schematic of L-PBF machine, and process of laser-material interaction in L-PBF. More than 130 input parameters might influence the process (Rehme, Emmelmann, and Beyer 2005). Parameters can be categorized as predefined and variable. The predefined parameters are the properties of the material used (density, melting point, thermal conductivity, particle size distribution, etc.), build environment (shield gas properties), and laser beam properties (mode, wavelength). Some of the most important process variables are laser power, focal spot diameter, scanning speed, powder layer thickness, hatch distance, the oxygen level in the chamber, rate of flow gas, etc. (O'Regan et al. 2016). Of these parameters, four large groups of parameters have the main impact on the L-PBF quality i.e., Machine-based, Material-based, and Post treatment parameters. Their interaction is nonlinear and understanding the effect of altering some parameters on the final product quality is not yet well available (Moges, Ameta, and Witherell 2019; Vock et al. 2019; Schmidt et al. 2017).

The LPBF process initiates with designing the 3D models and follows by slicing the model in the form of solid or surface. Defining the manufacturing parameters (e.g., scanning strategy, build rate, layer thickness, and build angles, etc.) then applies. During the process, the part is created from single tracks, layer by layer. Interaction of the laser beam with a pre-deposited powder layer on the base plate, causes localized melting, and the solidification leads to the formation of a single track. This track is the base structural unit of an L-PBF part: the single layer of the object is formed by lasering multiple tracks, one after each other, providing a certain superimposition, to warranty uniform layer thickness and proper surface finishing. The 3rd object dimension is formed by the deposition of multiple layers. The scan strategy i.e., scanning path, scanning direction, scanning sequence, etc. is a critical factor that affects the quality of the fabricated part. The L-PBF component must be fixed to the base place directly and/or by support structures. Supports not only provide the fixation of the part to the base plate also allow to rotate the part in the desired position to

reduce the deformation through controlling the heat dissipation, to reduce thermal stresses. Nevertheless, the L-PBF quality is influenced by its orientation respect to the base plate, the type and position of supports, the scan strategy, etc. The process parameters have to be optimized to ensure high density, good surface quality, and good geometric accuracy of parts. Overall, four different types of defects are introduced in L-PBF process, namely: lack-of-fusion porosity, keyhole porosity, balling, and gas porosity (Gordon et al. 2020).

The components fabricated using L-PBF process may not meet all requirements directly in the as-built state; thus, post processing is frequently needed. The final product quality is defined by key characteristics: microstructure, porosity, residual stresses, surface roughness, and dimensional accuracy. To improve the surface quality of the L-PBF parts, the main drawback of this technology, mechanical post-processing is applied. On the other hand, the proper heat treatment is often required to obtain the appropriate mechanical properties, relieve the residual stress, and reduce the porosity of as-built part. Usually, the post-process may involve the following actions: first heat treatment of attached part to the base plate to relieve the residual stresses; base plate removal; support removal; cleaning the part (e.g., ultrasonic cleaning); second heat treatment to improve the mechanical properties (e.g., annealing, aging, hot isostatic pressing); final machining and polishing.

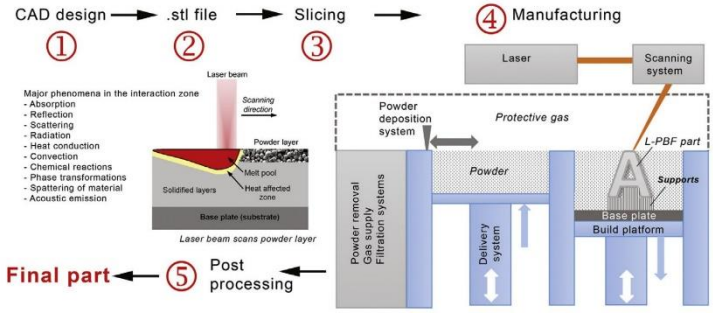

Figure 1-14 : A workflow of part creation from CAD design, schematic of L-PBF machine and process of laser-material interaction in L-PBF (Yadroitsev, Yadroitsava, and du Plessis 2021)**.**

1.9.3 LPBF of bulk β-Ti alloy for biomedical application

Titanium and its alloys are broadly used as a biomaterial because they provide an exceptional combination of mechanical properties with appropriate biocompability. They can be manufactured well with the L-PBF because of their good inherent weldability properties. The wide range of titanium alloys i.e., α and β can be manufactured by the L-PBF process. Moreover, modification in chemical composition

through alloying additions, heat treatment enables to tune the properties of fabricated component with respect to the needed applications. Most L-PBF works in the biomedical filed of Ti alloys has focused on processing α/β alloys, mostly Ti-6Al-4V alloy. In contrast to the limited studies on L-PBF processing of biocompatible β-Titanium alloys.

The recent paradigm of AM components for the biomedical application has led to the use of β-Ti alloys to reduce elastic modulus. The non-toxic β-stabilizer elements should be also used as an alloying element. Commonly used elements are group IVb, Vb, and VIb refractory/transition metals: Hf, Ta, Nb, Mo, Zr, or a combination thereof. Hf, Ta, and Nb are rare and expensive elements. On the other hand, the prealloying and powder manufacturing of them is not unexpensive. Some researchers have tried to stabilize the β-phase through in-situ alloying in L-PBF from the mixture of powder (Kong et al. 2021; Vrancken et al. 2014; Kang et al. 2019). Although the final component could be potentially used in some cases, the samples fabricated by this method usually demonstrate segregation, separation of impurities and alloying elements in different regions of solidified alloy, which in turn cannot be used for the biomedical implant due to safety reasons. Segregation may pose some problems both in physical and mechanical properties. An overview of the mechanical properties of some L-PBF β-Ti alloys is given in Table 1-5. Lower elastic modulus and higher fracture elongation are reported for the L-PBF processed β-Ti alloys compared to the reference alloy (Ti-6Al-4V). This is accompanied by 15%-50% lower values for yield stress and ultimate tensile strength.

Table 1-5. Mechanical properties of L-PBF processed β-Ti alloys.

Alloy	σy0.2 (Mpa)	UTS (Mpa)	E (Gpa)	El (%)	Reference
Ti-24Zr-4Nb-8Sn	563 ± 38	665 ± 18	53 ± 1	13.8 ± 4.1	(L. C. Zhang et al. 2011)
Ti-15Ta-1.5Zr	890 ± 51	869 ± 19	92 ± 9	16.1 ± 1.2	(L. Yan et al. 2016a)
Ti-15Ta-5.5Zr	960 ± 32	925 ± 35	72 ± 4	18.9 ± 2.0	(L. Yan et al. 2016a)
Ti-15Ta-10.5Zr	805 ± 19	769 ± 16	43 ± 3	15.1 ± 0.9	(L. Yan et al. 2016a)
Ti-50Ta	/	925 ± 9	76 ± 4	12	(Sing, Yeong, and Wiria 2016)
Ti-6Al-4V-10Mo	858 ± 16	919 ± 10	73 ± 1	20.1 ± 2.0	(Vrancken et al. 2014)
Ti-6Al-4V (ref)	990 ± 5	1095 ± 10	110 ± 5	8.1 ± 0.3	(Facchini et al. 2010)

$\sigma_{y0.2}$: 0.2% yield stress; UTS : ultimate tensile strength; E : elastic modulus; El : fracture elongation. The tensile test samples were tested parallel to the building direction for both alloys.

Microstructural characteristics impact the mechanical properties of L-PBF processed β-Ti alloys.Ishimoto et al (Ishimoto et al. (2017) applied two scan strategies to fabricate Ti-15Mo-5Zr-3Al β-alloy. Since the elastic modulus is highly dependent on the crystallographic orientation, varying the scan strategy led to different textures, hence different elastic moduli. They pointed out that the elastic modulus could be

obtained either as isotropic (75 ± 3 GPa) or anisotropic (69 ± 1 GPa and 100 ± 5 GPa), shown in Figure 1-15. They explained that bidirectional scanning with or without a rotation of 90º between the layers resulted in textures with the preferential <001> and <011> crystallographic orientation along the building direction, respectively. This is because the various scan strategies alter the path of the maximum thermal gradient, and hence, the texture.

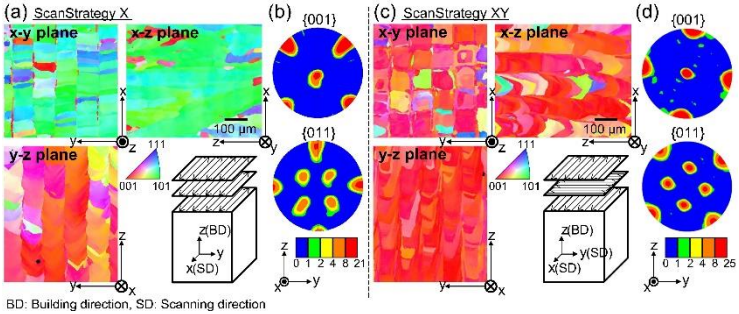

Figure 1-15 : Texture of L-PBF Ti-15Mo-5Zr-3Al β-alloy (a,c) Inverse pole figure (IPF) images from the three orthogonal planes. (b,d) (001), and (011) pole figures measured in the y–z plane. BD is the building direction and SD is the scanning direction (Ishimoto et al. 2017).

The corrosion behavior and the biocompatibility of Ti biomaterials produced by L-PBF is important. L-PBF Ti-6Al-4V alloy showed vulnerability to pitting corrosion in the 3.5wt.% NaCl solution compared with its counterpart fabricated by casting (Dai et al. 2016).. The corrosion results evidenced that the phase constitution leading to different corrosion resistance: the AM-produced alloy containing α' martensite and less β phase showed worse corrosion resistance when compared with the casting alloy. The corrosion behavior of the L-PBF β-Ti alloys was also investigated. Qin et al (Qin et al. (2019)) compared the corrosion behavior of Ti-24Nb-4Zr-8Sn manufactured by casting and L-PBF. A single β-phase microstructure was stabilized in both cases. The potentiodynamic polarization curves of both alloys were very similar (Figure 1-16), suggesting a very similar corrosion behavior. From the result of this study, it can be inferred that the corrosion behavior of this Ti alloy is mainly governed by their phase constituents, but not the fabrication method.

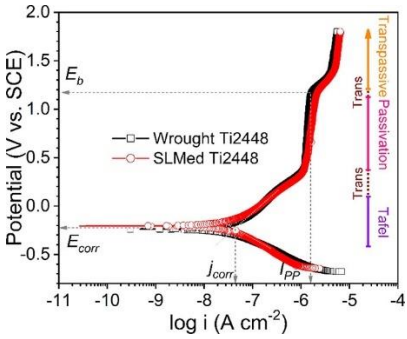

Figure 1-16 : Electrochemical measurements of L-PBF and wrought Ti–24Nb–4Zr–8Sn (Qin et al. 2019).

A few works investigated the biocompatibility of β-Ti alloy fabricated by L-PBF. L. Yan et al (L. Yan et al. (2016b) inserted the Ti-15Ta-10.5Zr alloy mini-plate osteosynthesis in rat tibia. After five weeks, the histological analysis suggested multiple positive correlations between genes denoting inflammation and bone remodeling around the implant, proving that no periosteum necrosis or osteoporosis of the bone was caused. Therefore, the authors concluded that this alloy fabricated by L-PBF is suitable for bone implants. The cell culture measurement of printed Ti-30Nb-5Ta-3Zr showed good spreading behavior and cell adhesion with no cell cytotoxicity according to the RGR value (Luo et al. 2019). The Zr addition improved the biocompatibility of the Ti-Nb-Ta based β alloy processed by L-PBF (Kong et al. 2021). The ion releasing and cell culture assess tests confirmed that the corrosion product film on the alloys was stable after 30 days immersion. It showed the good biocompatibility regarding cytotoxicity during culture with corrosion ions obtained in that alloys. Although all these three studies were performed on the L-PBF β alloy, the tested components were polished and the effect of the as-built surface finishing on the biocompatibility has not been investigated.

1.10 Additive manufacturing of cellular lattice metallic biomaterial

Many materials have a cellular structure, i.e., an assembly of prismatic or polyhedral cells with solid edges and faces packed together to fill space (Figure 1-17). Cork, wood, sponge, and bone are all examples of cellular solids in nature. Engineered honeycombs and foams have been made from polymers, metals, ceramics, and glasses, and their structure provides a unique property that can be exploited in a variety of applications. The structure of cellular materials has been researched since the 1660s, when Robert Hooke examined a section of cork in his microscope and first used the term “cell” to describe its structure (Lorna J. Gibson and Ashby 1997). The cellular structure can be divided into the foam-like porous

structure and architected cellular materials in terms of repeatability and filling the space. The foams have a random, stochastic, structure (Figure 1-17 A and B) generally acquired by a manufacturing process that offers only partial control on the cell size and cell-wall thickness, while architected cellular materials (Figure 1-17C) have a well-controlled periodic geometry which can be completely determined by a small number of design parameters.

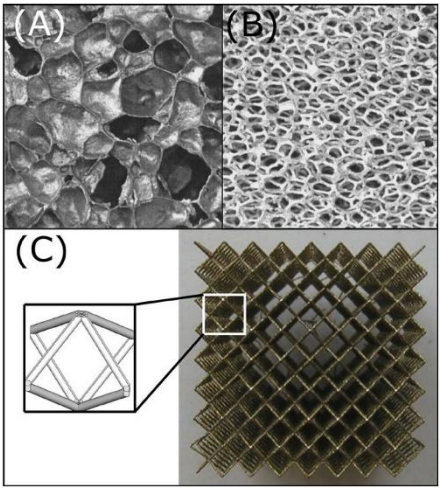

Figure 1-17 : Examples of cellular materials: (A) closed cell foam (L J Gibson 2000)**. (B) open cell foam** (L J Gibson 2000)**. (C) regular cellular material (body cubic centered BCC unit cell)** (Smith, Guan, and Cantwell 2013).

Cellular materials have been usually used in the past for load-bearing applications. These materials have been manufactured using conventional methods of fabrication that involve liquid- and solid-state processes (e.g., direct forming and powder metallurgy) and electro- or vapor-deposition. The lack of form-freedom is the main inherent limitation for traditional fabrication techniques. In particular, these show limited capability in controlling the sizes and shape of cells. The AM techniques provide the freedom to accurately manage the size and architecture of cells at the microscale (L J Gibson 2000). Powder bed fusion techniques are the most widely used AM processes for manufacturing cellular material. L-PBF is more diffused than E-PBF, and its reliability is generally more consolidated. The cellular materials manufactured by L-PBF, therefore, have attracted a greater deal of attention these decades. The method allows the fabrication of cellular structures with intricate microarchitectures and the high resolution, required for the biomedical applications (Frazier 2014; Chen et al. 2021). There are, however, some manufacturing restraints

for this method for fabrication of cellular material that deviates the final properties from the as-designed one, e.g., the orientation of the lattice for the build direction, minimum feature size (wall thickness, edges, and corners), the sizes of over hangs, and the constraints concerning the design of support structures and their removal (X. Wang et al. 2016).

1.10.1 Architecture

The structure of cellular materials varies from the near-perfect order of honeycomb to the disordered, three-dimensional networks of sponges and foams. According to (Lorna J. Gibson and Ashby 1997), unit cells that stack to fill a plane in two dimensions are depicted in Figure 1-18. The shapes demonstrate both isotropic and anisotropic cells. The cells can be spatially arranged in more than one direction to create structures with varying edge connectivity, hence giving different properties. The man-made cellular designs use the regular shapes in principle while the natural two-dimensional cellular material is less regular: a soap froth between glass slides. But even the most random designs in the nature and human body obey certain topological laws, which implies that precise statements can be made about them.

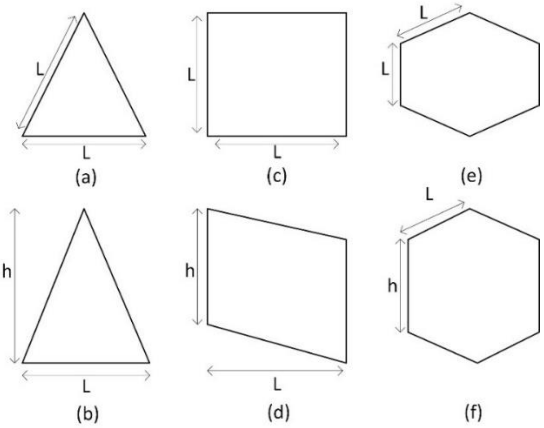

Figure 1-18 : Polygons found in two-dimensional cellular materials: (a) equilateral triangle, (b) isosceles triangle, (c) square, (d) parallelogram, (e) regular hexagon, (f) irregular hexagon. Note that any triangle, quadrilateral, or hexagon with a center of symmetry will fill the plane, adapted from (Lorna J. Gibson and Ashby 1997).

In three dimensions a greater diversity of cell shapes is possible (Figure 1-19). Like the two-dimensional cells, they must pack to fill the space. Only a few unit cells can be spatially stacked in undistorted periodic patterns: the triangular, rhombic, and hexagonal prisms, the rhombic dodecahedron, and tetrakaidecahedron are space-

filling solids. Moreover, if distorted, the tetrahedron, the icosahedron, and the pentagonal dodecahedron can be space-filling bodies as well. Consequently, lattice cellular materials are created initiating from these fundamental unit cells. Every cellular structure is composed of vertices, joined by edges, which surround faces, which enclose cells. In two-dimensions the vertices are joined by edges that enclose faces or cells. According to the Euler's law (Euler 1746) for a large aggregate of cells, the cells parameters can be termed as follows:

$$F - E + V = 1 \quad (two\ dimensions) \tag{5}$$

$$-C + F - E + V = 1 \quad (three\ dimensions) \tag{6}$$

Where the terms define the number of faces F, of edges E, of vertices V, of cells. For example, a honeycomb with regular hexagonal cells has 1 cell, eight faces, six edges surrounding each face, and twelve vertices.

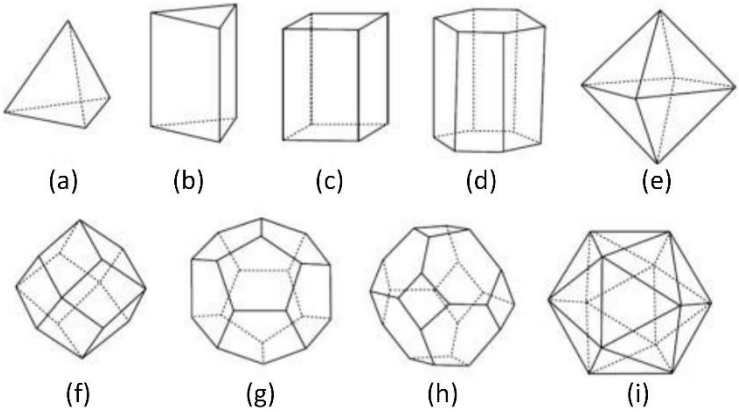

Figure 1-19 : Three-dimensional polyhedral cells: (a) tetrahedron, (b) triangular prism, (c) rectangular prism, (d) hexagonal prism, (e) octahedron, (f) rhombic dodecahedron, (g) pentagonal dodecahedron, (h) tetrakaidecahedron, (i) icosahedron (Heo, Ju, and Kim 2013).

The most widely used lattice materials are those based on strut-based lattices. They are developed starting from the fundamental unit cells. In strut-based lattices, nodes placed at the vertices or edges of unit cells are connected by the struts (or beams). Benedetti et al (Benedetti et al. 2021) classified twenty strut-based lattices architectures, shown in Figure 1-20 (A). They are mostly based on the cubic cell in which the cells are designed somehow to achieve the desired density and mechanical properties. The strut-based lattices can be also classified according to the deformation behavior based on their struts' connectivity (Deshpande, Ashby, and Fleck 2001). According to the stability criteria of Maxwell (*M*) (Clerk Maxwell 1864),

the requirements for a pin-jointed frame made up of *b* struts and *j* joints to be both statically and kinematically determinate in 2D and 3D are

$$M = b - 2j + 3 = 0 \quad (2D) \tag{7}$$

$$M = b - 3j + 6 = 0 \quad (3D) \tag{8}$$

Under compression, the frame can collapse because of the rotation of the struts about the joints (i.e., it becomes a mechanism), shown in Figure 1-21 (a) in which the b = 4, j = 4, and M = -1 (i.e., it becomes a structure), shown in Figure 1-21(b) in which the b = 5, j = 4, and M = 0. The first frame is defined as "*bending-dominated"* because the struts with connected joints bend when loaded (the node resists rotation), while the latter frame as *"stretching-dominated"* because the struts are loaded principally axially even with connected nodes, with some struts experiencing tensile forces. Two examples of 3D unit cells are illustrated in Figure 1-21 (c) and (d).

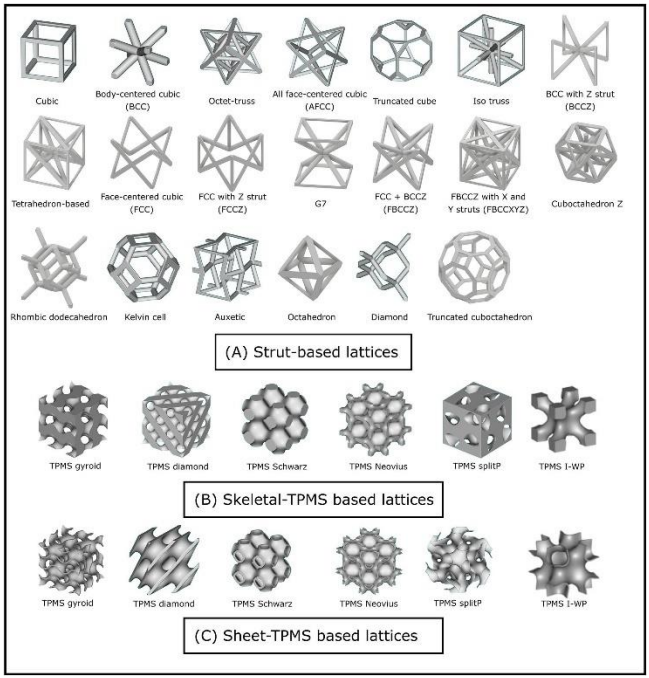

Figure 1-20 : Various architectures of lattice structures (A) Strut-based lattice cells, (B) Skeletal- and (C) Sheet-triply periodic minimal surfaces (TPMS) (Benedetti et al. 2021)**.**

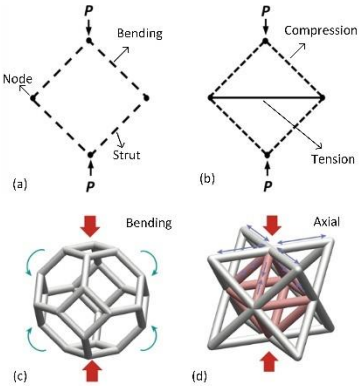

Figure 1-21 : Two examples of pin-jointed frames: (a) bending dominated, and (b) stretching-dominated. (c) bending dominated and (d) stretching dominated unit cells.

The *triply periodic minimal surfaces* (TPMS) class of cellular materials is of interest these decades due to its applications, some of them are shown in the last two rows of Figure 1-20. They have been proved to be very suitable for their additive manufacturability due to their curved surface geometries (Maconachie et al. 2019; Bobbert et al. 2017). Schwarz firstly proposed the Primitive and Diamond TPMS in the 19th Century (Schwarz 1890). TPMS are mathematically created surfaces with no self-intersecting or enfolded surfaces. They are packed together in a periodic 3D pattern and the surface area for a given boundary is locally minimized such that the mean curvature at each point is zero. Therefore, they are known as triply periodic minimal surfaces structures. TPMS can be expressed mathematically using the level-set approximation method based on harmonic functions of the spatial cartesian coordinates and the desired level of density (Michielsen and Kole 2003). To sketch TPMS structure from the mathematical formulation, two different tactics are usually implemented (Al-Ketan, Al-Rub, and Rowshan 2017). In the first one, the TPMS is thickened to create a solid lattice known as “sheet TPMS”; while in the second, the volume disconnected by the TPMS is filled to produce a solid lattice known as the “skeletal" or "cellular" TPMS.

Two main lattice parameters of cellular materials, that any property can be related to, are the relative density $\bar{\rho}$ and porosity P expressed as follows (Lorna J. Gibson and Ashby 1997):

$$\bar{\rho} = \frac{\rho}{\rho_0} \quad \textbf{(9)}$$

$$P = 1 - \bar{\rho} \quad \textbf{(10)}$$

Where ρ_0 is the density of the base (solid) material. The relative density can be calculated as the ratio between volume occupied by the cellular material and the total cell volume (i.e., including porosity). Some models were proposed in (Lorna J. Gibson and Ashby 1997) to calculate the relative density of a few different types of cellular materials as a function of the strut length and diameter, according to geometrical considerations. The porosity and elastic modulus of the lattice material implant has linear correlation (Scott J Hollister 2005). This ratio is obtained by Ashby-Gibson models for the foams (M. Ashby et al. 2000) and these relations hold well for lattices – the elastic modulus can be theoretically predicted from the porosity level. Although these parameters are very useful to categorize the lattice materials, they are not sufficient to distinguish the morphology of cellular materials. As an example, bending- and stretching-dominated lattices may show different mechanical properties and failure mechanisms even with the same relative density.

From the biomedical point of view, the lattice structure morphology is of critical importance. Certain requirements of lattices to be used in biomedical implants, especially those dealing with bone replacement, have been reported in several reviews (L E Murr 2017; X.-Y. Zhang, Fang, and Zhou 2017; X. Wang et al. 2016; Dong, Tang, and Zhao 2017). The leading consideration for bone replacement is matching the elastic modulus of the implant to the bone, to minimize the stress shielding, as shown in the Figure 1-22 the mismatch between the elastic modulus of the bone and implant causes the stress shielding and hence bone resorption.

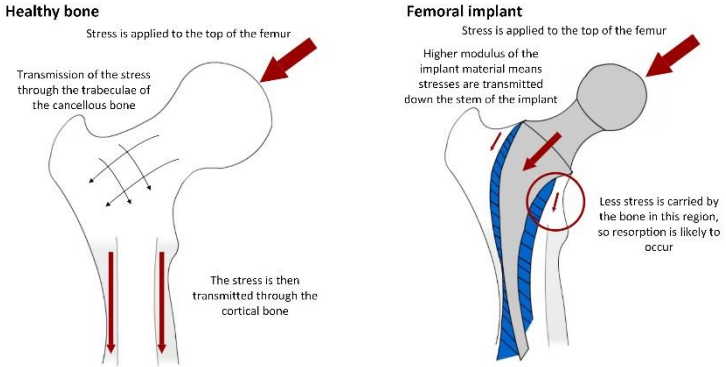

Figure 1-22 : Stress shielding mechanism (Arifin et al. 2014).

The implant should also allow in-growth of new bone. This osseointegration arises from a combination of physiological processes: initial cell seeding, followed by vascularization and bone growth. The first step is closely influenced by the surface availability for cell attachment in which the low permeability provokes the initial cell

seeding. An irregular cavity, edges, and non-spherical pore shapes can be considered as the best locations for cell seeding in the lattice materials. For subsequent vascularization and bone growth, good permeability is needed to enable nutrients to flow through the structure. Therefore, even if a large surface would be desired to reduce the elastic modulus; there is still a big debate about the ideal porosity percentage, pore size, and shape leading to the best osseointegration. For instance, very broad pores size ranges, namely 50-1200 μm, were suggested for new bone growth and high fixation in orthopedic or dental applications (Lopez-Heredia et al. 2008; Taniguchi et al. 2016a; BOBYN et al. 1980).

1.10.2 Structural integrity Ⅰ：static mechanical properties

Cellular materials can be classified according to their behavior under external loads. The mechanical behavior of strut-based cellular material, with the same relative density is depicted in Figure 1-23. In the specific case, the cellular material is Inconel 625, a Ni-superalloy additively manufactured by L-PBF. This material is not suitable for biomedical implant, but it is ductile enough to allow showing the effects of the lattice morphology on the mechanical behavior. The applied compression leads to either stretch- or bending-dominated behavior. The stress-strain curves highlight three different parts:

(1) a first linear elastic regime until the yielding of struts by bending or stretching;
(2) a plateau regime inside which the cells begin to collapse due to buckling, brittle crushing or yielding dependent on the properties of the base material and the cell morphology;
(3) a densification part in which the cells collapse so that the struts reach contact against the other.

The stretch-dominated lattices usually show higher initial stiffness and yield strength than bending-dominated lattices. The post-yielding softening is detected in the stretch-dominated lattices because of sudden failure, followed by plateau consisting of stress peaks which is the indication for the progressive failure of the layers. The stretch-dominated lattices are most structurally efficient but are more prone to sudden failure and are less effective in dissipating deformation energy. Bending-dominated lattices are more rigid, show a more progressive transition to the stress plateau regime, which appears more flat (L J Gibson, Ashby, and Harley 2010; M. F. Ashby 2006). Under tensile stresses the stress-strain curves would be very similar in the elastic range, but after yielding the struts will tend to gradually align along the loading direction, without any buckling, until failure (Raghavendra et al. 2020). In tensile testing of cellular material, failure can be either ductile or brittle, depending on the plastic resources of the solid material (M. Ashby et al. 2000).

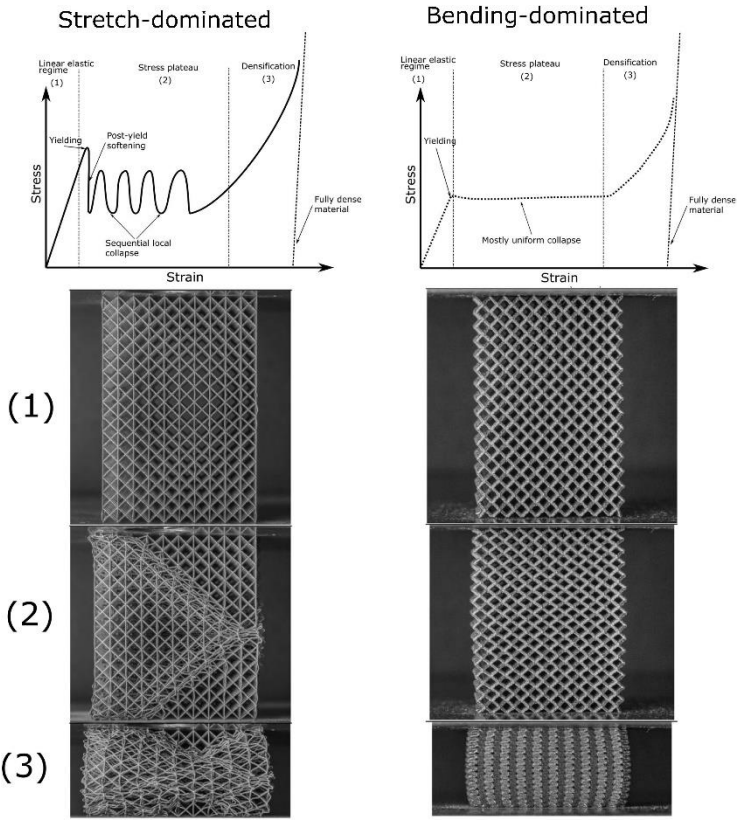

Figure 1-23 : Typical compressive strain-stress curves for stretching- and bending-dominated cellular materials with same relative density (curves adapted from (M. F. Ashby 2006)**). (1) Linear-elastic regime. (2) Post-yield stress plateau. (3) Densification. Photographs were taken in** (Leary 2018) **at the corresponding deformation regime on bending- (left) and stretching- (right) dominated lattice structures. The base material is Inconel 625.**

Various numerical and theoretical models have been proposed over the past decade to predict the behavior of the cellular materials (Smith, Guan, and Cantwell 2013; Ahmadi et al. 2014; González and Nuño 2016; Alaña et al. 2019; Ruiz de Galarreta, Jeffers, and Ghouse 2020). The high number of cells in a lattice structure usually makes it difficult to model the entire cellular geometry in full detail, even by utilizing advanced finite element software with powerful processing hardware. Therefore, the main goal of those methods is the investigation of the effective

properties of the cellular structure based on the material properties and morphology of the cells. The basic concept for mechanical modeling of cellular material is the Representative Volume Element (RVE), that is the fracture of volume of lattice. The RVE represents the properties of the entire system. This element should be small enough to decrease the complication of the problem, on the one hand, and big enough to estimate the exact behavior of entire cellular structure with good accuracy, on the other hand. The unit cell can be considered as RVE in case of regular periodic structures but identifying the size of RVE in case of non-regular periodic lattice structures is not readily available, for instance, fully random foams. In this case, the size of RVE gradually increase until a convergence is observed in the properties, even in this case the computational limitation must be deemed (Shahzamanian et al. 2013; S J Hollister and Kikuchi 1992; Hashin 1983).

The effective elastic constant and the yield strength of 2D and 3D regular lattices can be expressed by the closed-form model (L J Gibson et al. 1982; Lorna J. Gibson and Ashby 1997). The model assumes that the cell struts or walls behaves like Euler – Bernoulli beams. The model calculates the elastic constant from the stress strain delivered by applying uniform loads to the unit cell. The model proposes two equations correlating elastic modulus and strength to the relative density of the cellular material using a power law:

$$\frac{E}{E_0} = C_1\left(\frac{\rho}{\rho_0}\right)^n = C_1\bar{\rho}^{\,n} \quad \textbf{(11)}$$

$$\frac{\sigma_y}{\sigma_{y0}} = C_2\left(\frac{\rho}{\rho_0}\right)^m = C_2\bar{\rho}^{\,m} \quad \textbf{(12)}$$

Where E_0 and σ_y are elastic modulus and yield strength of the base material and C_i $(i=1,2)$, m, and n are constants that depend on the form of unit cell and can be defined theoretically (closed from solution) or fitted experimental data (Ghouse et al. 2018; 2017; C. Yan et al. 2014). n is equal to 1 in an ideal stretching- and 1.5-2 in an ideal bending- dominated structure, as shown for example in Figure 1-24, where the experimental values are compared to the ideal ones (Tan et al. 2017). These types of plots are useful to compare the properties of different cellular materials in a broad porosity size range.

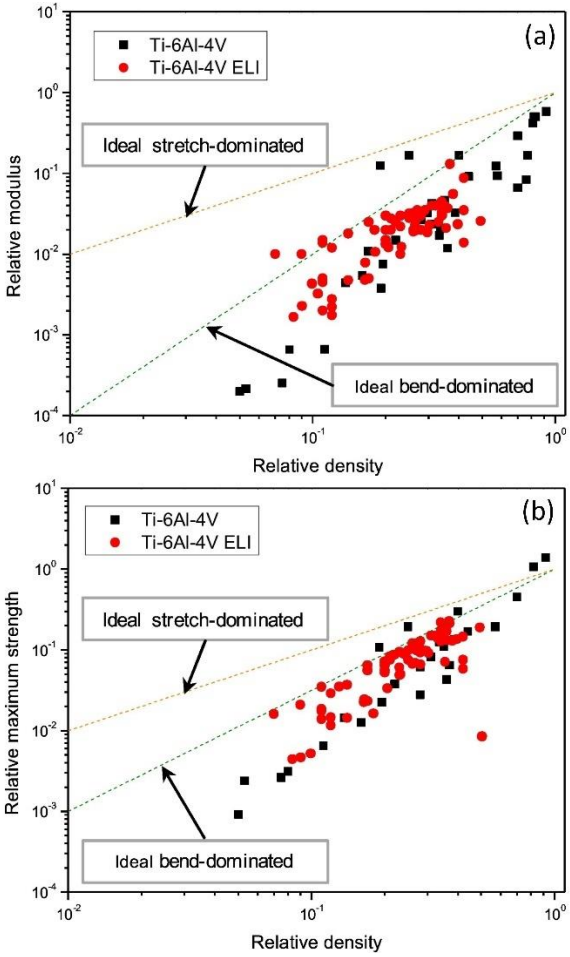

Figure 1-24 : Relative elastic modulus vs relative density (a) and relative strength vs relative density plots for various cellular materials (Tan et al. 2017)**.**

It can be inferred that decreasing the relative density leads to decreasing the elastic modulus and strength both theoretically and experimentally. It is pertinent to mention that experimental data shows large scattering and that most of them are in better agreement with Gibson-Ashby models for bending-dominated behavior, even though some of the topological unit cell are nominally classified as stretch-dominated (e.g., FCCZ or octet). The most important bending effects resulted from the geometric

inaccuracies, affecting the manufactures cellular material, is believed to be the reason to follow the bending-dominated mechanism for the experimental data. The main geometrical inaccuracies are the misalignment of the strut axis according to the loading direction. This study reveals the importance of investigation of the cellular material manufacturing related issues. Comparing the Ashby-Gibson model with the experimental data, there are also some limitations for this model. The model loses its accuracy by increasing the density (usually it should be less than 0.3 (Arabnejad and Pasini 2013)); the model is impractical for very complex lattices; classical beam theory cannot accurately consider the stress-strain state at stress concentrators (such as at cell nodes). Although the homogenization method, the most advanced numerical technique, proposed to be replaced with traditional methods, this one also has some limitations related to the assumptions that is based on.

The finite element (FE) method on the other hand provides valid results without hypothetically limitations. Theoretically, no limitations can be considered for the even complex lattices model including finest details. Indeed, the FE allows to study the local stress concentrator locations. The only limitation is associated to the heavy computational power required by this method, especially for the complex lattice architectures. The FE models can be divided into two groups based on the beam elements and continuum elements (Dong, Tang, and Zhao 2017). The beam elements are computationally fast, versatile, and useful to capture failure mechanisms (Luxner, Stampfl, and Pettermann 2005; Smith, Guan, and Cantwell 2013). Some studies used the beam element model for mechanical behavior investigations of cellular materials. For example, (Alkhader and Vural 2008) used the beam model to show the loss of periodicity in the structure of a stretching-dominated cell leads into a shift towards a bending-dominated mechanical behavior, and hence a reduction in stiffness. Besides the advantages of the beam models, these are valid only for the slender cell walls and they are believed to be practically impossible to apply for high relative densities – they do not provide the local stress-strain states as well. The continuum models on the other hand allows to predict the mechanical behavior with higher accuracy at the expense of long computation times (Dong, Tang, and Zhao 2017). The failure mechanisms of stretching- and bending-dominated lattices were modeled employing 3D continuum and successfully validated by experimental data in (Kadkhodapour et al. 2015). The FE continuum model also used to investigate the effect of tissue ingrowth in L-PBF Ti-6A-l4V biomedical scaffolds considering the multi material analyses (Hedayati et al. 2017). Recently, the X-ray Computed Tomography (CT) was used as the input model instead of ideal CAD to simulate the mechanical behavior of as-fabricated lattices (Dallago, Winiarski, et al. 2019; Raghavendra et al. 2021a; Veyhl et al. 2011; Xiao et al. 2017). Two major problems were observed in these studies. First, they simplified the problem by using the periodic boundary conditions in some cases in which causes some deviation in the mechanical behavior of the

experimental tests. Second, the mesh generation quality is not that good to capture the fine local stress concentrator, if even so, the computational power of the computer is still a big issue.

1.10.3 Structural integrity Ⅱ: Fatigue behavior

Fatigue is a process of progressive localized permanent structural change arising in a material subjected to conditions that create fluctuating stresses and strains that culminate in cracks formation or failure after subjecting to an adequate number of cycles (Stephens et al. 2000). The exposed materials to the time-varying loads are prone to failure at stress levels well below a given ultimate strength of the material. The crack initiation process occurs at stress amplitudes below the yield limit of the material. According to the material properties and stress concentrator location, the loading level can be changed. If the loads are above a certain threshold, the microscopic damages in the material occur, leading to the nucleation and propagation of cracks and ultimately fatigue failure. The main peculiar crack initiation mechanism in a ductile material is the localized dislocation slip along preferential crystallographic planes, leading to the formation of slip bands under cyclic loading (Figure 1-25). The microscopic damage occurs mainly on the surface since here the material is less constrained. The slip bands tend to form in the plane of maximum shear stress (45º) in ductile materials. The exposed fresh slip plane surface is covered by the oxide layer and usually followed by strain hardening. Therefore, this process is irreversible. Accumulation of the slip deformation leads to the formation of the microcracks under further cycling loading. The engineering material containing microstructural flaws like micro segregation, voids, inclusions, etc., which cause localized stress concentration under cyclic loading, may reduce the threshold stress needed slip bands formation. The total fatigue life, described by the number of cycles to failure N_f, consists of two different contributions, that for crack initiation, N_i, and that for crack propagation, N_p.

$$N_f = N_i + N_p \tag{13}$$

It is worth mentioning that the crack initiation phase period is strongly affected by surface finishing, a very critical issue for as-fabricated AM component; by the material strength; and by the microstructure. In the crack propagation phase, the rate is not that much related to strength as it is on the elastic modulus. It is reasonable to assume that due to the rough surface of the as-fabricated AM part, the total fatigue life is driven by the first phase. From the economical point of view, the AM process is still considered the expensive process and any post treatment for reducing the surface roughness will add the additional cost into the final product, especially for the lattice material with complex structures. For machined specimens, the N_i covers most of the life, while for the welded structures small process-induced cracks present before loading, and hence the N_f is mainly determined by the propagation phase.

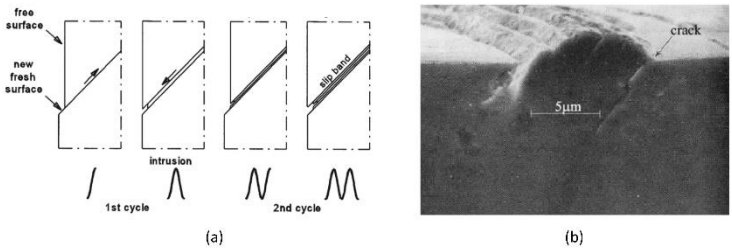

Figure 1-25 : Crack initiation by formation of slip bands in ductile materials, schematic in (a) and Macrographic in (b). (Jaap Schijve 2009; Suresh 1998).

The engineering materials with limited ductility (e.g., high-strength metals) show more localized form of damage near to the defects within the material (François, Pineau, and Zaoui 2013). In such conditions, the crack can initiate from the defects and propagate through the section of the specimen on a plane perpendicular to the loading direction. Thus, the fatigue life can be effectively enhanced by controlling the defects i.e., porosity, lack of fusion, inclusions, slip bands, weak grain boundaries, and surface imperfections in AM components. The fatigue behavior can be divided into low-cycle fatigue (LCF) and high-cycle fatigue (HCF) depending on the occurrence of plastic deformation, or not, respectively. A widely used fatigue model describing the LCF is the Coffin-Manson equation (Coffin 1972):

$$\frac{\Delta\varepsilon_p}{2} = \varepsilon'_f(2N)^c \quad \textbf{(14)}$$

Where $\Delta\varepsilon_p$ is the plastic strain amplitude, ε' is the fatigue ductility coefficient, $2N$ is the number of reversals to failure, and c is the fatigue ductility exponent (≈-0.5). Both fatigue constants are empirically available in the literature review.

On the contrary, the HCF is modeled commonly using stress-based expressions. Basquin's proposed the model representing the relation between the applied cyclic stress and the fatigue life. Commonly, for this model several samples are tested under fatigue loading with different stress levels and Basquin's equation will represent linear regression of fatigue life data in a log-log plot of stress life, known as S-N curve (J. Schijve 2003).

$$\sigma_a = A(2N)^B \quad \textbf{(15)}$$

Where σ_a is the applied stress amplitude, $2N$ is the number of reversals to failure, A is the fatigue strength coefficient, and B is the fatigue strength exponent. The fatigue data can be collected under a fully reversed stress cycling in an ideal condition, in this case, the $\sigma_{max} = \sigma_{min}$ and $\sigma_m=(\sigma_{max}+\sigma_{min})/2 = 0$. It could be seen in real-life applications such as biomedical hip implants; however, the actual loading includes superimposed

oscillatory stress. From this perspective, the Haigh diagram is offered to demonstrate the non-zero mean stress effect on fatigue behavior in which the oscillatory stress amplitude, σ_a plots versus the mean stress, σ_m using constant lifelines. In this way, the plots can be divided into infinite and finite lifetime regions.

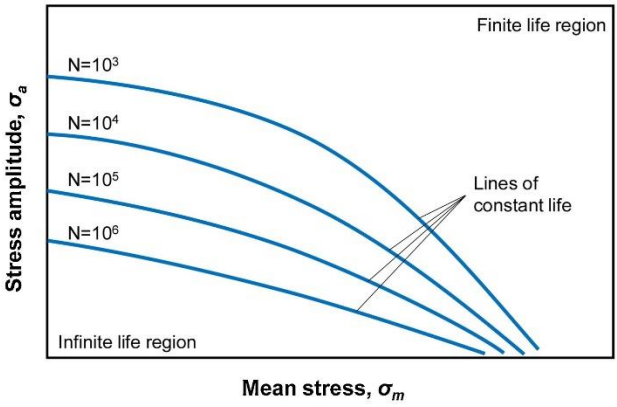

Figure 1-26 : A Haigh diagram showing the mean stress effect on fatigue properties (Benedetti et al. 2021).

Regarding the fatigue properties of the cellular material, some more aspects should be added to the fundamental approaches of fatigue investigation i.e., porosity and relative density related factors. The majority of fatigue experiments of cellular materials have been conducted under uniaxial compression-compression in which the applied cyclic load is always in the negative regime (Kelly et al. 2019; M. W. Wu et al. 2020; Y. J. Liu et al. 2020; van Hooreweder et al. 2017a; Yánez et al. 2020; Amin Yavari et al. 2015a; Ahmadi et al. 2018). The quasi-static characterization was commonly preceded in that works to estimate the yield and plateau stress and the fatigue lives ranging from a few thousand to 1-2 million cycles explored between 10 and 80 % of yield stress. The fatigue damage mechanism of cellular material can be divided into three regions based on the global strain evolution (see Figure 1-27): the plastic strain is accumulated in the first stage in which culminates in the crack initiation. The crack propagates through the material characterized by a smoother slope of the total strain in stage Ⅱ and followed by crack coalescence typified with abrupt increment in the slope of total strain at stage Ⅲ. During the very early cycles of stage Ⅰ, the plastic redistribution of peak stresses is believed to be found at the high stress concentrator locations of lattices which are followed by elastic-shakedown. The progressive accumulation of inelastic strain, known as ratcheting, is dominated

the largest part of the first stage. The intensity of ratcheting arising in the first stage is known as ratcheting rate, i.e., the rate of accumulation of inelastic strain in the direction of the applied load. Boniotti et al (Boniotti et al. (2019) attested that the ratcheting rate is relatively independent from the cell architecture. Contrariwise, the effect of the porosity and cell architecture was pronounced by plotting the ratcheting rate versus applied stress amplitude in (S. Zhao et al. 2018), highlighting that the fatigue strength is strongly influenced by the cell morphology of lattices.

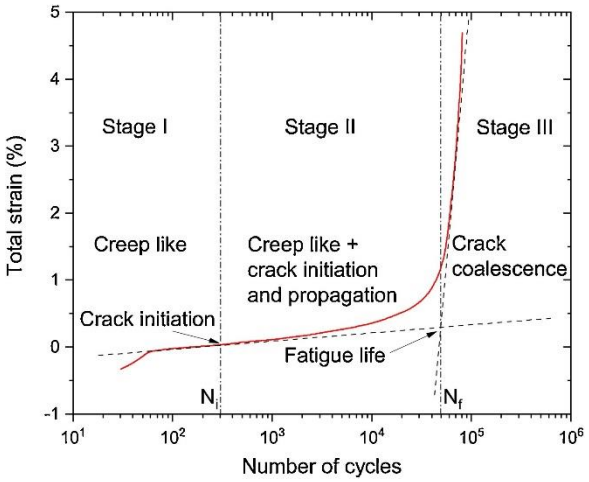

Figure 1-27 : Typical three stages evolution of fatigue damage of cellular material (Özbilen et al. 2016; Lefebvre, Baril, and Bureau 2009).

Presented in this regard also for the first time by Zadpoor and collaborators (Amin Yavari et al. 2015b) that compression-compression fatigue strength of lattice materials is mainly affected by cell type and porosity. In this way, they normalized the fatigue strength according to the yield strength allowing to exclude the contribution of porosity. Benedetti et al (Benedetti et al. 2021) also plotted the normalized fatigue strength of various cellular materials as a function of relative density as shown in Figure 1-28. The overall result of this plot illustrates that the normalized fatigue strength shows a decreasing trend with increasing porosity. This survey shows that for the Ti-6Al-4V alloy, apart from the cubic cell, strut-based cellular design lies on the lower band of the plot, supporting the suitability of the material for the fabrication of cellular structures. Moreover, by comparing different materials with the same cell design it can be deduced that ductile materials demonstrate higher normalized fatigue strength. High ductility is expected to accommodate stress peaks in the vicinity of stress concentrators, i.e., nodes and geometric imperfections. The truncated

cuboctahedron (M. W. Wu et al. 2020; Amin Yavari et al. 2015b) and topology optimized truss (Y. J. Liu et al. 2020) cells are among the strut-based lattice materials showing the highest normalized fatigue strength. The cubic cell design printed orthogonally with respect to the building platform and loaded parallel to the struts demonstrates a high fatigue strength (Amin Yavari et al. 2015b). This result is an exception and there has been reported that no fatigue damage was observed for the simple cubic design which can be associated with the loading configuration and strut directions where the struts only undergo compressive local stresses. On the contrary, the other cell architectures subject to the local bending stresses are less fatigue resistant. Despite the fact that the cubic cell design is not of interest in practical applications, due to the high anisotropy, the cubic design is interesting for fundamental investigation of the fatigue properties under reduced effect of the bending dominated local stresses (Dallago et al. 2021). The TPMS cellular structure shows better fatigue performance compared to the strut-based lattices, clearly demonstrating that zero curvatures surfaces play a positive influence upon reducing the effect of detrimental local stress raiser points.

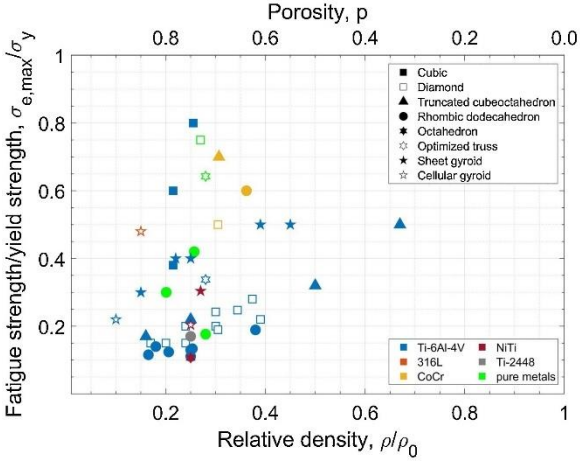

Figure 1-28 : Compression-compression fatigue strength normalized with respect to the yield strength as a function of the open porosity, $\sigma_{e,max}$ is the fatigue strength at 10^6 cycles to failure (Benedetti et al. 2021).

1.10.4 Review of manufacturing-related issue

Although the L-PBF technique offers form-freedom design, there are still some design constraints that need to be considered. Several guidelines (Kranz et al., 2015) have been proposed in the past to deal with the limitations of the L-PBF process and to define the processibility windows. The relevant topics in this regard include the

minimum feature size (e.g., wall thickness, edges, and corners), the orientation of the lattice with respect to the build direction, the sizes of the overhangs, and the requirements regarding the design of support structures and their removal (Wang et al., 2016). Overhangs are one of the most important aspects that need to be carefully considered, as they can create undesired defects (Su et al., 2012; Calignano, 2014). Overhangs are the parts of structure that are not self-supporting. An example is reported in Figure 1-29. As the manufacturing process progresses, there are no solidified sections from the previous layers that support overhangs, making them susceptible to collapse and defect formation. Successful fabrication of overhangs is, therefore, often dependent on the proper choice of the fabrication angle (Su et al., 2012). For overhangs exceeding a specific size and forming small angles with the powder bed, support structures need to be used. These will have to be removed during post-processing, which can damage AM parts.

In fact, and indeed, the same manufacturing consideration as above are required for the cellular structures and even the impact of the same manufacturing imperfections may have more detrimental contributions on their mechanical properties. For instance, the surface irregularities i.e., micro-notch and porosities are more critical due to the effective size compared to the strut diameter or sheet thickness of lattice structures. In this section, the manufacturing related-issues of the lattice material will be reviewed and the design and technological measures to improve the quality of lattices will be further discussed.

1.10.4.1 Surface morphology

High roughness is a very typical feature of AM components. Changing the process parameters and orientation of the part, with respect to the build platform, can lead to different surface roughness (Strano et al. 2013). Not optimized process parameters may create irregular tracks and an imperfect melting pool which enhances a surface roughness. Such defects are common where low laser power or high scan speed are used. Despite the fact that slower scan speed or higher laser power may result in better surface quality, out of optimum-range values will lead to excessive temperature rise and melt pool size. A larger melt pool brings to larger tracks, coarser surface defects, and more particles attached to the surface. This is of great importance for cellular structures, in view of the high surface area and the many different surface orientations.

The surfaces quality in as-built AM components can be classified according to their orientations. Upward-facing (upskin) surfaces are smoother compared to the other surfaces, however, the laser tracks are visible. Side surfaces are typically less smooth, while downward (downskin) surfaces are very rough even with excess melted material (dross formation). Stair-step effects, layer on top of each other make the steps, can be found in both upskin and downskin surfaces where the surface-oriented

at an angle (Strano et al. 2013). This stair-stepping is closely related to the layer height setting that has an adverse effect on the surface quality when sets in a greater height because they do not follow the as-designed geometry, especially at angular orientation (Figure 1-29).

The attached powder and stair-step effect are influenced directly by the melt pool. The local heat transfer is determined by the size of melt pool. During layer manufacturing, the energy transfer from the laser beam is strongly affected by the complex interaction with the solid/powder system. The powder typically is less conductive than the solidified metal from which the heat applied by the laser beam will be carried away. The local heat may affect the powder bed by attaching the powder to the surface of the solidified body. These powders are typically partially melted, due to the local heating leading to rough surfaces. Their amount typically varies on differently oriented struts, being lower on vertical struts and considerably high on struts forming low angles with the powder bed. (Pyka et al. 2013).

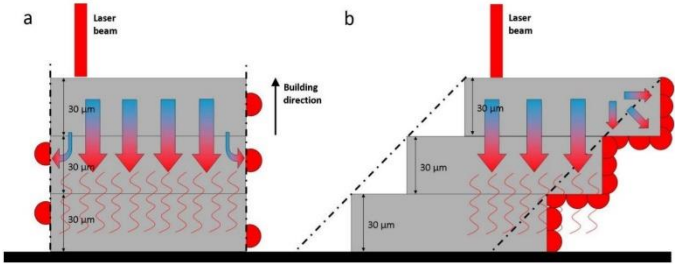

Figure 1-29 : Schematic illustration of heat flow and stair-step effect for vertical (a) and angular (b) struts relative to the build platform (Pyka et al. 2013)**.**

The focused laser spot size in the L-PBF system is usually 50-100 µm and single-track widths is typically 100-200 µm. These process parameters create the fundamental minimum size limitation in the fabrication of the strut or sheet. An individual melted layer in the lattice structure may need only one or a few tracks adjacent to one another. Building a layer which cannot cover the entire width of the single-track (either from the design or at the angular locations) may cause either thinner or thicker features. On the other hand, the layer is included of the overlapped single tracks to fabricate the full dense structures. This can be called the resolution or the minimum feature size of the system that can be built of the exact dimension, which is typically 0.1-02 mm. Another related issue that can impact the surface quality is the start-stop cycling of the system for each scan track. Typically, the lattice features involve short scanning tracks, which may impact on the regularity of scanning, negatively affecting the surface quality. Murchio et al (Murchio et al. 2021) studied the effect of the building orientation on the surface quality for the micro struts with a

diameter of 0.6 mm (Figure 1-30). They reported that the building angle less than 45º caused a very rough surface on the downskin while the upskin showed a smoother surface. The individual single track is well visible for the strut fabricated at 0º relative to the build platform.

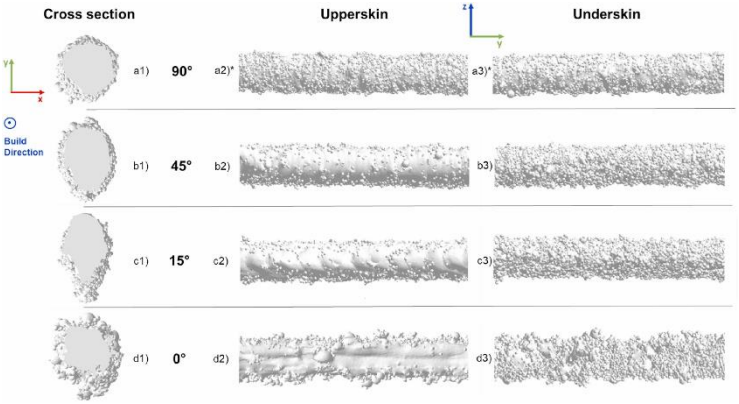

Figure 1-30 : Surface quality of 3D CT scan of four different lattice struts with respect to the build orientation and up and down skin surfaces. a1) to d1) shows the xy cross sections while a2) to d2) the upskin on the yz plane and a3) to d3) the downskin yz profile (Murchio et al. 2021)**.**

Residual stress and warping or cracking caused by the local high temperature of a laser beam also may have a considerable impact upon the surface quality. Unsupported horizontal or diagonal struts leading to build up the residual stress are prone to the warp upwards and cause failure. In addition, unsupported horizontal and diagonal struts are typically fabricated thicker than vertical struts, because of the dross formation on the downskin surfaces and melt pool penetration into the underlying layers (D. Wang et al. 2013; Murchio et al. 2021), as shown in the Figure 1-30 C and d. Accordingly, vertical struts showed better mechanical properties than horizontal and diagonal ones, due to the lower surface imperfections which create lower geometrical imperfections and stress riser location, detrimental both for quasi static and time-varying loadings, respectively (Murchio et al. 2021).

1.10.4.2 Geometrical deviation and CT scan

In addition to the surface roughness, the geometrical inaccuracies have a direct impact on the mechanical properties. Typically, poorly optimized process parameters directly affect the surface roughness, and in worst cases, it causes geometrical inaccuracies, due to the fact that the accumulated imperfection over the surfaces results in deviation of the as-built geometry from the as-designed CAD. This can be realized observing the Figure 1-29b where the stair-step effect and attached powder

culminated in the deviation of the oriented as-built strut from the designed CAD (dashed line). It is believed that the geometrical accuracy is determined by the size of the melt pool and building orientation. The smaller melt pool size provides a higher resolution for the fabrication of the fine features. The melt pool size is also directly influenced by the process parameters, including spot laser size, laser power, scanning speed, layer thickness, and the hatch distance (Mullen et al. 2009; Sing, Wiria, and Yeong 2018; Qiu et al. 2015). As discussed earlier, due to the heating transfer, gravity, and capillary force, the CAD deviation is found to be higher for the horizontal struts, while increasing the strut angle reduces the geometric inaccuracies. Moreover, the inclined strut is highly influenced by the stair-step effect to create a not straight strut (Figure 1-31a) (Moussa et al. 2021; Bagheri et al. 2017). The mismatch accuracy is influenced by shrinkage during the solidification as well (Zhu, Anwer, and Mathieu 2017).

The geometrical mismatch can be investigated with some parameters especially introduced for the strut-based lattices (Dallago, Raghavendra, et al. 2019; van Bael et al. 2011; L. Liu et al. 2017): strut waviness, the deviation degree of offset from the centroid of the cross-sections along the length of the strut which results in wavy effect strut section irregularity, the deviation and/or inclination toward printing direction of the as-built cross-section of the strut with respect to the as-designed shape; strut thickness variation, the deviation of the average thickness of the cross-section along the length of the strut from the as-designed geometry; nodal geometry variation, the alteration of the local node geometry resulted from the excessive material added or uncompleted junction created during the fabrication process. The printing inclination typically plays the main role on the geometrical mismatch so that the material in excess tends to accumulate on the downside of the struts and junctions (relative to the build platform).

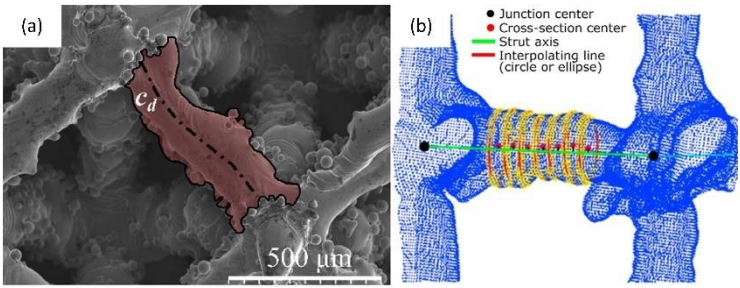

Figure 1-31 : (a) SEM micrograph of the octet truss lattice structure showing the geometrical irregularities in a diagonal strut (Moussa et al. 2021) **and (b) the ellipse fitting to the Micro-CT data for geometrical deviation investigations** (Dallago, Winiarski, et al. 2019)**.**

The geometrical deviations may have important implications on the mechanical properties. excessive material or/and attached powder may increase the elastic modulus, while the strut waviness may reduce the stiffness, in particular for the stretching-dominated lattices. The enhanced waviness factor may activate the bending moments that trigger a drop in the elastic modulus. Moreover, strut waviness reduces the strength to some extent because the structure becomes weaker to the external loads (L. Liu et al. 2017; Qiu et al. 2015).

The Micro-CT scan provides interesting possibilities to study the geometrical imperfections in a 3D view. (Dallago, Winiarski, et al. (2019) fitted the ellipse shape to the cross-section of the struts of lattice structure reconstructed by Micro-CT data to study the thickness and waviness of the strut using an in-house developed MATLAB Code. The authors reported that the horizontal struts showed higher thickness and waviness compared to the vertical ones (the building direction was reported orthogonally for the simple cubic design). They also investigated the effect of geometrical imperfection on the elastic modulus and stress concentration locations using the continuum and beam FE analyses in the elastic regime. They reported that the elastic modulus increases with the increasing thickness of the strut, in agreement with the Ashby-Gibson model. On the other hand, the bending moments introduced by the strut waviness and the junction center displacement reduced the elastic modulus of the stretching-dominated structure (simple cubic). The FE analyses of the stress states at/around the junction indicated that the as-built junction can be considered as high stress concentrator point in the lattice structures. However, they were not able to exactly identify and correlate the simulation result to the experimental one, most likely due to the complexity of the problem. (Raghavendra et al. 2021b) used the continuum FE model in both elastic and plastic regimes to investigate the simple cubic and trabecular lattice structure of reconstructed Micro-CT data. Comparing the as-design and Micro-CT model for stress-strain curve, the latter one could better represent the experimental data, although a modeling of the complete geometry might provide better results. The model could also predict roughly the exact location of the fracture in the component. The results evidenced a deviation in the prediction of the elastic modulus which can be improved by upgrading the accuracy of the FE modeling, especially during the mesh generation, to avoid the loss of data.

1.10.4.3 Microstructural aspect and internal defects

The physical and mechanical properties of the lattice materials are correlated to microstructure and internal defects. For instance, the internal porosity may reduce the density (physical properties) and mechanical strength (mechanical properties). Due to the rapid cooling rate and the re-solidification in L-PBF process, the microstructure of the as-built component typically contains elongated grains oriented along with the heating laser source (DebRoy et al. 2018). This effect is well described and

schematized in (Q. Zhang et al. 2016) where the solidification of the bulk additively manufactured Ti-6Al-2Zr-2Sn-3Mo-1.5Cr-2Nb alloy was studied. The layer by layer solidification led to a columnar structure characterized by the epitaxial growth of crystals along the building direction. The coarsening of the β grains was observed in correspondence of the first layers. Despite the fact that the prior β columnar grains are prevailing in a bulk component, the microstructure of lattice materials with smaller features (strut or sheet) may differ from the bulk samples, mainly due to the faster solidification rate caused by the high surface area. This has been studied for strut-based lattice structures with various thicknesses in (Niendorf, Brenne, and Schaper 2014). The results of this study showed that there is a critical strut thickness for epitaxial columnar growth, which was between 0.65 and 1.1 mm for the austenitic steel 316L. A similar result was reported for the AlSi12 alloy lattice material as well (Reinhart, Teufelhart, and Riss 2012). Due to the fact that mechanical properties, especially fatigue resistance, are influenced by the microstructure, grain morphology is of critical interest. Y. J. Liu et al (Y. J. Liu et al. 2017) investigated the fatigue crack growth on the Ti2448 β-Ti lattice material. As shown in Figure 1-32, the fatigue crack propagated through the equiaxed β grains, by transgranular fracture, while it deflected at a high angle boundaries of columnar grains. The grain morphology is determined by the laser scan strategy and the process parameters. For instance, the outer contour applied with the hatch strategy for the internal section may develop the fine and equiaxed grain over the surface with the columnar grain in the internal regions of as-built sample. On the other hand, it has been mentioned that long columnar grains are not favorable to mechanical properties because they do not have enough grain boundary obstacles avoiding the movement of the dislocation during the stress applying (DebRoy et al. 2018). This indicates the importance of the microstructure for the structural integrity, which has been far less studied so far.

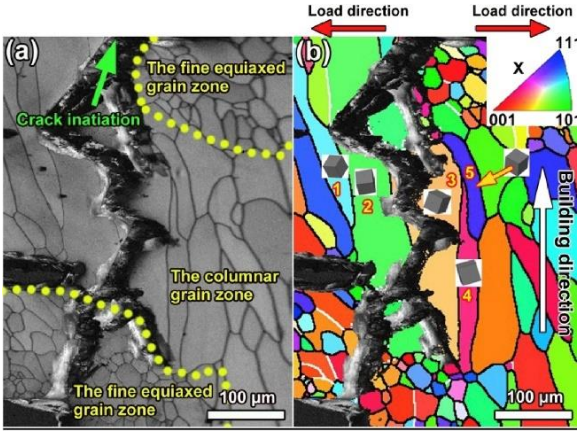

Figure 1-32 : The EBSD images of the fatigue crack propagation track for the lattice Ti2448 component. (a) the morphology of the single β grains, (b) the EBSD orientation microscopy map of the strut.

Typically, the as-built Ti-6Al-4V alloy cannot be used for biomedical applications due to the brittle martensite structure leading to low ductility and poor fatigue resistance. The heat treatment is vital for the AM component made of this alloy, whose modified microstructure provides better properties(van Hooreweder et al. 2017b). The HIP treatment was used in (M.-W. Wu et al. 2017) in an attempt to improve fatigue endurance. The microstructure transformed from brittle α'-martensite to more ductile α+β after HIP, (Figure 1-33), leading to the crack blunting under fatigue loading. A similar concept was applied to CP-Ti and Ti-6Al-4V alloy fabricated with two different cellular structures, showing that the ductility contributed to the improvement of the fatigue properties (Y. J. Liu et al. 2020).

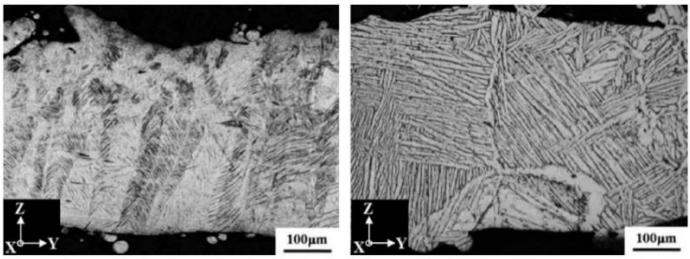

Figure 1-33 : The microstructure of strut-based lattice of Ti-6Al-4V alloy in a as-built (a) and after HIP treatment (b) showing the change in microstructural features (M.-W. Wu et al. 2017)**.**

In addition to the microstructure, the imperfect process parameters leading to the internal defects may result in reducing the mechanical properties of the lattice materials, as shown in a recent study of the auxetic meta-biomaterial (Kolken et al. 2021b) in which the improper process parameters caused significant internal porosity. The Micro-CT and SEM images revealed a large volume of interconnected pore spaces, as shown in Figure 1-34. An unstable vapor cavity caused by the high laser power with respect to the scan speed may leave the rounded pores in the solidified material, known as a keyhole. Extremely low laser power with high scan speed, too large layer thickness, and too large hatch spacing may create the lack of fusion porosity. Due to the rounded shape of keyholes, they are less detrimental to mechanical properties compared to the highly irregular shape of lack of fusions (Benedetti et al. 2021). In addition to the requirement of optimizing the process parameter to reduce the porosity, the overlapping of the contour and hatch tracks can be the source of the porosity. This is critical and observed sometimes near the edges of the parts leading to the subsurface porosity.

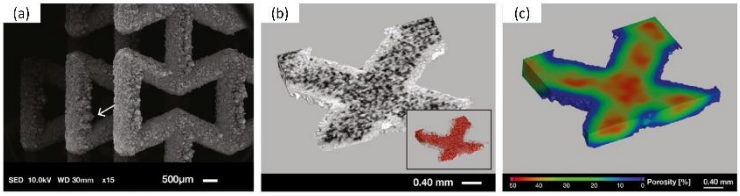

Figure 1-34 : The structure of auxetic design observed using SEM (a), the inside morphology (b) and the local average porosity imaged using micro-CT (Kolken et al. 2021b).

1.10.5 In vitro and In vivo studies of cellular Ti materials

The cell architecture and pore sizes should be tailored for better biocompatibility. The improper process parameters of AM leading to the deviation from the as-designed CAD may have a considerable impact also on the biocompatibility, for instance due to the too low pore size.

The biological studies can be divided into two categories, *in vitro* and *in vivo,* for the evaluation of cell adhesion and osseointegration, respectively. These analyses are required before designing and manufacturing the lattices implant (Khalili and Ahmad 2015). The cell adhesion is composed of three stages: cell attachment to the substrate, flattening and propagating of the actin skeleton with the development of focal adhesion among the cell and its substrate. The life expectancy of the implant and its effectiveness are governed by the affinity of the cells to an implant. The cell adhesion is not only related to the cell properties but also on implant properties like the surface topography, roughness, the wetting behavior, etc. (M. Wang et al. 2016b). Therefore, several studies have focused on the cell architecture and pore size effects

on the biological response of cell attachment.

D. Zhao et al (D. Zhao et al. 2018) investigated the cell affinity of cellular tetrahedron and octahedron of Ti fabricated by L-PBF and found that 1000 μm pore size is the most appropriate for cells to adhere, to flatten, to spread. In 500 μm pore size the cell seeding is obstructed but the fatigue endurance was higher. In a similar study, the various cell architectures of Ti-6Al-4V alloy with a designed pore size of 500 and 100 μm were tested for biological behavior with seeded human periosteum-derived cells for 14 days (van Bael et al. 2012). Smaller pore sizes and corners in lattices were more useful for cell growth at the early stage. In fact, the cell growth is controlled by a curvature-driven mechanism in this stage so that the living cells could densely distribute in the corners and the cell could bridge. The large pore sizes were detected to be more metabolic active after 2 weeks. The influence of various cellular Ti materials on human osteoblasts behavior in static and dynamic cells was investigated in (Markhoff et al. 2015). The cubic and pyramidal designs showed better collagen formation in comparison to the diagonal lattices.

The osseointegration is not only influenced by the size and shape of pores, roughness, the chemical composition of the implant. Type of loading and stresses are also of importance, as mentioned in the different studies. (Kokubo and Yamaguchi (2016) modified the surface of the implant by the bioactive material. In this work, it was mentioned that initial appetite layer formation on the surface plays an important role for further bone growth, and that layer can be considered as the indication for in vitro bone growth test success. The comprehensive osseointegration study made in ((Taniguchi et al. 2016b) on the L-PBF heat-treated Ti diamond structures with 300-900 μm pore size implanted in the rabbit's tibia. After two weeks, the lattice structures with 600 μm designed pore size demonstrated better bone implant fixation ability and mechanical properties; however, after 4-8 weeks, all forms of lattice designs showed high fixation ability. The true effect of pore size is not very distinguishable; mainly due to the irregular shape of the pores, high surface roughness, and collapsed pores which are all caused by the improper AM process parameters. The efficient vascularization could not be achieved for the as-designed 300 μm pore size because of the small size of real pores. This study also suggested the diamond structures for orthopedic load-bearing applications. H. Wang et al (H. Wang et al. (2018) found the diamond structure as a good option for bone replacement implants. After 8 weeks, diamond regular and irregular structures demonstrated better biocompatibility performance overall. The results show that at the early stage, smaller pores with high curvature were more beneficial for initial bone growth while the bigger pores had advantages at later stages of bone regeneration. Cheng et al (Cheng et al. (2017; 2014) inspired a real human femoral head reconstruction by CT scan to design and fabricate the Ti-6Al-4V implants. Their result showed the enhancement in the

osseointegration compared to the regular design, due to the combination of pore sizes and bone mimicking features. Cohen et al (Cohen et al. (2017) monitored and studied CT scan data after implantation. The histological cross-sections of the solid lattice biomimetic implants in rabbit femur after 10 weeks showed an increase in cell response and mineralization. This confirms that the trabecular bone-inspired porosity stimulates bone growth to a great extent.

1.10.6 LPBF of cellular β-Ti alloy for biomedical application

Additively manufactured lattice structures of titanium alloys, especially Ti6Al4V, are widely studied for their use in bone replacement implants. However, few studies have focused on β-Ti alloys for biomedical application.

Y. J. Lieu et al (Y. J. Liu et al. 2016) comparatively investigated the microstructure, defects, and mechanical behavior of β type Ti-24Nb-4Zr-8Sn rhombic dodecahedron lattice structure manufactured by EMB and L-PBF. The microstructural analyses showed that due to the high temperature (∼500 °C) of the powder bed in EBM, leading to the low cooling rate, the α+β microstructure was present in the as-built material. On the other hand, the high cooling rate of L-PBF process led to the formation of a very fine β dendritic structure. Therefore, the reported elastic modulus was higher in the case of EBM sample (∼1.34 ± 0.04 GPa) in comparison of the L-PBF sample (∼0.95 ± 0.05 GPa) fabricated with the same powder and geometry. The Micro-CT results and micrographs revealed that the EBM sample had lower porosities compared to the L-PBF samples, mainly due to the better process parameter optimization, this is evident looking at Figure 1-35 (a-b). Round porosity (gas trapped) and keyhole porosity were found for the EMB and LPBF processed materials, respectively. They reported that the porosities were mainly due to the vaporization of tin during the melting process, a phenomenon limits the manufacturability of this alloy in essence. The study shows that internal defects had a minor impact on the compressive properties so that the L-PBF sample with finer microstructure showed higher yielding strength. The annealing not only caused the grain coarsening, but also the α phase dissolution, leading to a reduction of the yielding strength, as shown in Figure 1-35 (c). The graph shows that the mechanical behavior of all tested samples is bending-dominated. However, the as-built EBM sample evidenced a worse surface geometrical inaccuracy.

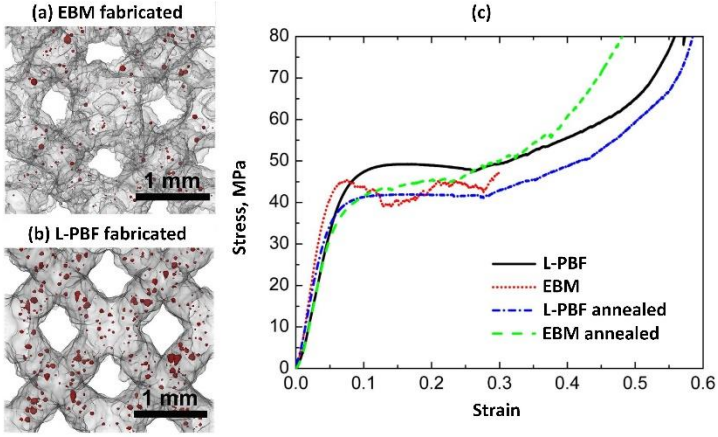

Figure 1-35 : The micro-CT results imaged of EBM (a) and L-PBF (b) cellular materials; the typical compressive stress–strain curves for samples of Ti-24Nb-4Zr-8Sn alloy in as-built and annealed conditions (c) (Y. J. Liu et al. 2016).

The fatigue samples of this work were heat treated to achieve a single-β structure for all of them. The fatigue failure of cellular material could be related to the surface defects at low stress levels, and to internal porosities at high stress levels, respectively. The fatigue behavior was believed to be ruled by the cyclic ratcheting and surface properties, resulting in similar properties for the materials produced with both manufacturing processes. However, the higher data scattering at high stress levels for L-PBF samples, is likely due to the higher number of internal defects.

Luo et al (Luo et al. 2020) fabricated the β type Ti-30Nb-5Ta-8Zr alloy by L-PBF. They optimized the process parameters to obtain a defect free bulk sample. Rhombic dodecahedron and body centered cellular architectures with 20 and 30 % relative density were further printed to investigate both, mechanical and biological properties. The mechanical properties data was found comparable with that of cancellous bone (Sevilla et al. 2007), as shown in Table 1-6. After 72h of cell culturing, all the as-built lattices showed homogeneous cell distribution and the absence of cell cytotoxicity based on the fluorescence images analyses and cell relative growth rate (RGR) evaluation, respectively. Moreover, the proteomic study revealed the high biocompatibility of this alloy so that the surface proteomic signature of the printed TNTZ alloy can activate some crucial protein pathways and increase cell mobility, protein binding, and cell proliferation.

Table 1-6. Comparison of the mechanical properties of cancellous bone and L-PBF processed Ti-30Nb-5Ta-8Zr alloy (Luo et al. 2020; Sevilla et al. 2007)**.**

Alloy	$\sigma_{y0.2}$ (Mpa)	El (%)	E (Gpa)	σ_{emax} (Mpa)
Cancellous bone	15.2 ± 8	7.1 ± 3	1.08 ± 0.86	25 ± 8.1
Ti-30Nb-5Ta-8Zr	12.5-67	5.7	0.7-4.4	22

$\sigma_{y0.2}$: 0.2% yield compression stress; El : fracture elongation; E : elastic modulus; σ_{emax}: fatigue strength limit.

1.10.7 Aim of this study

The main aim of this Thesis work is to investigate the behavior of a beta-Ti-alloy for the biomedical application, to address some of the limitations of the alloys currently used in the AM field:

- the presence of toxic elements in the biomedical Ti- alloys;
- the formation of a hard and brittle martensitic microstructure during L-PBF;
- the need of heat treatment to modify the microstructure and to recover the limited ductility of the martensitic structure;
- The elastic modulus of the benchmark alloy (Ti6Al4V) is still high with respect to that of bones – stabilizing the β phase not only contributes toward reducing the elastic modulus, also provides better biocompatibility compared with a mixture of α + β phases.

Based on the above limitations and literature review, the Ti-21S alloy is used for this study because of its potential to provide less toxic alloying elements i.e., vanadium, and its potential to stabilize the β phase during L-PBF. To the authors best knowledge, there were not works published related to the fabrication of Ti-21S alloy with AM process at the starting point of this work. Therefore, firstly physical, mechanical, and biological properties of the additively manufactured bulk material are investigated. In the second phase of the work, the manufacturability of simple cubic lattice coupons is studied. The lattice manufacturability will be studied referring to geometrical accuracy, morphology, internal and surface defectiveness, and microstructure. Micro-CT based simulation was used to determine the minimum manufacturable cell size of Ti-21 lattice structure. The selected cell structure was mechanically tested to validate the manufacturability trend. After finding the minimum cell size, the more complex octet structure was fabricated, and its mechanical properties are investigated.

1.11 Reference

Affatato, Saverio. 2014. “Contemporary Designs in Total Hip Arthroplasty (THA).” *Perspectives in Total Hip Arthroplasty*, January, 46–64. https://doi.org/10.1533/9781782420392.1.46.

Ahmadi, S. M., G. Campoli, S. Amin Yavari, B. Sajadi, R. Wauthle, J. Schrooten, H. Weinans, and A. A. Zadpoor. 2014. “Mechanical Behavior of Regular Open-Cell Porous Biomaterials Made of Diamond Lattice Unit Cells.” *Journal of the Mechanical Behavior of Biomedical Materials* 34 (June): 106–15. https://doi.org/10.1016/J.JMBBM.2014.02.003.

Ahmadi, S. M., R. Hedayati, Y. Li, K. Lietaert, N. Tümer, A. Fatemi, C. D. Rans, B. Pouran, H. Weinans, and A. A. Zadpoor. 2018. “Fatigue Performance of Additively Manufactured Meta-Biomaterials: The Effects of Topology and Material Type.” *Acta Biomaterialia* 65 (January): 292–304. https://doi.org/10.1016/J.ACTBIO.2017.11.014.

Alaña, Markel, Aitziber Lopez-Arancibia, Ainara Pradera-Mallabiabarrena, and Sergio Ruiz de Galarreta. 2019. “Analytical Model of the Elastic Behavior of a Modified Face-Centered Cubic Lattice Structure.” *Journal of the Mechanical Behavior of Biomedical Materials* 98 (October): 357–68. https://doi.org/10.1016/J.JMBBM.2019.05.043.

Al-Ketan, Oraib, Rashid K Abu Al-Rub, and Reza Rowshan. 2017. “Mechanical Properties of a New Type of Architected Interpenetrating Phase Composite Materials.” *Advanced Materials Technologies* 2 (2): 1600235. https://doi.org/https://doi.org/10.1002/admt.201600235.

Alkhader, M., and M. Vural. 2008. “Mechanical Response of Cellular Solids: Role of Cellular Topology and Microstructural Irregularity.” *International Journal of Engineering Science* 46 (10): 1035–51. https://doi.org/10.1016/J.IJENGSCI.2008.03.012.

Alves, V. A., R. Q. Reis, I. C.B. Santos, D. G. Souza, T. de, M. A. Pereira-da-Silva, A. Rossi, and L. A. da Silva. 2009. “In Situ Impedance Spectroscopy Study of the Electrochemical Corrosion of Ti and Ti–6Al–4V in Simulated Body Fluid at 25 °C and 37 °C.” *Corrosion Science* 51 (10): 2473–82. https://doi.org/10.1016/J.CORSCI.2009.06.035.

Amin Yavari, S., S. M. Ahmadi, R. Wauthle, B. Pouran, J. Schrooten, H. Weinans, and A. A. Zadpoor. 2015a. “Relationship between Unit Cell Type and Porosity and the Fatigue Behavior of Selective Laser Melted Meta-Biomaterials.” *Journal of the Mechanical Behavior of Biomedical Materials* 43 (March): 91–100. https://doi.org/10.1016/J.JMBBM.2014.12.015.

———. 2015b. “Relationship between Unit Cell Type and Porosity and the Fatigue Behavior of Selective Laser Melted Meta-Biomaterials.” *Journal of the Mechanical Behavior of Biomedical Materials* 43 (March): 91–100. https://doi.org/10.1016/J.JMBBM.2014.12.015.

Anderson, J. M. 2011. “Biocompatibility and the Relationship to Standards: Meaning and Scope of Biomaterials Testing.” *Comprehensive Biomaterials* 4 (January): 7–26. https://doi.org/10.1016/B978-0-08-055294-1.00002-7.

Arabnejad, Sajad, and Damiano Pasini. 2013. “Mechanical Properties of Lattice Materials via Asymptotic Homogenization and Comparison with Alternative Homogenization Methods.” *International Journal of Mechanical Sciences* 77 (December): 249–62. https://doi.org/10.1016/J.IJMECSCI.2013.10.003.

Arifin, Amir, Abu Bakar Sulong, Norhamidi Muhamad, Junaidi Syarif, and Mohd Ikram Ramli. 2014. “Material Processing of Hydroxyapatite and Titanium Alloy (HA/Ti) Composite as Implant Materials Using Powder Metallurgy: A Review.” *Materials & Design* 55: 165–75. https://doi.org/https://doi.org/10.1016/j.matdes.2013.09.045.

Ashby, M F. 2006. “The Properties of Foams and Lattices.” *Philosophical Transactions of the Royal Society A: Mathematical, Physical and Engineering Sciences* 364 (1838): 15–30. https://doi.org/10.1098/rsta.2005.1678.

Ashby, Michael, Tony Evans, NA Fleck, JW Hutchinson, HNG Wadley, and LJ Gibson. 2000. “Chapter 3 - Characterization Methods.” In *Metal Foams*, edited by M F Ashby, A G Evans, N A Fleck, L J Gibson, J W Hutchinson, and H N G Wadley, 24–39. Burlington: Butterworth-Heinemann. https://doi.org/https://doi.org/10.1016/B978-075067219-1/50005-2.

Bael, S. van, Y. C. Chai, S. Truscello, M. Moesen, G. Kerckhofs, H. van Oosterwyck, J. P. Kruth, and J. Schrooten. 2012. “The Effect of Pore Geometry on the in Vitro Biological Behavior of Human Periosteum-Derived Cells Seeded on Selective Laser-Melted Ti6Al4V Bone Scaffolds.” *Acta Biomaterialia* 8 (7): 2824–34. https://doi.org/10.1016/J.ACTBIO.2012.04.001.

Bael, S. van, G. Kerckhofs, M. Moesen, G. Pyka, J. Schrooten, and J. P. Kruth. 2011. “Micro-CT-Based Improvement of Geometrical and Mechanical Controllability of Selective Laser Melted Ti6Al4V Porous Structures.” *Materials Science and Engineering: A* 528 (24): 7423–31. https://doi.org/10.1016/J.MSEA.2011.06.045.

Baeslack, W A, D W Becker, and F H Froes. 1984. “Advances in Titanium Alloy Welding Metallurgy.” *JOM* 36 (5): 46–58. https://doi.org/10.1007/BF03338455.

Bagheri, Zahra S., David Melancon, Lu Liu, R. Burnett Johnston, and Damiano Pasini. 2017. “Compensation Strategy to Reduce Geometry and Mechanics Mismatches in Porous Biomaterials Built with Selective Laser Melting.” *Journal of the Mechanical Behavior of Biomedical Materials* 70 (June): 17–27. https://doi.org/10.1016/J.JMBBM.2016.04.041.

Bai, Y., S. J. Li, F. Prima, Y. L. Hao, and R. Yang. 2012. “Electrochemical Corrosion Behavior of Ti–24Nb–4Zr–8Sn Alloy in a Simulated Physiological Environment.” *Applied Surface Science* 258 (8): 4035–40. https://doi.org/10.1016/J.APSUSC.2011.12.096.

Bania, Paul J. 1994. “Beta Titanium Alloys and Their Role in the Titanium Industry.” *JOM - Journal of the Minerals, Metals and Materials Society* 46 (7): 16–19. https://doi.org/10.1007/BF03220742.

Basu, Bikramjit, Dhirendra Katti, and Ashok Kumar. 2009. *ADVANCED BIOMATERIALS Fundamentals, Processing, and Applications Edited By*. http://www.wiley.com/go/permission.www.wiley.com.

Benedetti, M., A. du Plessis, R. O. Ritchie, M. Dallago, S. M.J. Razavi, and F. Berto. 2021. “Architected Cellular Materials: A Review on Their Mechanical Properties towards Fatigue-Tolerant Design and Fabrication.” *Materials Science and Engineering: R: Reports* 144 (April): 100606. https://doi.org/10.1016/J.MSER.2021.100606.

“Biomaterials and Biomedical Materials.” 2019. *Definitions of Biomaterials for the Twenty-First Century*, January, 15–23. https://doi.org/10.1016/B978-0-12-818291-8.00002-X.

Bobbert, F S L, K Lietaert, A A Eftekhari, B Pouran, S M Ahmadi, H Weinans, and A A Zadpoor. 2017. “Additively Manufactured Metallic Porous Biomaterials Based on Minimal Surfaces: A Unique Combination of Topological, Mechanical, and Mass Transport Properties.” *Acta Biomaterialia* 53: 572–84. https://doi.org/https://doi.org/10.1016/j.actbio.2017.02.024.

BOBYN, J D, R M PILLIAR, H U CAMERON, and G C WEATHERLY. 1980. “The Optimum Pore Size for the Fixation of Porous-Surfaced Metal Implants by the Ingrowth of Bone.” *Clinical Orthopaedics and Related Research®* 150. https://journals.lww.com/clinorthop/Fulltext/1980/07000/The_Optimum_Pore_Size_for_the_Fixation_of.45.aspx.

Boniotti, L., S. Beretta, L. Patriarca, L. Rigoni, and S. Foletti. 2019. “Experimental and Numerical Investigation on Compressive Fatigue Strength of Lattice Structures of AlSi7Mg Manufactured by SLM.” *International Journal of Fatigue* 128 (November): 105181. https://doi.org/10.1016/J.IJFATIGUE.2019.06.041.

Boyer, R R, and R D Briggs. 2005. “The Use of β Titanium Alloys in the Aerospace Industry.” *Journal of Materials Engineering and Performance* 14 (6): 681–85. https://doi.org/10.1361/105994905X75448.

Callister William D., Jr. 2004. *Fundamentals of Materials Science and Engineering: An Integrated Approach, 2nd Edition*.

Campbell, F C, ed. 2008. “Elements of Metallurgy and Engineering Alloys.” ASM International. https://doi.org/10.31399/asm.tb.emea.9781627082518.

Cao, Yuankui, Weidong Zhang, Bin Liu, Min Song, and Yong Liu. 2020. “Extraordinary Tensile Properties of Titanium Alloy with Heterogeneous Phase-Distribution Based on Hetero-Deformation Induced Hardening.” *Materials Research Letters* 8 (7): 254–60. https://doi.org/10.1080/21663831.2020.1745919.

Chandra Biswas, Manik, Bodiuzzaman Jony, · Pranab, Kumar Nandy, · Reaz, Ahmed Chowdhury, Sudipta Halder, et al. 2021. “Recent Advancement of Biopolymers and Their Potential Biomedical Applications.” *Journal of Polymers and the Environment*. https://doi.org/10.1007/s10924-021-02199-y.

Chaudhuri, K, and J.~H. Perepezko. 1994. “Microstructural Study of the Titanium Alloy Ti-15Mo-2.7Nb-3Al-0.2Si (TIMETAL 21S).” *Metallurgical and Materials Transactions A* 25 (6): 1109–18. https://doi.org/10.1007/BF02652286.

Chen, Liang-Yu, Shun-Xing Liang, Yujing Liu, and Lai-Chang Zhang. 2021. “Additive Manufacturing of Metallic Lattice Structures: Unconstrained Design, Accurate Fabrication, Fascinated Performances, and Challenges.” *Materials Science and Engineering: R: Reports* 146 (October): 100648. https://doi.org/10.1016/J.MSER.2021.100648.

Cheng, Alice, David J Cohen, Adrian Kahn, Ryan M Clohessy, Kaan Sahingur, Joseph B Newton, Sharon L Hyzy, Barbara D Boyan, and Zvi Schwartz. 2017. “Laser Sintered Porous Ti–6Al–4V Implants Stimulate Vertical Bone Growth.” *Annals of Biomedical Engineering* 45 (8): 2025–35. https://doi.org/10.1007/s10439-017-1831-7.

Cheng, Alice, Aiza Humayun, David J Cohen, Barbara D Boyan, and Zvi Schwartz. 2014. “Additively Manufactured 3D Porous Ti-6Al-4V Constructs Mimic Trabecular Bone Structure and Regulate Osteoblast Proliferation, Differentiation and Local Factor Production in a Porosity and Surface Roughness Dependent Manner.” *Biofabrication* 6 (4): 045007. https://doi.org/10.1088/1758-5082/6/4/045007.

Choi, K., J. L. Kuhn, M. J. Ciarelli, and S. A. Goldstein. 1990. “The Elastic Moduli of Human Subchondral, Trabecular, and Cortical Bone Tissue and the Size-Dependency of Cortical Bone Modulus.” *Journal of Biomechanics* 23 (11):

1103–13. https://doi.org/10.1016/0021-9290(90)90003-L.

Chui, Pengfei, Ran Jing, Fenggang Zhang, Jianghua Li, and Tian Feng. 2020. "Mechanical Properties and Corrosion Behavior of β-Type Ti-Zr-Nb-Mo Alloys for Biomedical Application." *Journal of Alloys and Compounds* 842 (November): 155693. https://doi.org/10.1016/J.JALLCOM.2020.155693.

Clerk Maxwell, J. 1864. "L. On the Calculation of the Equilibrium and Stiffness of Frames." *The London, Edinburgh, and Dublin Philosophical Magazine and Journal of Science* 27 (182): 294–99. https://doi.org/10.1080/14786446408643668.

Coffin, L F. 1972. "The Effect of High Vacuum on the Low Cycle Fatigue Law." *Metallurgical and Materials Transactions B* 3 (7): 1777–88. https://doi.org/10.1007/BF02642561.

Cohen, David J, Alice Cheng, Kaan Sahingur, Ryan M Clohessy, Louis B Hopkins, Barbara D Boyan, and Zvi Schwartz. 2017. "Performance of Laser Sintered Ti–6Al–4V Implants with Bone-Inspired Porosity and Micro/Nanoscale Surface Roughness in the Rabbit Femur." *Biomedical Materials* 12 (2): 025021. https://doi.org/10.1088/1748-605X/aa6810.

Cotton, James D, Robert D Briggs, Rodney R Boyer, Sesh Tamirisakandala, Patrick Russo, Nikolay Shchetnikov, and John C Fanning. 2015. "State of the Art in Beta Titanium Alloys for Airframe Applications." *JOM* 67 (6): 1281–1303. https://doi.org/10.1007/s11837-015-1442-4.

Dai, Nianwei, Lai Chang Zhang, Junxi Zhang, Qimeng Chen, and Maoliang Wu. 2016. "Corrosion Behavior of Selective Laser Melted Ti-6Al-4 V Alloy in NaCl Solution." *Corrosion Science* 102 (January): 484–89. https://doi.org/10.1016/J.CORSCI.2015.10.041.

Dallago, M., S. Raghavendra, V. Luchin, G. Zappini, D. Pasini, and M. Benedetti. 2019. "Geometric Assessment of Lattice Materials Built via Selective Laser Melting." *Materials Today: Proceedings* 7 (January): 353–61. https://doi.org/10.1016/J.MATPR.2018.11.096.

———. 2021. "The Role of Node Fillet, Unit-Cell Size and Strut Orientation on the Fatigue Strength of Ti-6Al-4V Lattice Materials Additively Manufactured via Laser Powder Bed Fusion." *International Journal of Fatigue* 142 (January): 105946. https://doi.org/10.1016/J.IJFATIGUE.2020.105946.

Dallago, M., B. Winiarski, F. Zanini, S. Carmignato, and M. Benedetti. 2019. "On the Effect of Geometrical Imperfections and Defects on the Fatigue Strength of Cellular Lattice Structures Additively Manufactured via Selective Laser Melting." *International Journal of Fatigue* 124 (July): 348–60.

https://doi.org/10.1016/J.IJFATIGUE.2019.03.019.

DebRoy, T., H. L. Wei, J. S. Zuback, T. Mukherjee, J. W. Elmer, J. O. Milewski, A. M. Beese, A. Wilson-Heid, A. De, and W. Zhang. 2018. "Additive Manufacturing of Metallic Components – Process, Structure and Properties." *Progress in Materials Science* 92 (March): 112–224. https://doi.org/10.1016/J.PMATSCI.2017.10.001.

Deshpande, V S, M F Ashby, and N A Fleck. 2001. "Foam Topology: Bending versus Stretching Dominated Architectures." *Acta Materialia* 49 (6): 1035–40. https://doi.org/https://doi.org/10.1016/S1359-6454(00)00379-7.

Dikici, Burak, Mitsuo Niinomi, Mehmet Topuz, Serap Gungor Koc, and Masaaki Nakai. 2018. "Synthesis of Biphasic Calcium Phosphate (BCP) Coatings on B–type Titanium Alloys Reinforced with Rutile-TiO2 Compounds: Adhesion Resistance and in-Vitro Corrosion." *Journal of Sol-Gel Science and Technology* 87 (3): 713–24. https://doi.org/10.1007/s10971-018-4755-2.

Dong, Guoying, Yunlong Tang, and Yaoyao Fiona Zhao. 2017. "A Survey of Modeling of Lattice Structures Fabricated by Additive Manufacturing." *Journal of Mechanical Design* 139 (10). https://doi.org/10.1115/1.4037305.

Endo, Kaori, Satoshi Yamada, Masahiro Todoh, Masahiko Takahata, Norimasa Iwasaki, and Shigeru Tadano. 2016. "Structural Strength of Cancellous Specimens from Bovine Femur under Cyclic Compression." *PeerJ* 4 (January): e1562. https://doi.org/10.7717/peerj.1562.

Euler, Leonhard. 1746. "Thoughts on the Elements of Bodies, Memoirs of the Prussian Academy of Sciences," 1746. https://scholarlycommons.pacific.edu/euler-bap/.

Eylon, Daniel., Rodney. Boyer, Donald A. Koss, Metals and Materials Society. Titanium Committee. Minerals, and Metals and Materials Society. Annual Meeting (122nd : 1993 : Denver Minerals. 1993. *Beta Titanium Alloys in the 1990's : Proceedings of a Symposium on Beta Titanium Alloys*. Minerals, Metals & Materials Society. https://inis.iaea.org/search/search.aspx?orig_q=RN:25035790.

Facchini, Luca, Emanuele Magalini, Pierfrancesco Robotti, Alberto Molinari, Simon Höges, and Konrad Wissenbach. 2010. "Ductility of a Ti-6Al-4V Alloy Produced by Selective Laser Melting of Prealloyed Powders." *Rapid Prototyping Journal* 16 (6): 450–59. https://doi.org/10.1108/13552541011083371.

François, Dominique, André Pineau, and André Zaoui. 2013. "Fatigue." In *Mechanical Behaviour of Materials: Volume II: Fracture Mechanics and Damage*, 307–62.

Dordrecht: Springer Netherlands. https://doi.org/10.1007/978-94-007-4930-6_6.

Frazier, William E. 2014. “Metal Additive Manufacturing: A Review.” *Journal of Materials Engineering and Performance* 23 (6): 1917–28. https://doi.org/10.1007/s11665-014-0958-z.

Freese, Howard L, Michael G Volas, and J Randolph Wood. 2001. “Metallurgy and Technological Properties of Titanium and Titanium Alloys.” In *Titanium in Medicine: Material Science, Surface Science, Engineering, Biological Responses and Medical Applications*, 25–51. Berlin, Heidelberg: Springer Berlin Heidelberg. https://doi.org/10.1007/978-3-642-56486-4_3.

Geetha, M., A. K. Singh, R. Asokamani, and A. K. Gogia. 2009. “Ti Based Biomaterials, the Ultimate Choice for Orthopaedic Implants – A Review.” *Progress in Materials Science* 54 (3): 397–425. https://doi.org/10.1016/J.PMATSCI.2008.06.004.

Ghouse, Shaaz, Sarat Babu, Richard J. van Arkel, Kenneth Nai, Paul A. Hooper, and Jonathan R.T. Jeffers. 2017. “The Influence of Laser Parameters and Scanning Strategies on the Mechanical Properties of a Stochastic Porous Material.” *Materials & Design* 131 (October): 498–508. https://doi.org/10.1016/J.MATDES.2017.06.041.

Ghouse, Shaaz, Sarat Babu, Kenneth Nai, Paul A. Hooper, and Jonathan R.T. Jeffers. 2018. “The Influence of Laser Parameters, Scanning Strategies and Material on the Fatigue Strength of a Stochastic Porous Structure.” *Additive Manufacturing* 22 (August): 290–301. https://doi.org/10.1016/J.ADDMA.2018.05.024.

Gibson, L J. 2000. “Mechanical Behavior of Metallic Foams.” *Annual Review of Materials Science* 30 (1): 191–227. https://doi.org/10.1146/annurev.matsci.30.1.191.

Gibson, L J, M F Ashby, and B A Harley. 2010. *Cellular Materials in Nature and Medicine*. Cellular Materials in Nature and Medicine. Cambridge University Press. https://books.google.it/books?id=AKxiS4AKpyEC.

Gibson, L J, Michael Farries Ashby, G S Schajer, and C I Robertson. 1982. “The Mechanics of Two-Dimensional Cellular Materials.” *Proceedings of the Royal Society of London. A. Mathematical and Physical Sciences* 382 (1782): 25–42. https://doi.org/10.1098/rspa.1982.0087.

Gibson, Lorna J., and Michael F. Ashby. 1997. *Cellular Solids*. Cambridge University Press. https://doi.org/10.1017/CBO9781139878326.

Goguitchaichvili, Avto, Verónica Ortega, Jorge Archer, Juan Morales, and Anuar Teran Guerrero. 2017. “Absolute Geomagnetic Intensity Record from Pre-Columbian Pottery Dates Elite Tlailotlacan Woman in Ancient Teotihuacan.” *Journal of Archaeological Science: Reports* 14 (August): 146–51. https://doi.org/10.1016/J.JASREP.2017.05.030.

González, Fernando José Quevedo, and Natalia Nuño. 2016. “Finite Element Modelling Approaches for Well-Ordered Porous Metallic Materials for Orthopaedic Applications: Cost Effectiveness and Geometrical Considerations.” *Computer Methods in Biomechanics and Biomedical Engineering* 19 (8): 845–54. https://doi.org/10.1080/10255842.2015.1075009.

Gordon, Jerard v, Sneha P Narra, Ross W Cunningham, He Liu, Hangman Chen, Robert M Suter, Jack L Beuth, and Anthony D Rollett. 2020. “Defect Structure Process Maps for Laser Powder Bed Fusion Additive Manufacturing.” *Additive Manufacturing* 36: 101552. https://doi.org/https://doi.org/10.1016/j.addma.2020.101552.

Haftlang, Farahnaz, Abbas Zarei-Hanzaki, and Hamid Reza Abedi. 2020. “The Effect of Nano-Size Second Precipitates on the Structure, Apatite-Inducing Ability and in-Vitro Biocompatibility of Ti-29Nb-14Ta-4.5Zr Alloy.” *Materials Science and Engineering: C* 109 (April): 110561. https://doi.org/10.1016/J.MSEC.2019.110561.

Hanawa, T. 2010. “Overview of Metals and Applications.” *Metals for Biomedical Devices*, January, 3–24. https://doi.org/10.1533/9781845699246.1.3.

Hasan, Anwarul, Batzaya Byambaa, Mahboob Morshed, Mohammad Ibrahim Cheikh, Rana Abdul Shakoor, Tanvir Mustafy, and Hany E Marei. 2018. “Advances in Osteobiologic Materials for Bone Substitutes.” *Journal of Tissue Engineering and Regenerative Medicine* 12 (6): 1448–68. https://doi.org/https://doi.org/10.1002/term.2677.

Hashin, Z. 1983. “Analysis of Composite Materials—A Survey.” *Journal of Applied Mechanics* 50 (3): 481–505. https://doi.org/10.1115/1.3167081.

Hedayati, R., S. Janbaz, M. Sadighi, M. Mohammadi-Aghdam, and A. A. Zadpoor. 2017. “How Does Tissue Regeneration Influence the Mechanical Behavior of Additively Manufactured Porous Biomaterials?” *Journal of the Mechanical Behavior of Biomedical Materials* 65 (January): 831–41. https://doi.org/10.1016/J.JMBBM.2016.10.003.

Heo, Hyeonu, Jaehyung Ju, and Doo-Man Kim. 2013. “Compliant Cellular Structures: Application to a Passive Morphing Airfoil.” *Composite Structures* 106: 560–69. https://doi.org/https://doi.org/10.1016/j.compstruct.2013.07.013.

Hollister, S J, and N Kikuchi. 1992. “A Comparison of Homogenization and Standard Mechanics Analyses for Periodic Porous Composites.” *Computational Mechanics* 10 (2): 73–95. https://doi.org/10.1007/BF00369853.

Hollister, Scott J. 2005. “Porous Scaffold Design for Tissue Engineering.” *Nature Materials* 4 (7): 518–24. https://doi.org/10.1038/nmat1421.

Holzapfel, Boris Michael, Johannes Christian Reichert, Jan Thorsten Schantz, Uwe Gbureck, Lars Rackwitz, Ulrich Nöth, Franz Jakob, Maximilian Rudert, Jürgen Groll, and Dietmar Werner Hutmacher. 2013. “How Smart Do Biomaterials Need to Be? A Translational Science and Clinical Point of View.” *Advanced Drug Delivery Reviews* 65 (4): 581–603. https://doi.org/10.1016/J.ADDR.2012.07.009.

Hooreweder, Brecht van, Yanni Apers, Karel Lietaert, and Jean Pierre Kruth. 2017a. “Improving the Fatigue Performance of Porous Metallic Biomaterials Produced by Selective Laser Melting.” *Acta Biomaterialia* 47 (January): 193–202. https://doi.org/10.1016/J.ACTBIO.2016.10.005.

———. 2017b. “Improving the Fatigue Performance of Porous Metallic Biomaterials Produced by Selective Laser Melting.” *Acta Biomaterialia* 47 (January): 193–202. https://doi.org/10.1016/J.ACTBIO.2016.10.005.

Huang, J., and S. M. Best. 2007. “Ceramic Biomaterials.” *Tissue Engineering Using Ceramics and Polymers*, January, 3–31. https://doi.org/10.1533/9781845693817.1.3.

Huda, Zainul, and Prasetyo Edi. 2013. “Materials Selection in Design of Structures and Engines of Supersonic Aircrafts: A Review.” *Materials & Design* 46 (April): 552–60. https://doi.org/10.1016/J.MATDES.2012.10.001.

Ibrahim, Hamdy, Sajedeh Nasr Esfahani, Behrang Poorganji, David Dean, and Mohammad Elahinia. 2017. “Resorbable Bone Fixation Alloys, Forming, and Post-Fabrication Treatments.” *Materials Science and Engineering: C* 70 (January): 870–88. https://doi.org/10.1016/J.MSEC.2016.09.069.

Ishimoto, Takuya, Koji Hagihara, Kenta Hisamoto, Shi-Hai Sun, and Takayoshi Nakano. 2017. “Crystallographic Texture Control of Beta-Type Ti–15Mo–5Zr–3Al Alloy by Selective Laser Melting for the Development of Novel Implants with a Biocompatible Low Young’s Modulus.” *Scripta Materialia* 132: 34–38. https://doi.org/https://doi.org/10.1016/j.scriptamat.2016.12.038.

Ivasishin, Orest M, Pavlo E Markovsky, R v Teliovich, and Yu.V. Matviychuk. 2000. “STA Heat Treatment of Beta-Titanium Alloys after Various Thermomechanical Processing.” In *Development in Light Metals*, 188:63–72. Key Engineering Materials. Trans Tech Publications Ltd.

https://doi.org/10.4028/www.scientific.net/KEM.188.63.

Kadkhodapour, J., H. Montazerian, A. Ch Darabi, A. P. Anaraki, S. M. Ahmadi, A. A. Zadpoor, and S. Schmauder. 2015. "Failure Mechanisms of Additively Manufactured Porous Biomaterials: Effects of Porosity and Type of Unit Cell." *Journal of the Mechanical Behavior of Biomedical Materials* 50 (October): 180–91. https://doi.org/10.1016/J.JMBBM.2015.06.012.

Kang, Nan, Yunlong Li, Xin Lin, Enhao Feng, and Weidong Huang. 2019. "Microstructure and Tensile Properties of Ti-Mo Alloys Manufactured via Using Laser Powder Bed Fusion." *Journal of Alloys and Compounds* 771 (January): 877–84. https://doi.org/10.1016/J.JALLCOM.2018.09.008.

Kelly, Cambre N., Jaedyn Francovich, S. Julmi, David Safranski, Robert E. Guldberg, Hans J. Maier, and Ken Gall. 2019. "Fatigue Behavior of As-Built Selective Laser Melted Titanium Scaffolds with Sheet-Based Gyroid Microarchitecture for Bone Tissue Engineering." *Acta Biomaterialia* 94 (August): 610–26. https://doi.org/10.1016/J.ACTBIO.2019.05.046.

Khalili, Amelia Ahmad, and Mohd Ridzuan Ahmad. 2015. "A Review of Cell Adhesion Studies for Biomedical and Biological Applications." *International Journal of Molecular Sciences* 16 (8): 18149–84. https://doi.org/10.3390/ijms160818149.

Kokubo, Tadashi, and Seiji Yamaguchi. 2016. "Novel Bioactive Materials Developed by Simulated Body Fluid Evaluation: Surface-Modified Ti Metal and Its Alloys." *Acta Biomaterialia* 44 (October): 16–30. https://doi.org/10.1016/J.ACTBIO.2016.08.013.

Kolken, H. M.A., A. Fontecha Garcia, A. du Plessis, C. Rans, M. J. Mirzaali, and A. A. Zadpoor. 2021a. "Fatigue Performance of Auxetic Meta-Biomaterials." *Acta Biomaterialia* 126 (May): 511–23. https://doi.org/10.1016/J.ACTBIO.2021.03.015.

———. 2021b. "Fatigue Performance of Auxetic Meta-Biomaterials." *Acta Biomaterialia* 126 (May): 511–23. https://doi.org/10.1016/J.ACTBIO.2021.03.015.

Kolli, R Prakash, and Arun Devaraj. 2018. "A Review of Metastable Beta Titanium Alloys." *Metals* 8 (7). https://doi.org/10.3390/met8070506.

Kong, Weihuan, Sophie C Cox, Yu Lu, Victor Villapun, Xiaoling Xiao, Wenyou Ma, Min Liu, and Moataz M Attallah. 2021. "The Influence of Zirconium Content on the Microstructure, Mechanical Properties, and Biocompatibility of in-Situ Alloying Ti-Nb-Ta Based β Alloys Processed by Selective Laser Melting." *Materials Science and Engineering: C* 131: 112486. https://doi.org/https://doi.org/10.1016/j.msec.2021.112486.

Kuhn, Liisa T. 2005. “6 - BIOMATERIALS.” In *Biomedical Engineering*, edited by John D Enderle, Susan M Blanchard, and Joseph D B T - Introduction to Biomedical Engineering (Second Edition) Bronzino, 255–312. Boston: Academic Press. https://doi.org/https://doi.org/10.1016/B978-0-12-238662-6.50008-2.

Kumar Sadasivuni, Kishor, Prosenjit Saha, Jaideep Adhikari, Kalim Deshmukh, M Basheer Ahamed, and John-John Cabibihan. 2019. “Recent Advances in Mechanical Properties of Biopolymer Composites: A Review.” https://doi.org/10.1002/pc.25356.

Kumar, Satendra, and T. S.N. Sankara Narayanan. 2009. “Electrochemical Characterization of β-Ti Alloy in Ringer’s Solution for Implant Application.” *Journal of Alloys and Compounds* 479 (1–2): 699–703. https://doi.org/10.1016/J.JALLCOM.2009.01.036.

Ladino, Lady Diana, Gary Hunter, and José Francisco Téllez-Zenteno. 2013. “Art and Epilepsy Surgery.” *Epilepsy & Behavior* 29 (1): 82–89. https://doi.org/10.1016/J.YEBEH.2013.06.028.

Leary, M. 2018. “3.1 - Design of Titanium Implants for Additive Manufacturing.” In *Titanium in Medical and Dental Applications*, edited by Francis H Froes and Ma Qian, 203–24. Woodhead Publishing Series in Biomaterials. Woodhead Publishing. https://doi.org/https://doi.org/10.1016/B978-0-12-812456-7.00009-3.

Lefebvre, L P, E Baril, and M N Bureau. 2009. “Effect of the Oxygen Content in Solution on the Static and Cyclic Deformation of Titanium Foams.” *Journal of Materials Science: Materials in Medicine* 20 (11): 2223. https://doi.org/10.1007/s10856-009-3798-x.

Lin, Jixing, Sertan Ozan, Khurram Munir, Kun Wang, Xian Tong, Yuncang Li, Guangyu Li, and Cuie Wen. 2017. “Effects of Solution Treatment and Aging on the Microstructure{,} Mechanical Properties{,} and Corrosion Resistance of a β Type Ti–Ta–Hf–Zr Alloy.” *RSC Adv.* 7 (20): 12309–17. https://doi.org/10.1039/C6RA28464G.

Linder, L, A Carlsson, L Marsal, L M Bjursten, and P I Branemark. 1988. “Clinical Aspects of Osseointegration in Joint Replacement. A Histological Study of Titanium Implants.” *The Journal of Bone and Joint Surgery. British Volume* 70-B (4): 550–55. https://doi.org/10.1302/0301-620X.70B4.3403596.

Liu, Lu, Paul Kamm, Francisco García-Moreno, John Banhart, and Damiano Pasini. 2017. “Elastic and Failure Response of Imperfect Three-Dimensional Metallic Lattices: The Role of Geometric Defects Induced by Selective Laser Melting.” *Journal of the Mechanics and Physics of Solids* 107 (October): 160–84.

https://doi.org/10.1016/J.JMPS.2017.07.003.

Liu, Y. J., S. J. Li, H. L. Wang, W. T. Hou, Y. L. Hao, R. Yang, T. B. Sercombe, and L. C. Zhang. 2016. "Microstructure, Defects and Mechanical Behavior of Beta-Type Titanium Porous Structures Manufactured by Electron Beam Melting and Selective Laser Melting." *Acta Materialia* 113 (July): 56–67. https://doi.org/10.1016/J.ACTAMAT.2016.04.029.

Liu, Y. J., D. C. Ren, S. J. Li, H. Wang, L. C. Zhang, and T. B. Sercombe. 2020. "Enhanced Fatigue Characteristics of a Topology-Optimized Porous Titanium Structure Produced by Selective Laser Melting." *Additive Manufacturing* 32 (March): 101060. https://doi.org/10.1016/J.ADDMA.2020.101060.

Liu, Y. J., H. L. Wang, S. J. Li, S. G. Wang, W. J. Wang, W. T. Hou, Y. L. Hao, R. Yang, and L. C. Zhang. 2017. "Compressive and Fatigue Behavior of Beta-Type Titanium Porous Structures Fabricated by Electron Beam Melting." *Acta Materialia* 126 (March): 58–66. https://doi.org/10.1016/J.ACTAMAT.2016.12.052.

Lopez-Heredia, M A, E Goyenvalle, E Aguado, P Pilet, C Leroux, M Dorget, P Weiss, and P Layrolle. 2008. "Bone Growth in Rapid Prototyped Porous Titanium Implants." *Journal of Biomedical Materials Research Part A* 85A (3): 664–73. https://doi.org/https://doi.org/10.1002/jbm.a.31468.

Luo, J. P., Y. J. Huang, J. Y. Xu, J. F. Sun, M. S. Dargusch, C. H. Hou, L. Ren, R. Z. Wang, T. Ebel, and M. Yan. 2020. "Additively Manufactured Biomedical Ti-Nb-Ta-Zr Lattices with Tunable Young's Modulus: Mechanical Property, Biocompatibility, and Proteomics Analysis." *Materials Science and Engineering: C* 114 (September): 110903. https://doi.org/10.1016/J.MSEC.2020.110903.

Luo, J. P., J. F. Sun, Y. J. Huang, J. H. Zhang, D. P. Zhao, M. Yan, and Y. D. Zhang. 2019. "Low-Modulus Biomedical Ti–30Nb–5Ta–3Zr Additively Manufactured by Selective Laser Melting and Its Biocompatibility." *Materials Science and Engineering: C* 97 (April): 275–84. https://doi.org/10.1016/J.MSEC.2018.11.077.

Lütjering, Gerd, and James C Williams, eds. 2007. "Beta Alloys BT - Titanium." In , 283–336. Berlin, Heidelberg: Springer Berlin Heidelberg. https://doi.org/10.1007/978-3-540-73036-1_7.

Luxner, Mathias H, Juergen Stampfl, and Heinz E Pettermann. 2005. "Finite Element Modeling Concepts and Linear Analyses of 3D Regular Open Cell Structures." *Journal of Materials Science* 40 (22): 5859–66. https://doi.org/10.1007/s10853-005-5020-y.

Maconachie, Tobias, Martin Leary, Bill Lozanovski, Xuezhe Zhang, Ma Qian, Omar Faruque, and Milan Brandt. 2019. “SLM Lattice Structures: Properties, Performance, Applications and Challenges.” *Materials & Design* 183: 108137. https://doi.org/https://doi.org/10.1016/j.matdes.2019.108137.

Mantri, S. A., D. Choudhuri, T. Alam, G. B. Viswanathan, J. M. Sosa, H. L. Fraser, and R. Banerjee. 2018. “Tuning the Scale of α Precipitates in β-Titanium Alloys for Achieving High Strength.” *Scripta Materialia* 154 (September): 139–44. https://doi.org/10.1016/J.SCRIPTAMAT.2018.05.040.

Markhoff, Jana, Jan Wieding, Volker Weissmann, Juliane Pasold, Anika Jonitz-Heincke, and Rainer Bader. 2015. “Influence of Different Three-Dimensional Open Porous Titanium Scaffold Designs on Human Osteoblasts Behavior in Static and Dynamic Cell Investigations.” *Materials* 8 (8): 5490–5507. https://doi.org/10.3390/ma8085259.

McMahon, Rebecca E., Ji Ma, Stanislav v. Verkhoturov, Dany Munoz-Pinto, Ibrahim Karaman, Felix Rubitschek, Hans J. Maier, and Mariah S. Hahn. 2012. “A Comparative Study of the Cytotoxicity and Corrosion Resistance of Nickel–Titanium and Titanium–Niobium Shape Memory Alloys.” *Acta Biomaterialia* 8 (7): 2863–70. https://doi.org/10.1016/J.ACTBIO.2012.03.034.

Michielsen, K, and J S Kole. 2003. “Photonic Band Gaps in Materials with Triply Periodic Surfaces and Related Tubular Structures.” *Phys. Rev. B* 68 (11): 115107. https://doi.org/10.1103/PhysRevB.68.115107.

Moges, Tesfaye, Gaurav Ameta, and Paul Witherell. 2019. “A Review of Model Inaccuracy and Parameter Uncertainty in Laser Powder Bed Fusion Models and Simulations.” *Journal of Manufacturing Science and Engineering* 141 (4). https://doi.org/10.1115/1.4042789.

Moussa, Ahmed, David Melancon, Asma el Elmi, and Damiano Pasini. 2021. “Topology Optimization of Imperfect Lattice Materials Built with Process-Induced Defects via Powder Bed Fusion.” *Additive Manufacturing* 37 (January): 101608. https://doi.org/10.1016/J.ADDMA.2020.101608.

Mullen, Lewis, Robin C Stamp, Wesley K Brooks, Eric Jones, and Christopher J Sutcliffe. 2009. “Selective Laser Melting: A Regular Unit Cell Approach for the Manufacture of Porous, Titanium, Bone in-Growth Constructs, Suitable for Orthopedic Applications.” *Journal of Biomedical Materials Research Part B: Applied Biomaterials* 89B (2): 325–34. https://doi.org/https://doi.org/10.1002/jbm.b.31219.

Murchio, S., M. Dallago, F. Zanini, S. Carmignato, G. Zappini, F. Berto, D. Maniglio, and M. Benedetti. 2021. “Additively Manufactured Ti–6Al–4V Thin Struts via

Laser Powder Bed Fusion: Effect of Building Orientation on Geometrical Accuracy and Mechanical Properties." *Journal of the Mechanical Behavior of Biomedical Materials* 119 (July): 104495. https://doi.org/10.1016/J.JMBBM.2021.104495.

Murr, L E. 2017. "Open-Cellular Metal Implant Design and Fabrication for Biomechanical Compatibility with Bone Using Electron Beam Melting." *Journal of the Mechanical Behavior of Biomedical Materials* 76: 164–77. https://doi.org/https://doi.org/10.1016/j.jmbbm.2017.02.019.

Murr, Lawrence E. 2019. "Strategies for Creating Living, Additively Manufactured, Open-Cellular Metal and Alloy Implants by Promoting Osseointegration, Osteoinduction and Vascularization: An Overview." *Journal of Materials Science & Technology* 35 (2): 231–41. https://doi.org/10.1016/J.JMST.2018.09.003.

Naini, F. B., M. T. Cobourne, F. McDonald, and A. N.A. Donaldson. 2008. "The Influence of Craniofacial to Standing Height Proportion on Perceived Attractiveness." *International Journal of Oral and Maxillofacial Surgery* 37 (10): 877–85. https://doi.org/10.1016/J.IJOM.2008.07.022.

Narayan, Roger J, ed. 2012. "Materials for Medical Devices." ASM International. https://doi.org/10.31399/asm.hb.v23.9781627081986.

Niendorf, Thomas, Florian Brenne, and Mirko Schaper. 2014. "Lattice Structures Manufactured by SLM: On the Effect of Geometrical Dimensions on Microstructure Evolution During Processing." *Metallurgical and Materials Transactions B* 45 (4): 1181–85. https://doi.org/10.1007/s11663-014-0086-z.

Nishimura, T, M Nishigaki, and H Kusamichi. 1982. "Aging Characteristics of Beta Titanium Alloys." In *Titanium and Titanium Alloys: Scientific and Technological Aspects Volume 3*, edited by J C Williams and A F Belov, 1675–89. Boston, MA: Springer US. https://doi.org/10.1007/978-1-4757-1758-7_6.

O'Regan, Paul, Paul Prickett, Rossi Setchi, Gareth Hankins, and Nick Jones. 2016. "Metal Based Additive Layer Manufacturing: Variations, Correlations and Process Control." *Procedia Computer Science* 96 (January): 216–24. https://doi.org/10.1016/J.PROCS.2016.08.134.

Özbilen, Sedat, Daniela Liebert, Tilmann Beck, and Martin Bram. 2016. "Fatigue Behavior of Highly Porous Titanium Produced by Powder Metallurgy with Temporary Space Holders." *Materials Science and Engineering: C* 60 (March): 446–57. https://doi.org/10.1016/J.MSEC.2015.11.050.

Peters, M, J Hemptenmacher, J Kumpfert, and C Leyens. 2003. "Structure and Properties of Titanium and Titanium Alloys." In *Titanium and Titanium Alloys*,

1–36. John Wiley & Sons, Ltd. https://doi.org/https://doi.org/10.1002/3527602119.ch1.

Pyka, Grzegorz, Greet Kerckhofs, Ioannis Papantoniou, Mathew Speirs, Jan Schrooten, and Martine Wevers. 2013. “Surface Roughness and Morphology Customization of Additive Manufactured Open Porous Ti6Al4V Structures.” *Materials* 6 (10): 4737–57. https://doi.org/10.3390/ma6104737.

Qin, Peng, Yang Chen, Yu-Jing Liu, Junxi Zhang, Liang-Yu Chen, Yuhua Li, Xuhui Zhang, Chongde Cao, Hongqi Sun, and Lai-Chang Zhang. 2019. “Resemblance in Corrosion Behavior of Selective Laser Melted and Traditional Monolithic β Ti-24Nb-4Zr-8Sn Alloy.” *ACS Biomaterials Science & Engineering* 5 (2): 1141–49. https://doi.org/10.1021/acsbiomaterials.8b01341.

Qiu, Chunlei, Sheng Yue, Nicholas J.E. Adkins, Mark Ward, Hany Hassanin, Peter D. Lee, Philip J. Withers, and Moataz M. Attallah. 2015. “Influence of Processing Conditions on Strut Structure and Compressive Properties of Cellular Lattice Structures Fabricated by Selective Laser Melting.” *Materials Science and Engineering: A* 628 (March): 188–97. https://doi.org/10.1016/J.MSEA.2015.01.031.

Raghavendra, Sunil, Alberto Molinari, Michele Dallago, Gianluca Zappini, Filippo Zanini, Simone Carmignato, and Matteo Benedetti. 2021a. “Uniaxial Static Mechanical Properties of Regular, Irregular and Random Additively Manufactured Cellular Materials: Nominal vs. Real Geometry.” *Forces in Mechanics* 2 (July): 100007. https://doi.org/10.1016/J.FINMEC.2020.100007.

———. 2021b. “Uniaxial Static Mechanical Properties of Regular, Irregular and Random Additively Manufactured Cellular Materials: Nominal vs. Real Geometry.” *Forces in Mechanics* 2 (July): 100007. https://doi.org/10.1016/J.FINMEC.2020.100007.

Raghavendra, Sunil, Alberto Molinari, Vigilio Fontanari, Michele Dallago, Valerio Luchin, Gianluca Zappini, and Matteo Benedetti. 2020. “Tension-Compression Asymmetric Mechanical Behaviour of Lattice Cellular Structures Produced by Selective Laser Melting.” *Proceedings of the Institution of Mechanical Engineers, Part C: Journal of Mechanical Engineering Science* 234 (16): 3241–56. https://doi.org/10.1177/0954406220912786.

Rehme, O, C Emmelmann, and E Beyer. 2005. “Reproducibility for Properties of Selective Laser Melting Products, INTERNATIONAL CONFERENCE; 3rd, Lasers in Manufacturing; LIM 2005.” In *Lasers in Manufacturing; LIM 2005, LASERS IN MANUFACTURING -WLT CONFERENCE- CD-ROM EDITION-, INTERNATIONAL CONFERENCE; 3rd, Lasers in Manufacturing; LIM 2005*, 227–32. Stuttgart: AT-Verlag;

https://www.tib.eu/de/suchen/id/BLCP%3ACN068599180.

Reinhart, Gunther, Stefan Teufelhart, and Fabian Riss. 2012. “Investigation of the Geometry-Dependent Anisotropic Material Behavior of Filigree Struts in ALM-Produced Lattice Structures.” *Physics Procedia* 39 (January): 471–79. https://doi.org/10.1016/J.PHPRO.2012.10.063.

Rho, Jae Young, Richard B. Ashman, and Charles H. Turner. 1993a. “Young’s Modulus of Trabecular and Cortical Bone Material: Ultrasonic and Microtensile Measurements.” *Journal of Biomechanics* 26 (2): 111–19. https://doi.org/10.1016/0021-9290(93)90042-D.

———. 1993b. “Young’s Modulus of Trabecular and Cortical Bone Material: Ultrasonic and Microtensile Measurements.” *Journal of Biomechanics* 26 (2): 111–19. https://doi.org/10.1016/0021-9290(93)90042-D.

Rho, Jae Young, Liisa Kuhn-Spearing, and Peter Zioupos. 1998. “Mechanical Properties and the Hierarchical Structure of Bone.” *Medical Engineering & Physics* 20 (2): 92–102. https://doi.org/10.1016/S1350-4533(98)00007-1.

Rubenchik, Alexander M., Wayne E. King, and Sheldon S. Wu. 2018. “Scaling Laws for the Additive Manufacturing.” *Journal of Materials Processing Technology* 257 (July): 234–43. https://doi.org/10.1016/J.JMATPROTEC.2018.02.034.

Ruiz de Galarreta, Sergio, Jonathan R.T. Jeffers, and Shaaz Ghouse. 2020. “A Validated Finite Element Analysis Procedure for Porous Structures.” *Materials & Design* 189 (April): 108546. https://doi.org/10.1016/J.MATDES.2020.108546.

Salernitano, E, and C Migliaresi. 2003. “Composite Materials for Biomedical Applications: A Review.” *Journal of Applied Biomaterials and Biomechanics* 1 (1): 3–18. https://doi.org/10.1177/228080000300100102.

Sansoz, F, M Almesallmy, and H Ghonem. 2004. “Ductility Exhaustion Mechanisms in Thermally Exposed Thin Sheets of a Near-β Titanium Alloy.” *Metallurgical and Materials Transactions A* 35 (10): 3113–27. https://doi.org/10.1007/s11661-004-0056-1.

Schijve, J. 2003. “Fatigue of Structures and Materials in the 20th Century and the State of the Art.” *International Journal of Fatigue* 25 (8): 679–702. https://doi.org/10.1016/S0142-1123(03)00051-3.

Schijve, Jaap. 2009. “Fatigue as a Phenomenon in the Material.” In *Fatigue of Structures and Materials*, edited by Jaap Schijve, 13–58. Dordrecht: Springer Netherlands. https://doi.org/10.1007/978-1-4020-6808-9_2.

Schmidt, Michael, Marion Merklein, David Bourell, Dimitri Dimitrov, Tino Hausotte,

Konrad Wegener, Ludger Overmeyer, Frank Vollertsen, and Gideon N. Levy. 2017. “Laser Based Additive Manufacturing in Industry and Academia.” *CIRP Annals* 66 (2): 561–83. https://doi.org/10.1016/J.CIRP.2017.05.011.

Schwarz, H A. 1890. *Gesammelte Mathematische Abhandlungen*. Gesammelte Mathematische Abhandlungen. J. Springer. https://books.google.it/books?id=hmYJAAAAIAAJ.

Sevilla, P., C. Aparicio, J. A. Planell, and F. J. Gil. 2007. “Comparison of the Mechanical Properties between Tantalum and Nickel–Titanium Foams Implant Materials for Bone Ingrowth Applications.” *Journal of Alloys and Compounds* 439 (1–2): 67–73. https://doi.org/10.1016/J.JALLCOM.2006.08.069.

Shahzamanian, M M, T Tadepalli, A M Rajendran, W D Hodo, R Mohan, R Valisetty, P W Chung, and J J Ramsey. 2013. “Representative Volume Element Based Modeling of Cementitious Materials.” *Journal of Engineering Materials and Technology* 136 (1). https://doi.org/10.1115/1.4025916.

Sharir, Amnon, Meir Max Barak, and Ron Shahar. 2008. “Whole Bone Mechanics and Mechanical Testing.” *The Veterinary Journal* 177 (1): 8–17. https://doi.org/10.1016/J.TVJL.2007.09.012.

Simsek, Ijlal, and Dursun Ozyurek. 2019. “Investigation of the Wear and Corrosion Behaviors of Ti5Al2.5Fe and Ti6Al4V Alloys Produced by Mechanical Alloying Method in Simulated Body Fluid Environment.” *Materials Science and Engineering: C* 94 (January): 357–63. https://doi.org/10.1016/J.MSEC.2018.09.047.

Sing, Swee Leong, Florencia Edith Wiria, and Wai Yee Yeong. 2018. “Selective Laser Melting of Lattice Structures: A Statistical Approach to Manufacturability and Mechanical Behavior.” *Robotics and Computer-Integrated Manufacturing* 49 (February): 170–80. https://doi.org/10.1016/J.RCIM.2017.06.006.

Sing, Swee Leong, Wai Yee Yeong, and Florencia Edith Wiria. 2016. “Selective Laser Melting of Titanium Alloy with 50 Wt% Tantalum: Microstructure and Mechanical Properties.” *Journal of Alloys and Compounds* 660: 461–70. https://doi.org/https://doi.org/10.1016/j.jallcom.2015.11.141.

Smith, M., Z. Guan, and W. J. Cantwell. 2013. “Finite Element Modelling of the Compressive Response of Lattice Structures Manufactured Using the Selective Laser Melting Technique.” *International Journal of Mechanical Sciences* 67 (February): 28–41. https://doi.org/10.1016/J.IJMECSCI.2012.12.004.

Stephens, R I, A Fatemi, R R Stephens, and H O Fuchs. 2000. *Metal Fatigue in*

Engineering. A Wiley-Interscience Publication. Wiley. https://books.google.it/books?id=B2aAPVa1TIoC.

Strano, Giovanni, Liang Hao, Richard M. Everson, and Kenneth E. Evans. 2013. "Surface Roughness Analysis, Modelling and Prediction in Selective Laser Melting." *Journal of Materials Processing Technology* 213 (4): 589–97. https://doi.org/10.1016/J.JMATPROTEC.2012.11.011.

Suresh, S. 1998. *Fatigue of Materials*. Cambridge University Press. https://doi.org/10.1017/CBO9780511806575.

Takematsu, E., K. Katsumata, K. Okada, M. Niinomi, and N. Matsushita. 2016. "Bioactive Surface Modification of Ti–29Nb–13Ta–4.6Zr Alloy through Alkali Solution Treatments." *Materials Science and Engineering: C* 62 (May): 662–67. https://doi.org/10.1016/J.MSEC.2016.01.041.

Tan, X. P., Y. J. Tan, C. S.L. Chow, S. B. Tor, and W. Y. Yeong. 2017. "Metallic Powder-Bed Based 3D Printing of Cellular Scaffolds for Orthopaedic Implants: A State-of-the-Art Review on Manufacturing, Topological Design, Mechanical Properties and Biocompatibility." *Materials Science and Engineering: C* 76 (July): 1328–43. https://doi.org/10.1016/J.MSEC.2017.02.094.

Taniguchi, Naoya, Shunsuke Fujibayashi, Mitsuru Takemoto, Kiyoyuki Sasaki, Bungo Otsuki, Takashi Nakamura, Tomiharu Matsushita, Tadashi Kokubo, and Shuichi Matsuda. 2016a. "Effect of Pore Size on Bone Ingrowth into Porous Titanium Implants Fabricated by Additive Manufacturing: An in Vivo Experiment." *Materials Science and Engineering: C* 59: 690–701. https://doi.org/https://doi.org/10.1016/j.msec.2015.10.069.

———. 2016b. "Effect of Pore Size on Bone Ingrowth into Porous Titanium Implants Fabricated by Additive Manufacturing: An in Vivo Experiment." *Materials Science and Engineering: C* 59 (February): 690–701. https://doi.org/10.1016/J.MSEC.2015.10.069.

Tong, Xian, Quanxiang Sun, Dechuang Zhang, Kun Wang, Yilong Dai, Zimu Shi, Yuncang Li, et al. 2021. "Impact of Scandium on Mechanical Properties, Corrosion Behavior, Friction and Wear Performance, and Cytotoxicity of a β-Type Ti–24Nb–38Zr–2Mo Alloy for Orthopedic Applications." *Acta Biomaterialia* 134 (October): 791–803. https://doi.org/10.1016/J.ACTBIO.2021.07.061.

Vandenbroucke, Ben, and Jean-Pierre Kruth. 2007. "Selective Laser Melting of Biocompatible Metals for Rapid Manufacturing of Medical Parts." *Rapid Prototyping Journal* 13 (4): 196–203. https://doi.org/10.1108/13552540710776142.

Veyhl, C., I. v. Belova, G. E. Murch, and T. Fiedler. 2011. “Finite Element Analysis of the Mechanical Properties of Cellular Aluminium Based on Micro-Computed Tomography.” *Materials Science and Engineering: A* 528 (13–14): 4550–55. https://doi.org/10.1016/J.MSEA.2011.02.031.

Vock, Silvia, Burghardt Klöden, Alexander Kirchner, Thomas Weißgärber, and Bernd Kieback. 2019. “Powders for Powder Bed Fusion: A Review.” *Progress in Additive Manufacturing* 4 (4): 383–97. https://doi.org/10.1007/s40964-019-00078-6.

Vrancken, B., L. Thijs, J. P. Kruth, and J. van Humbeeck. 2014. “Microstructure and Mechanical Properties of a Novel β Titanium Metallic Composite by Selective Laser Melting.” *Acta Materialia* 68 (April): 150–58. https://doi.org/10.1016/J.ACTAMAT.2014.01.018.

Wang, Di, Yongqiang Yang, Ziheng Yi, and Xubin Su. 2013. “Research on the Fabricating Quality Optimization of the Overhanging Surface in SLM Process.” *The International Journal of Advanced Manufacturing Technology* 65 (9): 1471–84. https://doi.org/10.1007/s00170-012-4271-4.

Wang, Han, Kexin Su, Leizheng Su, Panpan Liang, Ping Ji, and Chao Wang. 2018. “The Effect of 3D-Printed Ti6Al4V Scaffolds with Various Macropore Structures on Osteointegration and Osteogenesis: A Biomechanical Evaluation.” *Journal of the Mechanical Behavior of Biomedical Materials* 88 (December): 488–96. https://doi.org/10.1016/J.JMBBM.2018.08.049.

Wang, Mengke, Yuwei Wu, Songhe Lu, Tong Chen, Yijiao Zhao, Hu Chen, and Zhihui Tang. 2016a. “Fabrication and Characterization of Selective Laser Melting Printed Ti–6Al–4V Alloys Subjected to Heat Treatment for Customized Implants Design.” *Progress in Natural Science: Materials International* 26 (6): 671–77. https://doi.org/10.1016/J.PNSC.2016.12.006.

———. 2016b. “Fabrication and Characterization of Selective Laser Melting Printed Ti–6Al–4V Alloys Subjected to Heat Treatment for Customized Implants Design.” *Progress in Natural Science: Materials International* 26 (6): 671–77. https://doi.org/10.1016/J.PNSC.2016.12.006.

Wang, Xiaojian, Shanqing Xu, Shiwei Zhou, Wei Xu, Martin Leary, Peter Choong, M. Qian, Milan Brandt, and Yi Min Xie. 2016. “Topological Design and Additive Manufacturing of Porous Metals for Bone Scaffolds and Orthopaedic Implants: A Review.” *Biomaterials* 83 (March): 127–41. https://doi.org/10.1016/J.BIOMATERIALS.2016.01.012.

Wegst, Ulrike G K, Hao Bai, Eduardo Saiz, Antoni P Tomsia, and Robert O Ritchie. 2015. “Bioinspired Structural Materials.” *Nature Materials* 14 (1): 23–36.

https://doi.org/10.1038/nmat4089.

Williams, David F. 2008. “On the Mechanisms of Biocompatibility.” *Biomaterials* 29 (20): 2941–53. https://doi.org/10.1016/J.BIOMATERIALS.2008.04.023.

Williams, J C, B S Hickman, and H L Marcus. 1971. “The Effect of Omega Phase on the Mechanical Properties of Titanium Alloys.” *Metallurgical Transactions* 2 (7): 1913–19. https://doi.org/10.1007/BF02913423.

Wilson, J. 2018. “Metallic Biomaterials: State of the Art and New Challenges.” *Fundamental Biomaterials: Metals*, January, 1–33. https://doi.org/10.1016/B978-0-08-102205-4.00001-5.

Wu, Ming Wei, Jhewn Kuang Chen, Bo Huan Lin, Po Hsing Chiang, and Mo Kai Tsai. 2020. “Compressive Fatigue Properties of Additive-Manufactured Ti-6Al-4V Cellular Material with Different Porosities.” *Materials Science and Engineering: A* 790 (July): 139695. https://doi.org/10.1016/J.MSEA.2020.139695.

Wu, Ming-Wei, Jhewn-Kuang Chen, Bo-Huan Lin, and Po-Hsing Chiang. 2017. “Improved Fatigue Endurance Ratio of Additive Manufactured Ti-6Al-4V Lattice by Hot Isostatic Pressing.” *Materials & Design* 134: 163–70. https://doi.org/https://doi.org/10.1016/j.matdes.2017.08.048.

Wu, Shuilin, Xiangmei Liu, Kelvin W.K. Yeung, Changsheng Liu, and Xianjin Yang. 2014. “Biomimetic Porous Scaffolds for Bone Tissue Engineering.” *Materials Science and Engineering: R: Reports* 80 (1): 1–36. https://doi.org/10.1016/J.MSER.2014.04.001.

Xiao, Lijun, Weidong Song, Cheng Wang, Huiping Tang, Qunbo Fan, Nan Liu, and Jianzhong Wang. 2017. “Mechanical Properties of Open-Cell Rhombic Dodecahedron Titanium Alloy Lattice Structure Manufactured Using Electron Beam Melting under Dynamic Loading.” *International Journal of Impact Engineering* 100 (February): 75–89. https://doi.org/10.1016/J.IJIMPENG.2016.10.006.

Xie, Kelvin Y., Yanbo Wang, Yonghao Zhao, Li Chang, Guocheng Wang, Zibin Chen, Yang Cao, et al. 2013. “Nanocrystalline β-Ti Alloy with High Hardness, Low Young’s Modulus and Excellent in Vitro Biocompatibility for Biomedical Applications.” *Materials Science and Engineering: C* 33 (6): 3530–36. https://doi.org/10.1016/J.MSEC.2013.04.044.

Xu, T. W., S. S. Zhang, F. S. Zhang, H. C. Kou, and J. S. Li. 2016. “Effect of ω-Assisted Precipitation on B→α Transformation and Tensile Properties of Ti–15Mo–2.7Nb–3Al–0.2Si Alloy.” *Materials Science and Engineering: A* 654 (January): 249–55. https://doi.org/10.1016/J.MSEA.2015.12.052.

Xu, Tiewei, Shanshan Zhang, Sen Liang, Ning Cui, Lei Cao, and Yong Wan. 2019. "Precipitation Behaviour during the β → α/ω Phase Transformation and Its Effect on the Mechanical Performance of a Ti-15Mo-2.7Nb-3Al-0.2Si Alloy." *Scientific Reports* 9 (1): 17628. https://doi.org/10.1038/s41598-019-54114-0.

Xue, Pengfei, Yan Li, Kangming Li, Deyuan Zhang, and Chungen Zhou. 2015. "Superelasticity, Corrosion Resistance and Biocompatibility of the Ti–19Zr–10Nb–1Fe Alloy." *Materials Science and Engineering: C* 50 (May): 179–86. https://doi.org/10.1016/J.MSEC.2015.02.004.

Yadroitsava, I., A. du Plessis, and I. Yadroitsev. 2019. "Bone Regeneration on Implants of Titanium Alloys Produced by Laser Powder Bed Fusion: A Review." *Titanium for Consumer Applications: Real-World Use of Titanium*, January, 197–233. https://doi.org/10.1016/B978-0-12-815820-3.00016-2.

Yadroitsev, Igor. 2009. *Selective Laser Melting : Direct Manufacturing of 3D-Objects by Selective Laser Melting of Metal Powders*. Saarbrücken: LAP Lambert Academic Publ.

Yadroitsev, Igor, Ina Yadroitsava, and Anton du Plessis. 2021. "Basics of Laser Powder Bed Fusion." *Fundamentals of Laser Powder Bed Fusion of Metals*, January, 15–38. https://doi.org/10.1016/B978-0-12-824090-8.00024-X.

Yan, Chunze, Liang Hao, Ahmed Hussein, Philippe Young, and David Raymont. 2014. "Advanced Lightweight 316L Stainless Steel Cellular Lattice Structures Fabricated via Selective Laser Melting." *Materials & Design* 55 (March): 533–41. https://doi.org/10.1016/J.MATDES.2013.10.027.

Yan, Lamei, Youwei Yuan, Linjun Ouyang, Hong Li, Alireza Mirzasadeghi, and Li Li. 2016a. "Improved Mechanical Properties of the New Ti-15Ta-XZr Alloys Fabricated by Selective Laser Melting for Biomedical Application." *Journal of Alloys and Compounds* 688: 156–62. https://doi.org/https://doi.org/10.1016/j.jallcom.2016.07.002.

———. 2016b. "Improved Mechanical Properties of the New Ti-15Ta-XZr Alloys Fabricated by Selective Laser Melting for Biomedical Application." *Journal of Alloys and Compounds* 688 (December): 156–62. https://doi.org/https://doi.org/10.1016/j.jallcom.2016.07.002.

Yánez, Alejandro, María Paula Fiorucci, Alberto Cuadrado, Oscar Martel, and Donato Monopoli. 2020. "Surface Roughness Effects on the Fatigue Behaviour of Gyroid Cellular Structures Obtained by Additive Manufacturing." *International Journal of Fatigue* 138 (September): 105702. https://doi.org/10.1016/J.IJFATIGUE.2020.105702.

Zareidoost, Amir, and Mardali Yousefpour. 2020. "A Study on the Mechanical

Properties and Corrosion Behavior of the New As-Cast TZNT Alloys for Biomedical Applications." *Materials Science and Engineering: C* 110 (May): 110725. https://doi.org/10.1016/J.MSEC.2020.110725.

Zhang, D C, Y F Mao, M Yan, J J Li, E L Su, Y L Li, S W Tan, and J G Lin. 2013. "Superelastic Behavior of a β-Type Titanium Alloy." *Journal of the Mechanical Behavior of Biomedical Materials* 20: 29–35. https://doi.org/https://doi.org/10.1016/j.jmbbm.2013.01.015.

Zhang, L C, D Klemm, J Eckert, Y L Hao, and T B Sercombe. 2011. "Manufacture by Selective Laser Melting and Mechanical Behavior of a Biomedical Ti–24Nb–4Zr–8Sn Alloy." *Scripta Materialia* 65 (1): 21–24. https://doi.org/https://doi.org/10.1016/j.scriptamat.2011.03.024.

Zhang, Lai-Chang, and Liang-Yu Chen. 2019. "A Review on Biomedical Titanium Alloys: Recent Progress and Prospect." *Advanced Engineering Materials* 21 (4): 1801215. https://doi.org/https://doi.org/10.1002/adem.201801215.

Zhang, Qiang, Jing Chen, Lilin Wang, Hua Tan, Xin Lin, and Weidong Huang. 2016. "Solidification Microstructure of Laser Additive Manufactured Ti6Al2Zr2Sn3Mo1.5Cr2Nb Titanium Alloy." *Journal of Materials Science & Technology* 32 (4): 381–86. https://doi.org/10.1016/J.JMST.2015.11.019.

Zhang, Xiang-Yu, Gang Fang, and Jie Zhou. 2017. "Additively Manufactured Scaffolds for Bone Tissue Engineering and the Prediction of Their Mechanical Behavior: A Review." *Materials* 10 (1). https://doi.org/10.3390/ma10010050.

Zhao, Danlei, Yutian Huang, Yong Ao, Changjun Han, Qian Wang, Yan Li, Jie Liu, Qingsong Wei, and Zhen Zhang. 2018. "Effect of Pore Geometry on the Fatigue Properties and Cell Affinity of Porous Titanium Scaffolds Fabricated by Selective Laser Melting." *Journal of the Mechanical Behavior of Biomedical Materials* 88 (December): 478–87. https://doi.org/10.1016/J.JMBBM.2018.08.048.

Zhao, S., S. J. Li, S. G. Wang, W. T. Hou, Y. Li, L. C. Zhang, Y. L. Hao, R. Yang, R. D.K. Misra, and L. E. Murr. 2018. "Compressive and Fatigue Behavior of Functionally Graded Ti-6Al-4V Meshes Fabricated by Electron Beam Melting." *Acta Materialia* 150 (May): 1–15. https://doi.org/10.1016/J.ACTAMAT.2018.02.060.

Zhá\vnal, P, P Beran, T Hansen, J Šmilauerová, J Stráský, M Janeček, and P Harcuba. 2018. "Thermal Expansion Evolution of Metastable $\upbeta$ Ti-15Mo Alloy during Linear Heating." *{IOP} Conference Series: Materials Science and Engineering* 461 (December): 12094. https://doi.org/10.1088/1757-899x/461/1/012094.

Zhu, Zuowei, Nabil Anwer, and Luc Mathieu. 2017. “Deviation Modeling and Shape Transformation in Design for Additive Manufacturing.” *Procedia CIRP* 60 (January): 211–16. https://doi.org/10.1016/J.PROCIR.2017.01.023.

Chapter Ⅱ
Material and Methods

2.1 Powder

A prealloyed β-Ti21S alloy powder (GKN Hoeganaes Corporation, Cinnaminson, NJ, USA, D10 = 25 µm, D50 = 41 µm, D90 = 60 µm) produced by plasma-atomization was used. The chemical composition (wt.%) is listed in Table 2-1.

Table 2-1. The chemical composition of β-Ti21S (wt.%) powder.

Element	Mo	Al	Nb	Si	O	Ni	Ti
Weight %	14.6	2.8	2.8	0.3	0.11	0.004	Bal.

2.2 Specimen design

Cylindrical samples (D=4 mm, H=10 mm) were produced by L-PBF for the optimization of the processing parameters, the microstructure and phase constitution analysis, and the and density measurement. Samples were built with the main axis parallel to the building direction. Dogbone cylindrical specimens, with geometry compliant with the ASTM E8M standard, were used for the tensile tests (Figure 2-1a). Cylindrical specimens, with geometry compliant with the ASTM E606 standard, were used for fatigue testing (Figure 2-1b). In order to evaluate any possible anisotropy in the mechanical properties, three cubic samples of 8 mm side were extracted from the terminal part of the tensile test specimens and tested under compression along the three directions x, y, and z, where the building direction was in the z direction. Particular care was taken to cut the sample faces in order to properly align the sample with the loading direction.

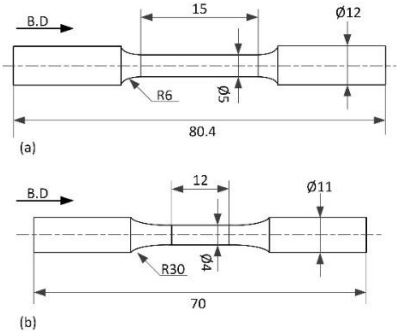

Figure 2-1 : The geometry of the bulk L-PBF samples used for tensile (a) and fatigue (b) tests (dimension in mm).

The primary goal of the present study after investigation of the bulk material is to determine whether the β-Ti21S alloy can be employed to fabricate cellular lattice structures. A first experimental campaign was therefore carried out to evaluate its manufacturability. For this purpose, metrological and metallurgical investigations were carried out on small specimens consisting of a 3x3x3 arrangement of regular cubic cells, as shown in Figure 2-2 (c), these samples are referred herein to the Representative Volume Elements (RVEs) samples. All the structures were designed with fillets at the nodes and circular struts to minimize sharp corners and associated stress concentrations, which were proved to be detrimental for the fatigue strength of cellular lattice materials (Dallago et al. 2021). The corresponding strut thickness and fillet radius were adjusted through a homogenization technique implemented in nTopology software to achieve a theoretical elastic modulus along the cube side direction of about 1 GPa. The sections of the struts are circular with constant diameter, and all nodes are filleted. The geometrical parameters that characterize each cell are the strut length *L*, the strut thickness *t* (diameter), and the fillet radius *R*. The geometric features of the three different unit cell sizes are listed in Table 2-2. Due to its simplicity, the cubic unit cell was considered the best candidate to explore the 3D-printability of lattice structures using β-Ti21S alloy. The mechanical testing sample was designed in rectangular shape (Figure 2-2 d).

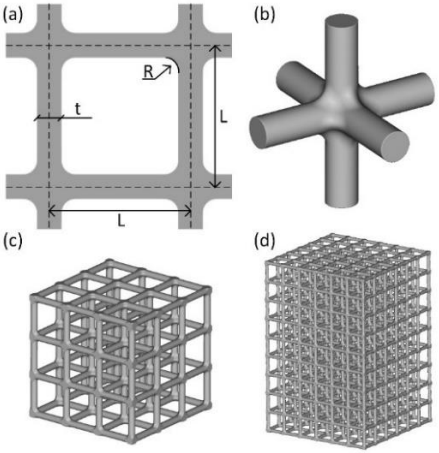

Figure 2-2 : The geometry of the cubic lattice samples, (a) Unit cell configuration parameter definition of in-plane geometry (R = fillet radius, t = strut thickness, and L = cell size or strut length), (b) 3D view of junction with concave fillet, (c) assembled design for manufacturability study, and (d) assembled design for mechanical testing.

Table 2-2. Investigated lattice designs for Representative Volume Elements (RVEs) .

Designation XPY-t*	Unit cell size L (mm)	Strut thickness t (mm)	Fillet radius R (mm)	Ratio (t/L)	Porosity (%)
LPS 0.26	1.5	0.26	0.13	0.17	93
NPS 0.26	1.5	0.26	0.13	0.17	93
NPM 0.68	4	0.68	0.4	0.17	93
NPL 1.06	6	1.06	0.3	0.17	93

***XP = Low or Normal laser Power, Y = Size of sample (Small, Medium, and Large), t = strut thickness in mm**

In the second step of lattice structure investigation, a more intricate geometry, octet truss, was designed and investigated. The reason for this choice is manifold: the octet truss topology was found to be more effective for the mechanical properties, showing higher fatigue resistance (Benedetti et al. 2021). This structure has two size of large and small pores size suitable from the biomedical point of view. The sample was designed with a strut thickness of t=0.54 mm, fillet radius of r=0.6 mm and the cell size of L=4 mm (Figure 2-3a). The mechanical test sample was designed with repeating the cell size 6 times in each direction to create the rectangular geometry (Figure 2-3b).

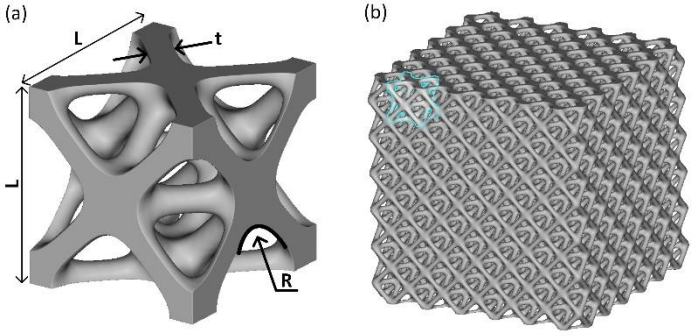

Figure 2-3 : The geometry of the octet truss lattice samples, (a) Unit cell configuration parameter definition of in-plane geometry (R = fillet radius, t = strut thickness, and L = cell size or strut length) and (b) assembled design for mechanical testing.

2.3 L-PBF parameters

The bulk samples were fabricated with the main axis parallel to the building direction using an L-PBF machine model MYSINT100 (SISMA SPA, Piovene Rocchette, Italy) with a laser spot of 55 µm. The machine has an in-house developed building platform of 100 mm diameter and a 200 W fiber laser. Process parameters

were optimized to achieve maximum density. The laser heat input was kept between 40 J/mm^3 and 90 J/mm^3. An XY alternate scan strategy was applied. In order to prevent oxygen pick-up, an argon atmosphere was used, reaching a 100 ppm O_2 content inside the chamber. The process layer thickness was set to 20 µm

The cubic lattices samples were fabricated diagonally with support attached to one corner of the sample to ensure an acceptable geometric accuracy to the all the cell struts, as this was found to produce the best quality (Simone Murchio et al., n.d.; S. Murchio et al. 2021). The octet truss samples were fabricated along the length of cube with support attached to the bottom side of part. The same machine with a laser spot of 55 µm was used. The contouring scan strategy was applied as shown in the Table 2-3. An XY alternate scan strategy was adopted for the hatching strategy. The powder layer thickness was set to 20 µm. To investigate the effect of laser heat input on microstructure and manufacturability, two different laser power were employed in the fabrication of the samples with the smallest cell size, namely low (LP) and normal power (NP). A contouring strategy was adopted for all specimens. The samples were manually detached from the building platform and the excess powder particles were ultrasonically removed by ethanol 96%.

Table 2-3. Scan strategy investigated for lattice designs.

Designation XPY-t*	Laser heat input (J/mm3)	Scan strategy
LPS 0.26	45-75	Contouring
NPS 0.26	60-90	Contouring
NPM 0.68	60-90	Hatching and outer contouring
NPL 1.06	60-90	Hatching and outer contouring
Octet 0.54	60-90	Hatching and outer contouring

***XP = Low or Normal laser Power, Y = Size of sample (Small, Medium, and Large), t = strut thickness in mm.**

2.4 X-ray diffraction

The phase constitution was determined by X-ray diffraction (XRD) using a Co radiation (λ = 0.17889 nm) source and the analysis were made from the polished samples. Texture and crystallographic orientation for taking out pole figure were evaluated by X-ray with (1) microfocus 50 W Cu source, 2D beam optic; (2) detctris eiger 1M 2S hybrid pixel detector; and (3) four circle huber goniometer. Both X-ray measurements were carried out on metallographic cross sections parallel and perpendicular to the building directions.

2.5 Density measurement

Density was measured by Archimedes' principle according to ASTM B962-08 on 10 mm diameter samples. The relative density was calculated normalizing the measured density by the theoretical density of the β-Ti21 4.94 g/cm^3 (Welsch, Boyer, and Collings 1993). For cellular structures, the relative density was calculated according to ASTM B962, as well as from Micro-CT data using the nTopology platform considering the entire volume surfaces using the mass properties block. nTopology (n n.d.) is a software package dedicated to the design and simulation of lattice structures, but dimensional measurements are also possible.

2.6 Microstructure

To study the microstructure of the lattice structures, the specimens were sectioned, mounted in cold resin, ground with emery papers followed by polishing with 0.04 µm silica suspension, and etched using Kroll's solution to reveal the microstructure. The microstructural characterization was carried out by optical microscopy (model Axiophot, Carl Zeiss EL-Einsatz, Jena, Germany) as well as by scanning electron microscopy (SEM, model JSM-IT300LV, Jeol, Tokyo, Japan).

2.7 Micro-hardness

The HV0.1 hardness was measured with a micro hardness tester (model FM-310, Future Tech, Kawasaki, Japan), according to ASTM E92, taking five measurements for each sample and reporting the average value from the top and lateral surfaces.

2.8 CT scan

X-ray Micro-CT was used for analysis of whole lattice samples, scanned at the best possible voxel size for each sample (Anton du Plessis et al. 2018). A Nanotom S system was used, with X-ray voltage between 110 and 130 kV and current 80 to 90 µA. The smallest samples (LPS and NPS) were scanned with 5 µm voxel size, while the larger samples with 12 µm and 16 µm. Additional scan of each sample type was performed for sectioned samples with 2 µm voxel size. Image analysis was performed using Volume Graphics VGStudio Max 3.4.5. After denoising the images with adaptive Gauss filter, an advanced surface determination function was used to create a sub-voxel segmentation of the material-air interface. This was used to create a 3D mesh representation of the real sample geometry. The obtained STL file data gathered from the analysis was taken as the input for the further geometrical analysis.

2.9 Metrological analyses

The morphological analysis of the lattice cubic design was performed by measuring the local strut and junction sizes, according to the sphere method

described in (A du Plessis et al. 2018). This method was conducted for designing STL file and Micro-CT data STL file in VGStudio Max (wall thickness analysis function). The sphere method fits the largest sphere at each location within the structure and reports those sphere diameters as the distribution histogram of local thickness. The junction and strut thickness were detected by bimodal distribution fitting method and the surface imperfections were estimated by normal distribution fitting method. To compare with the 3D method, the 2D investigation (in-plane) from SEM micrographs were also made, whereby the strut and junction thickness were measured by fitting the circular shape to them and reporting the average diameters.

The dimensional analysis was made by overlapping the CAD design on the printed one. The strut waviness factor and eccentricity (tending to have a circular shape in plane) were measured by a MATLAB (MathWorks, USA) code. For this, the STL file gathered from Micro-CT scan data were imported into MATLAB and the center of each node was calculated as the centroid of the junction, after that each strut was sampled in 40 slices. The points of each slice were fitted via a least square ellipse shape (Figure 2-4). Overall, 54 struts (18 vertical and 36 horizontal) were sliced. The strut waviness factor was estimated from the distance of junction center from the fitted elliptical cross-section on the plane (Figure 2-4); the values were then normalized to the nominal length of strut to be comparable to each cell size. The eccentricity was also quantified according to the following equation:

$$e = \frac{\sqrt{a^2 - b^2}}{a} \tag{16}$$

where a and b are the longer and shorter diagonals of ellipse, respectively.

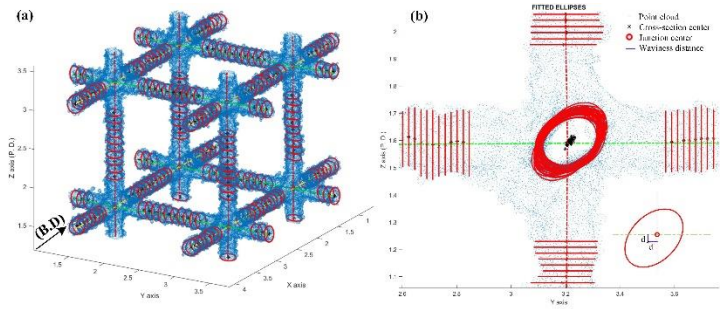

Figure 2-4 : The strut waviness and eccentricity measurement in the MATLAB platform. (a) example of slicing and fitting the ellipse to the STL file gathered from the Micro-CT data, (b) the fitted ellipse parameters to the sliced sample.

2.10 FE simulations

To investigate the effect of geometrical imperfections introduced by the manufacturing techniques on the local stress field generating on struts and nodes, Linear Finite Element (FE) analyses were carried out. For this purpose, the geometry of the entire lattice samples acquired via CT scans (RVEs) was imported into the nTopology platform. The RVEs were repeated in space to reply to the real cell structure, and a tetrahedral volume mesh was generated. To capture the surface irregularities and to speed up the simulation process, the mesh transition technique was conducted so that the mesh volume size was minimum on the surface (equal and less than the size of Micro-CT scan voxel size) and gradually increased toward the center of the body. This procedure was performed by means of ramp function block during the mesh generation process. Linear elastic properties inferred from the monotonic tensile tests were enforced into the FE models. The application of the compressive load was simulated through a displacement-based analysis. For this purpose, the deformation of the bottom surface was constrained in all directions and normal compressive displacements were applied to the top surface (Figure 2-5a). Displacement values were obtained from the experiments. The stress was calculated by dividing the reaction by the applied displacement and the nominal area of the FE model.

The displacement field determined by the above simulations for the entire cellular lattice was used to set the boundary conditions of a refined submodel of a single node of the structure. For this purpose, the higher accuracy from a finer mesh was used (edge length 0.05 mm). Nodal displacements interpolated from those estimated from the general model were applied to the cutting planes of the submodel. The resulting stress field was compared with that estimated in a similar way but considering the ideal CAD geometry of the cellular lattice specimens.

A convergence test was performed by changing the function parameter of the ramp block to obtain a different transition degree of the volume mesh from surface to the center. In this way, the minimum mesh size was set fix at the surface and the transition varied towards the center of the body. The error was calculated on the maximum principal stress for each level. The convergence analysis was stopped when the relative error was equal or below 1%.

The stress concentration factor (K^*_t) was calculated according to the following definition (Dallago et al. 2019):

$$K_t^* = \frac{maximum\ von\ Mises\ equivalent\ stress\ in\ the\ structure}{nominal\ homogenous\ stress} \quad \textbf{(17)}$$

Where the nominal homogenous stress (MPa) is the ratio between the load on the junction and the nominal area of junction. The K^*_t values at every point were taken

in the space and the average values were made in a z-plane for one point. The data points were plotted with its geometrical junction counterpart in the 2D plane.

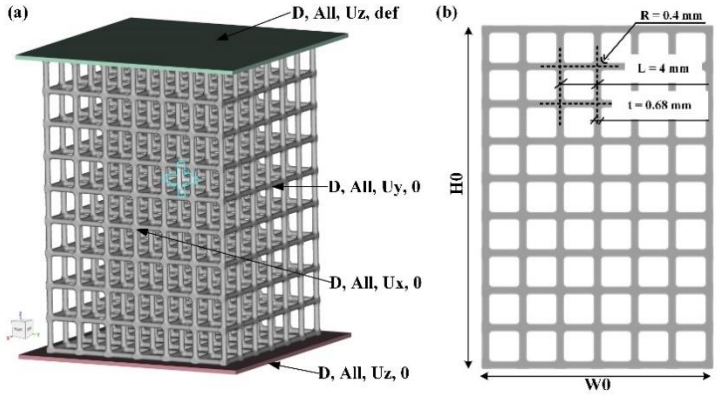

Figure 2-5 : (a) sketch of the FE model showing the boundary condition and single junction as sub-model. The boundary condition was translated to the sub-model, (b) geometry of the specimens used for the mechanical tests (compression and fatigue).

2.11 Mechanical testing

Tensile tests for the bulk samples were carried out according to ASTM E8M at a strain rate of 1 mm/min on dogbone cylindrical specimens with 15 mm gage length and 5 mm diameter using a universal servohydraulic testing machine (model 8516, Instron, Norwood, MA, USA). Strains were measured using an axial extensometer with a 12.5 mm gauge length. Yield stress, Young's modulus, and fracture strain were determined according to ASTM E 111; the average values and standard deviations were calculated considering at least three samples. Samples were tested parallel to the building direction and did not undergo any finishing step after L-PBF.

In order to explore possible anisotropy of the bulk sample in the material mechanical response, three cubic samples of 8 mm side were extracted from the terminal part of the tensile specimens and tested under compression along the three directions x, y, and z. Particular care was taken to cut the sample faces in order to properly align the sample with the loading direction. Compressions tests were carried out under stroke control with a strain rate of 1 mm/min. Tests were stopped at 12% strain owing to the achievement of the load capacity of the testing machine. The compression axial strain was measured using an Instron LVDT, and the same machine used for the tensile tests.

High cycle compression–compression fatigue testing was carried out on 10 bulk specimens; staircase fatigue test strategy was performed for load values selection. A

RUMUL resonating fatigue test machine was used with an R-ratio of -1 in compression. The data were fitted according to the following equation:

$$\sigma_a = C_1 + \frac{C_2}{N_f^m} \quad \textbf{(18)}$$

Where σ_a is the homogenous axial stress amplitude, N_f is the number of cycles to failure, C_1, C_2, and m are a fitting constant. The scattering of the fatigue data (S^2) was estimated by equation **(19)**.

$$S^2 = \frac{\sum_{i=1}^{n}(\sigma_{a,i} - \sigma'_{a,i})^2}{n-p} \quad \textbf{(19)}$$

Where $\sigma_{a,i}$ is the stress amplitude after *i* cycles, $\sigma'_{a,i}$ is its estimator, *n* is the number of data elements, and *p* is the number of parameters in the regression (p = 3).

Static compression and fatigue compression-compression tests performed on the lattice designs (Figure 2-2d and Figure 2-3b). More specifically, quasi-static monotonic compression tests were performed on the samples using a universal servohydraulic testing machine (model 8516, Instron) equipped with compression plates. The tests were conducted according to ISO 13314:2011 at room temperature imposing a constant deformation speed of 0.5 mm/min. A linear variable displacement transducer (LVDT) was used to measure the displacement up to 15 percent of elongation. The stress–strain curve obtained from the monotonic testing condition was then used to calculate the monotonic Young's modulus, E_m, 0.2% offset yield strength, σ_y, and the maximum compressive strength, σ_{mc}. Cyclic tests were performed to obtain the cyclic Young's modulus, E_c, after stabilization of the stress–strain response. The specimens were loaded between 20% and 70% of the yield load obtained from the monotonic testing condition using a triangular shape wave for five cycles.

High cycle compression–compression fatigue testing was carried out on 10 lattice specimens. A RUMUL resonating fatigue test machine was used with an R-ratio of 0.1 in compression. The data were fitted, and the scattering of the fatigue data was estimated according to the equations (18) and (19), respectively. Five fatigue lattice samples were sectioned for identification of crack locations after testing.

2.12 In Vitro testing

In vitro cytotoxicity was determined according to EN ISO 10993-5: 2009 for the β-Ti21S (test) and Ti–6Al–4V ELI (reference) samples (ISO 10993 2009). MG63 human osteosarcoma cell line (Cell bank IRCCS San Martino IST, Genova, Italy) was used. Cells were thawed and expanded in a 75 mL flask using Dulbecco's modified Eagle's medium (DMEM, Merck KGaA, Darmstadt, Germany) with 10% foetal bovine

serum (Euroclone S.p.A, Pero, Italy) and 100 IU/mL penicillin–100 µg/mL streptomycin (Gibco, Merck KGaA, Darmstadt, Germany) in standard culture conditions (37 °C in 5% CO_2 humidified atmosphere). Cells were seeded at the concentration of 2×10^4 cells/cm^2 in multiwell plates with test and reference materials and appropriate negative (CTR−: negative ConTRol, cells without materials) and positive (CTR+: positive ConTRol, cells in presence of a known cytotoxic agent, 0.5% phenol solution in DMEM) controls were run concomitantly.

Plates were incubated for 24 h, at 37 °C in 5% CO_2 atmosphere. Thereafter, cell viability assay, Neutral red, and Phallodin stainings were performed and supernatants collected for the measurement of lactate dehydrogenase (LDH) release.

Cell viability was evaluated by adding Alamar Blue Cell Viability Reagent (Thermo Fisher Scientific, Waltham, MA, USA) to the fresh medium; viable cells internalize and reduct non-fluorescent Resazurin to fluorescent Resorufin. After 3.5 h of incubation, fluorescence was red at 530ex–590em nm wavelengths by a micro plate reader (VICTOR X2030, Perkin Elmer, Italy) and expressed as a percentage of negative controls. Samples with cell viability below 70% were considered cytotoxic, as indicated in the ISO 10993 standard.

LDH release was measured by an enzyme-kinetic cytotoxicity detection kit (Roche Diagnostics Spa, Monza, Italy). Briefly, 100 µL of reagent was added to 100 µL of cell supernatant in a 96-well plate; after 30 min of incubation at room temperature in the dark, optical density (OD) were quantified by spectrophotometer at 490/655 nm. Cytotoxicity was calculated as follows:

$$Cytotoxicity(\%) = \frac{OD\ test - OD\ CTR-}{OD\ CTR + -OD\ CTR-} \times 100 \quad \textbf{(20)}$$

Neutral Red staining and quantification were performed by the in vitro toxicology assay kit (Merck KGaA, Darmstadt, Germany). Briefly, a 0.033% solution of the reagent in culture medium was added to all wells at the end of the experimental time for a further 90 min. Cultures were examined by light microscopy for the evaluation of cell morphology and images were taken (inverted microscope equipped with a Nikon digital camera model Eclipse, Melville, NY, USA). Then, the dye was solubilized by adding 1% acetic acid in 50% ethanol under gentle stirring in a shaker for 10 min. Absorbance was measured at a wavelength of 540 nm. Neutral red uptake was expressed as the percentage of negative controls.

Phalloidin staining was performed after cell fixation in a solution of 4% paraformaldehyde in phosphate buffered solution (PBS) for 15 min at 37 °C, permeabilization in 0.5% Triton X-100 for 15 min, and extensive washing steps in PBS. An Fluorescein Isothiocyanate -conjugate phalloidin solution (Merck KGaA, Darmstadt, Germany) 1:100 in PBS was added for 30 min at 37 °C and, after washing

in PBS, samples were observed by fluorescence microscope (Nikon Eclipse, Nikon, Moncalieri, Italy).

Statistical evaluation of biomedical data was performed using the software v.23 package SPSS/PC + StatisticsTM 25.0 (SPSS Inc., Chicago, IL, USA). Data are reported as mean ± standard deviations (SD) at a significance level of $p < 0.05$ of three replicates. Data did not show a normal distribution and homogeneity of variance (Levene test), and thus a non-parametric analysis was carried out using Kruskal–Wallis followed by the Mann–Whitney U test to compare materials and controls.

2.13 References

Benedetti, M., A. du Plessis, R. O. Ritchie, M. Dallago, S. M.J. Razavi, and F. Berto. 2021. "Architected Cellular Materials: A Review on Their Mechanical Properties towards Fatigue-Tolerant Design and Fabrication." *Materials Science and Engineering: R: Reports* 144 (April): 100606. https://doi.org/10.1016/J.MSER.2021.100606.

Dallago, M., S. Raghavendra, V. Luchin, G. Zappini, D. Pasini, and M. Benedetti. 2021. "The Role of Node Fillet, Unit-Cell Size and Strut Orientation on the Fatigue Strength of Ti-6Al-4V Lattice Materials Additively Manufactured via Laser Powder Bed Fusion." *International Journal of Fatigue* 142 (January): 105946. https://doi.org/10.1016/j.ijfatigue.2020.105946.

Dallago, M., B. Winiarski, F. Zanini, S. Carmignato, and M. Benedetti. 2019. "On the Effect of Geometrical Imperfections and Defects on the Fatigue Strength of Cellular Lattice Structures Additively Manufactured via Selective Laser Melting." *International Journal of Fatigue* 124 (July): 348–60. https://doi.org/10.1016/J.IJFATIGUE.2019.03.019.

ISO 10993. 2009. "Biological Evaluation of Medical Devices — Part 5: Tests for in Vitro Cytotoxicity." *International Organization for Standardization, Geneva*. https://www.iso.org/standard/36406.html.

Murchio, S., M. Dallago, F. Zanini, S. Carmignato, G. Zappini, F. Berto, D. Maniglio, and M. Benedetti. 2021. "Additively Manufactured Ti–6Al–4V Thin Struts via Laser Powder Bed Fusion: Effect of Building Orientation on Geometrical Accuracy and Mechanical Properties." *Journal of the Mechanical Behavior of Biomedical Materials* 119 (July): 104495. https://doi.org/10.1016/J.JMBBM.2021.104495.

Murchio, Simone, Michele Dallago, Andrea Rigatti, Valerio Luchin, Filippo. Berto, Devid Maniglio, and Matteo Benedetti. n.d. "On the Effect of the Node and Building Orientation on the Fatigue Behavior of L-PBF Ti6Al4V Lattice Structure Sub-Unital Elements." *Material Design \& Processing*

Communications n/a (n/a): e258. https://doi.org/https://doi.org/10.1002/mdp2.258.

n, T. n.d. “NToplogy.” https://ntopology.com/. Accessed January 6, 2022. https://ntopology.com/.

Plessis, A du, I Yadroitsava, I Yadroitsev, SG le Roux, and DC Blaine. 2018. “Numerical Comparison of Lattice Unit Cell Designs for Medical Implants by Additive Manufacturing.” *Virtual and Physical Prototyping*, June, 1–16. https://doi.org/10.1080/17452759.2018.1491713.

Plessis, Anton du, Igor Yadroitsev, Ina Yadroitsava, and Stephan G le Roux. 2018. “X-Ray Microcomputed Tomography in Additive Manufacturing: A Review of the Current Technology and Applications.” *3D Printing and Additive Manufacturing* 5 (3): 227–47. https://doi.org/10.1089/3dp.2018.0060.

Welsch, G, R Boyer, and E W Collings. 1993. *Materials Properties Handbook: Titanium Alloys*. Materials Properties Handbook. ASM International. https://books.google.it/books?id=x3rToHWOcD8C.

Chapter Ⅲ

Result and Discussion

Part 1: Laser Powder Bed Fusion of bulk samples

3.1 Introduction

Among metallic biomaterials for biomedical and specifically orthopaedic application, titanium and its alloys exhibit the most suitable characteristics as compared to stainless steels and Co-Cr alloys because of their high biocompatibility, specific strength, and corrosion resistance (Lütjering and Williams 2007). According to their phase constitution, Ti-alloys are classified into three main groups, namely α, β and $\alpha+\beta$ alloys. In essence, the microstructure depends on type and number of alloying elements, since isomorphous α-phase stabilizers (Zr, Al, Sn, O and Si), dissolved preferentially in α phase, expand its phase field, while isomorphous β-phase stabilizers (H, Mo, W and V), dissolved in the β phase, play the same role on the β phase field (Collings 1988). Depending on the degree of alloying and thermomechanical processing path, it is possible to tune the balance of α and βphases, which permits to tailor properties like strength, toughness, and fatigue resistance.

Fully α alloys have important strength limitations due to reactions occurring at high temperatures, during hot forming. Therefore, the development of Ti-alloys has been mainly focused on α+β ones. Until recently, the guidelines followed for the introduction of biomaterials for hard tissue substitution in orthopedic applications have involved adaptation of existing materials, as exemplified by the use of Ti-6Al-4V extra-low interstitial (ELI), an alloy originally designed for aerospace applications. Besides Ti–6Al–4V ELI (ASTM F 136), only Ti–6Al–7Nb (ASTM F 1295) has been standardized for biomaterials in ASTM. However, one of the major limitations of $\alpha+\beta$ alloys is given by their relatively high Young's modulus E, being comprised between 110 and 120 GPa (Lütjering and Williams 2007). The resulting stiffness mismatch between bony tissue (Young's modulus is equal to 10÷20 GPa and 0.1÷1 GPa for cortical and cancellous bone, respectively) and implant causes stress shielding and bone resorption (HUISKES, WEINANS, and RIETBERGEN 1992; Parthasarathy et al. 2010).

In view of the lower elastic modulus of body center cubic bcc-β phase (50GPa<E<100GPa) as compared to the fcc-α one, as well as due to their good mechanical properties, excellent corrosion resistance and biocompatibility, β-Ti alloys have been recently proposed as a valid alternative to $\alpha+\beta$ ones (Khorasani et al. 2015; Niinomi 1998b). For this purpose, several alloying systems were explored in the past to confer adequate mechanical properties. To this regard, Mo-rich grades

like Ti-12Mo-6Zr-2Fe (ASTM F1813) and Ti-15Mo-2.8Nb-0.2Si-0.28O with tensile strength >1000MPa, total elongation >15% and Young's modulus around 80GPa were developed for orthopaedic applications (HUISKES, WEINANS, and RIETBERGEN 1992; Parthasarathy et al. 2010). Among Nb-rich grades, Ti-13Nb-13Zr is worth of mention because of the good property portfolio, even if precipitation hardening alloys as Ti–29Nb–13Ta–4.6Zr and Ti–16Nb–13Ta–4Mo have been proposed in the literature (Y. L. Zhou and Niinomi 2008; Niinomi 2003). Materials used in biomedical applications must exhibit a high cycle fatigue strength. The results reported in the literature evidence a broad spectrum of fatigue strength for biomedical Ti alloys, ranging from 265 to 816 MPa (Niinomi 1998b). This large variety can be mainly ascribed to the wide range of microstructural options (e.g., fully lamellar, bi-modal, pancake (Benedetti et al. 2008)) along with the possibility of hardening the metastable beta-matrix through precipitation of fine particles of α-phase (Collings 1988). In this way, it is possible to achieve fatigue properties even superior to those of α+β alloys (Peters and Lütjering 2001).

From a biological point of view, the compatibility and osseointegration of an implant in the surrounding living tissues can be seriously hindered by the release of metallic ions into the human body, causing sensitization, irritation, and inflammation. From a recent systematic review, metallic wear debris particles are responsible for upregulating the production of several pro-inflammatory cytokines, chemokines and matrix metalloproteases that induce chronic inflammation, tissue fibrosis and osteoclasts activation at the bone-implant interface (Veronesi, Tschon, and Fini 2017). Osteoclasts and osteoclastogenensis determine a progressive bone deterioration and enhance the osteolysis progress that can compromise the implant stability leading to implant loosening (Abu-Amer, Darwech, and Clohisy 2007; Wooley and Schwarz 2004; Sundfeldt et al. 2006).

Another limitation in the use of the golden standard Ti–6Al–4V ELI stems from its content of potentially cytotoxic alloying elements, namely Al and especially V (Kim Vanmeensel et al. 2018). There is hence a considerable interest in developing new Ti-alloy formulations without the addition of cytotoxic elements. In the context of b-Ti, which is the focus of the present paper, it is crucial to avoid the use of V as a b-stabilizing element (Niinomi, Nakai, and Hieda 2012). For instance, Ti-15Mo-5Zr-3Al has been claimed to be a good candidate for biomedical implants, mainly thanks to the relatively low Young's modulus (80 GPa), the good ductility (25%) and formability associated to the bcc structure along with adequate yield strength (830 MPa) (Niinomi 1998b). It is well documented that this alloy can experience long-term exposure in the human body and that the crystal structure of the cast alloys changes from $\alpha' \rightarrow \alpha'' \rightarrow \beta$ increasing the Mo content from 6 to 20 wt% (Ho, Ju, and Chern Lin 1999). Ti-15Mo-2.7Nb-3Al-0.2Si grade can provide the same properties of Ti-6Al-4V for biomedical

as well as for aerospace applications (Xu et al. 2016).

In designing new b Ti-alloy systems, the scenario depicted so far is further complicated by the growing interest towards fabricating biomedical prosthetic implants through additive manufacturing (AM) techniques (Ni et al. 2019). AM will prospectively allow tailoring a specific implant to the patient and producing it on demand, with large savings on times and costs (Gross et al. 2014). AM is gaining increasing interest due to the possibility of producing orthopedic implants with functionally graded open-cell porous metals(Ryan, Pandit, and Apatsidis 2006). Their purpose is to mimic the complex structure of the bone with the aim to increase the implant osseointegration (Tan et al. 2017). The main advantages of porous materials are the reduction of the elastic modulus mismatch between bone and implant alloy alleviating the stress shielding effect and improved implant morphology providing biological anchorage for tissue in-growth (Y. Wang et al. 2018).

Finding formulations of b Ti-alloys suitable to be additively manufactured is therefore of vital importance for the current biomedical research. The attention has been focused so far on the addition of transition/refractory β stabilizing metals. Wang et al (Q. Wang et al. 2017) investigated the effect of Nb content on the β phase stability of an AMed Ti-Nb system. Some other researchers (L. Zhou et al. 2018; Zhuravleva et al. 2013) have compared AM of the Ti-Nb system via other production methods, such as Hot Pressing and Hot Forging. In particular, Zhou et al (L. Zhou et al. 2018) reported that the microstructure, properties and phase formation are greatly influenced by the production method. Fischer and Schwab (Fischer et al. 2016; Holger Schwab et al. 2015) manufactured Ti-26Nb and Ti-45Nb with mixed and pre-alloyed powder to achieve the β phase. Trabecular structure made up of beta Ti-24Nb-4Zr-8Sn and Ti-30Nb-5Ta-3Zr were investigated in (Y. J. Liu et al. 2015; Luo et al. 2019) showing however that the footprint of α precipitation was not erased entirely. Tantalum has been introduced even if it is a rare-earth and expensive metal, 50 wt.% thereof is necessary to fully stabilize the beta phase in high cooling rate solidification (Sing, Yeong, and Wiria 2016). Recently, it was found that Ti-15Ta-xZr might have even better performances (L. Yan et al. 2016). Ti-5Al-5V-5Mo-3Cr alloy was designed to meet aerospace demands (H. Schwab et al. 2016). However, its biocompatibility is doubtful due to the presence of V and the fact that no cytotoxicity test was done. Some authors have attempted to address the drawbacks of the aforementioned elements by introducing Mo as the main alloying element. Vrancken et al (Vrancken et al. 2014) performed considerable research on the AM production of beta-Ti alloys. By introducing 10% wt. Mo to Ti-6Al-4V ELI powder, the β→α´ martensitic transformation was suppressed, and a metastable beta structure could be achieved. Indeed, owing to the limited chemical homogeneity of the liquid inside the melting pool, heat treatment was required to reduce the segregation of this element in the

microstructure. The Young's modulus (73 GPa) was lower than that of α+β alloys, but still much higher than that of the human bone (20 GPa). Nan Kang et. Al. produced Ti-7.5Mo samples by selective laser melting, showing that the Mo content is not high enough to obtain a fully β structure and a significant improvement in mechanical properties (Kang et al. 2019; 2020).

From the above discussion, it is clear that another AM-related advantage of β over α+β Ti-alloys resides in the possibility of suppressing the martensitic transformation in suitably formulated b Ti-alloys. Indeed, the high cooling rates typical of laser powder bed fusion (L-PBF) AM process lead to the formation of brittle and soft *α´* phase in α+β alloys (Vilaro, Colin, and Bartout 2011). In addition, the volumetric expansion associated to the martensitic transformation is responsible for undesired residual stresses and distortions (Ahmed and Rack 1998a). For this reason, α+β Ti-alloys necessitate a heat treatment before removing the part from the L-PBF building platform either above or below the b-transus to obtain a fine acicular or a coarse lamellar microstructure, respectively (Sercombe et al. 2008; Benedetti et al. 2017). This represents however an additional and delicate manufacturing step, which must be carried out carefully to avoid detrimental oxygen pickup (Z. Liu and Welsch 1988). Unfortunately, vacuum furnaces are not always within the reach of any biomedical manufacturer.

With this in mind, the present work is aimed at identifying a Ti-alloy formulation suitable to be manufactured via L-PBF without the necessity of any post-sintering treatment. In particular, it explores the potential use of the Ti-15Mo-2.7Nb-3Al-0.2Si alloy (Beta Ti21S, 21 wt.% of alloying additions, including Silicon) for biomedical applications. Through microstructural, mechanical and cytotoxicity analyses, we will show that this material exhibits (i) an unprecedented ultra-low elastic modulus, prospectively beneficial to the mechanical compatibility with the bone, ii) an improved cytocompatibility due to the lack of Vanadium, and iii) the absence of the martensitic transformation responsible for hard and brittle solidification structures.

3.2 Result and discussion

3.2.1 Microstructure

The prealloyed β-Ti21S alloy powder used in this work displays a spherical particles shape (Figure 3-1 a). The particle size distribution (D_{10}=25, D_{50}=41 and D_{90}=60 µm) evidences two distinct peaks, the first one centered around 10 µm related to satellite particles (Figure 3-1 b), and the second one, around 41 µm, related to the coarser powders fraction.

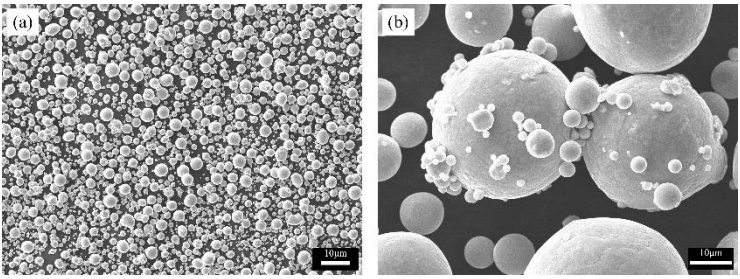

Figure 3-1 : (a) General and (b) high magnification views of β-Ti21S powder (scanning electron microscopy, SEM).

The top and a cross sectional views of the microstructure of a small cylindrical sample (D=4 mm, H=10 mm) highlight the achievement of a near fully dense material showing a columnar structure oriented along the building direction (BD) (Figure 3-2). The melting pools boundaries further outline the alternate laser scan strategy used for the fabrication of samples. The epitaxial growth of β grain takes place along the heat flow direction and, according to previous works, it stems from partial remelting of previously consolidated layers, and extends up to several millimeters in length (Ishimoto et al. 2017). The average width of the β grains is 69±8 µm.

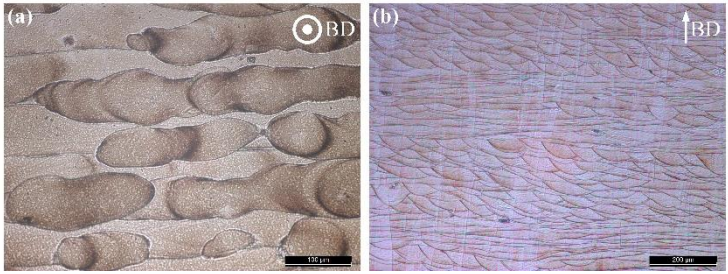

Figure 3-2 : Top (a) and cross section (b) views of as-built β-Ti21S (optical microscope). BD, building direction.

SEM micrographs taken at higher magnification emphasize the traces of melting pools boundaries (Figure 3-3 a and b). Moreover, SEM micrographs taken at higher magnification evidence that the solidification structure is planar at melt pool boundary, turning into cellular 0.5-1µm inside the pool region (Figure 3-3c). The destabilization of the planar solidification front is due the establishment of constitutional undercooling, and in particular to the decreasing temperature gradient inside the liquid (T'_L) ahead of the solid/liquid interface. When T'_L becomes lower than the critical gradient (T'_C) equation (21), the planar to cellular transition may occur (Porter and Easterling 2009).

$$T_c' = \frac{T_{liq} - T_{sol}}{D/v} \quad (21)$$

T_{liq}=liquidus temperature,

T_{sol}=solidus temperature,

D=solute diffusivity in the liquid, and

v=solidification speed

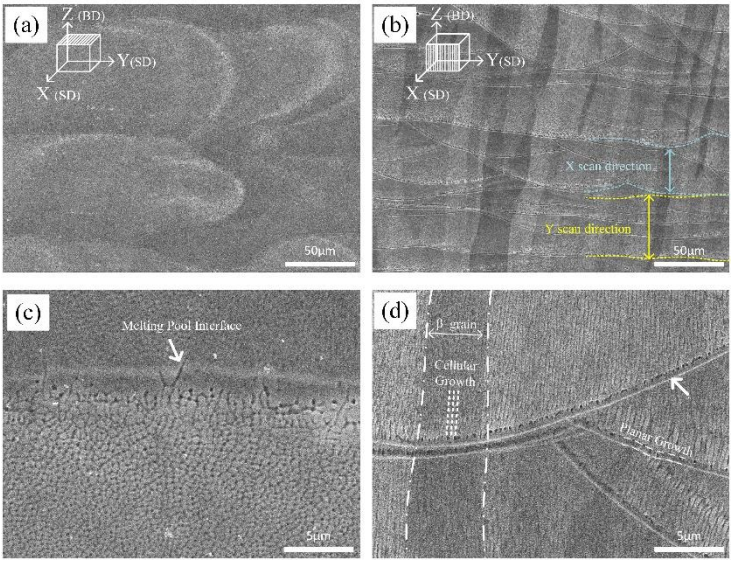

Figure 3-3 : SEM microstructure of Ti21S alloy at (a, b) low and (c, d) high magnification.

In 15%Mo Ti-21S alloy this event is favored by the large solidification range (T_{liq}-T_{sol} ≈ 15 k) as well as by the very high solidification speed *v* during LPBF process. A planar solidification front is observed instead in Ti-6Al-4V, showing a much narrower freezing range (T_{liq}-T_{sol} ≈ 5 k) (Khorasani et al. 2015). Inside each columnar grain, the cellular substructure shows an intercellular spacing of less than 0.6µm (Figure 3-3d). The cells growth direction is near-vertically oriented, i.e., along the temperature gradient, towards the top melt pool center. It closely follows the laser flow direction, i.e., if the laser beam is moved from left to right, the grains are oriented rightwards (Figure 3-2b and Figure 3-3b).

3.2.2 Phase constitution and texture

XRD analysis confirms that as-built alloy is constituted by a single metastable β-phase (Figure 3-4). Traces of neither α nor α'-martensite can be detected. Comparing the powder and as-built spectra, the peaks show a change in relative intensity, which is representative of the crystallographic texture in the as-built alloy. As a confirmation, XRD patterns were obtained from different orientations.

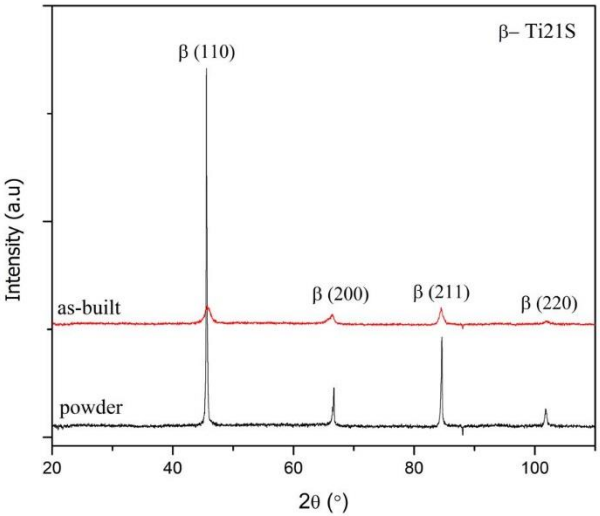

Figure 3-4 : XRD patterns of initial powder and As-built β-Ti 21S, fully stabilized beta is the main phase in this system.

Pole figures for the <110>, <100>, and <111> orientation from the top and cross sections are depicted in Figure 3-5. A preferential crystal growth orientation <100> is observed in the building direction *z* as well as in both the *z*–*y* and *z*–*x* planes, in agreement with the results obtained previously for different β-Ti alloys (Vrancken et al. 2014; Ishimoto et al. 2017). This preferred orientation can be considered a potential source of anisotropy, which will plausibly result in mechanical properties changing along different directions.

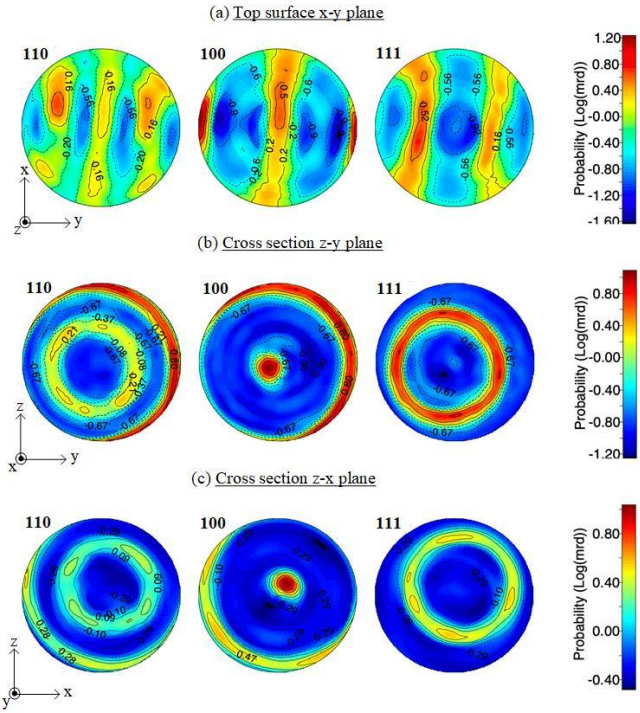

Figure 3-5 : Pole figures were taken from x–y, z–y, and z–x planes, indicating <100> texture in parallels planes to the building direction Z.

3.2.3 Mechanical properties

The mechanical behavior of β-Ti21S alloy is well described by the engineering stress–strain curve showing an initial linear elastic region followed by a very intense work softening (Figure 3-6). The mechanical properties are listed in Table 3-1 and compared with data found in the literature for other Ti-alloys. Where available, the mechanical properties are indicated as mean ± standard deviation. Looking at Figure 3-6, it can be noted that the three replicated tensile tests lead to stress–strain curves exhibiting a flow softening resulting in a marked stress drop. This behavior, recently reviewed in (Kumar et al. 2019), has been ascribed to the planar inhomogeneous plastic flow aided by localized adiabatic temperature rise. This is supported by the formation of intense planar slip bands, which originate from the relatively easy shearing of a thermal ω phase precipitates as well as their dissolution (Agarwal et al. 2008). The work softening could be prevented in Ti-5Al-5V-5Mo-3Cr-0.5Fe system

after super transus heat treatment transforming the β columnar structure into equiaxed. In this way, the tensile anisotropy in L-PBF β alloy can be also avoided (Zafari et al. 2022).

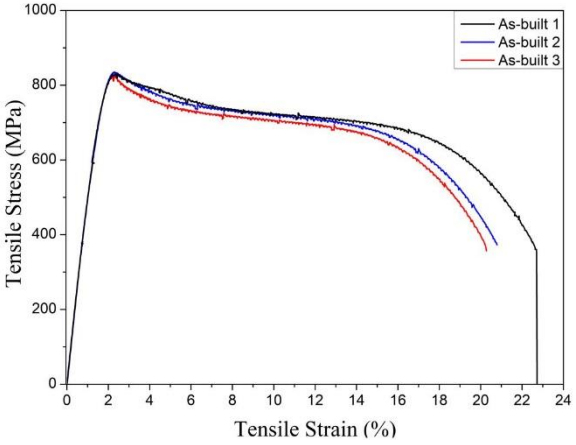

Figure 3-6 : Stress–strain curves of the β-Ti21S produced by L-PBF under tensile loading along the z-direction.

Table 3-1 : Mechanical properties of present β-Ti21S alloy compared with those reported in the literature for additively manufactured and wrought (W) Titanium alloys.

Alloy	$\sigma_{y0.2}$ (MPa)	UTS (MPa)	E (GPa)	El (%)	Structure	Reference
Ti–6Al–4V ELI[1,*]	1015	1090	113	10	α'	(Benedetti et al. 2017)
Ti–6Al–4V[*]	990 ± 5	1095 ± 10	110 ± 5	8.1 ± 0.3	α'	(Facchini et al. 2010)
Ti–6Al–4V + 10Mo[**]	858 ± 16	919 ± 10	73 ± 1	20 ± 2	β	(Vrancken et al. 2014)
Ti–7.5Mo[*]	570	740	70	9.2	α + β	(Kang et al. 2019)
W–Ti21S 0°[2]	852 ± 1	867 ± 5	-	16.4 ± 0.0	β	(Kumar et al. 2019)
W–Ti21S 45°[2]	859 ± 11	884 ± 0.6	-	13.5 ± 0.3	β	(Kumar et al. 2019)
W–Ti21S 90°[2]	797 ± 8	810 ± 14	-	16.7 ± 0.7	β	(Kumar et al. 2019)
β-Ti21S[*]	709 ± 6	831 ± 3	52 ± 0.3	21 ± 1.2	β	This study

σy 0.2: 0.2% yield stress; UTS: ultimate tensile strength; E: young's modulus; El: fracture elongation.

1. ELI = extra Low interstitials, 2. W = wrought β-Ti21S alloy samples cut from rolled sheet; the angles (expressed in degrees °) highlight the orientation of sample with respect to the rolling direction. *Tensile test sample axis parallel to the building direction. **Tensile test sample axis perpendicular to the building direction. Where available, mechanical properties are indicated as mean ± standard deviation.

The mechanical strength (UTS:831±3) is slightly lower than that reported (UTS:810±14) for the same wrought alloy (sheet 0.56 mm) in the solution heat treated condition (Table 3-1), but the fracture elongation is higher (21% for AM Beta21S, 16.4% for the wrought alloy). As expected, the strength is much lower than that of annealed α + β AM–Ti–6Al–4V (Sansoz, Almesallmy, and Ghonem 2004; Benedetti et al. 2017), but the result is worthy of attention, considering that the present figures were obtained without heat treatment. On the other hand, the high fracture elongation provides the condition for avoiding the heat treatment after additive manufacturing. Preliminary results using cantilever beam samples confirm that samples undergo very limited distortion compared with standard α+β AM–Ti–6Al–4V and that any thermal stress during laser processing could be accommodated. The elastic part of the stress–strain curves depicted in Figure 3-6 is affected by very low scatter, as also confirmed by the low standard deviation of the elastic modulus reported in Table 3-1. A fundamental result of this work is the extremely low value of the Young's, namely 52 ± 0.3 GPa, that is, about half of that of Ti–6Al–4V, which helps to prevent stress-shielding, maintaining at the same time an acceptable yield stress even higher than that of Ti–Nb–Ta–Zr (TNTZ) β-type alloys (σ_y=680MPa and E=64GPa) (Luo et al. 2019). Comparing this result with those reported in the existing literature, the property dispersion band of this material is clearly narrower. Even considering a very conservative 6 sigma approach, the dispersion band of the Young's modulus of the present material is not overlapped with that of the other materials.

Figure 3-7 displays the typical fracture surface of the tensile test sample. The cup-cone fracture clearly confirms the ductile fracture mechanism. Three distinct zones can be distinguished in Figure 3-7a. In the fibrous zone near the center (Figure 3-7b), dimples with different sizes are shown. It can be inferred that a large amount of plastic deformation, and hence energy, may occur before fracture, as confirmed by the high fracture elongation of this alloy.

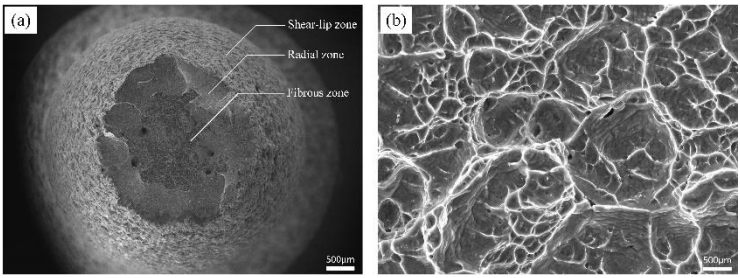

Figure 3-7 : Fracture surface of β-Ti21S tensile test samples showing three zones typical of a ductile mechanism. (a) Overview and (b) Detail illustrating the fibrous.

Figure 3-8 shows the compression stress–strain curves recorded along three different directions. A first interesting difference with respect to the tensile test curves is the steady strain hardening after yielding. A second important result is the different elastic modulus along the x (64±0.7 GPa), y (61±0.9 GPa), and z (52±0.5 GPa) directions. As expected, the lowest value is measured along the building direction, showing the minimum value, about 15–19% lower than those in the other two directions. On the other hand, the compressive strength is slightly higher along the BD, z. The gap is likely owing to the crystallographic texture evidenced by the pole figures. This anisotropy effect is also confirmed by the different hardness measured on the top (280±2 HV0.1) and lateral surfaces (298±3 HV0.1) of cylindrical samples.

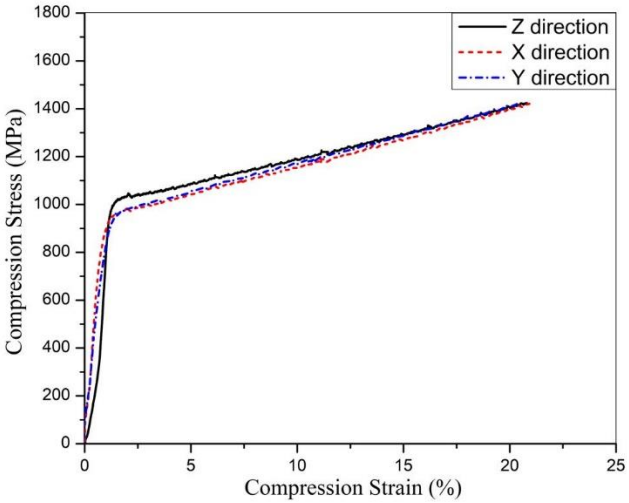

Figure 3-8 : Stress–strain curves of the β-Ti21S produced by LMF under compression loading along the z-direction.

The mechanical anisotropy in β-Ti alloys is the result of a complex set of factors including texture and well as microstructural characteristics like grain size, morphology, the presence of any α phase within the parent β matrix, extent of dynamic recrystallization in the case of hot deformation, and formation of in-grain shear bands in the deformed state (Stráský et al. 2018). There are different forms of anisotropy: i) Structural (crystallographic), ii) Microstructural (columnar grain). A first source of anisotropy is the microstructure produced by the layer-wise nature of the AM process; mechanical properties are influenced by the orientation of the melt pool boundaries with respect to that of the applied stress. This is eventually emphasized

by the presence of local defects like lack of fusion. Moreover, another important source of anisotropy is the columnar grains, aligned parallelly to the build direction. This effect was previously claimed to be the main cause of mechanical properties anisotropy in Ti–6Al–4V produced by AM, particularly strength and fracture elongation (Carroll, Palmer, and Beese 2015). However, alterations in the linear elastic behaviour have been investigated in far less detail and the few existing studies are not in agreement. Rehme et al and Chen et al (Rehme and Emmelmann (2006) and; Chen et al. (2017) did not evidence any dependency of the Young's modulus on the polar angle. On the basis of the results of Hitzler (Hitzler et al. 2017), however, important deviations in the elastic modulus were evidenced for 316 stainless steel. The nature of these deviations has not been explained, on a theoretical basis, but it is plausible that they are related to the different bonding strength along different crystallographic directions (Figure 3-5).

The R_a and R_z surface roughness values before and after machining are listed in Table 3-2. The result of fatigue tests of both as-built and finished materials is plotted in Figure 3-9. The best-fit parameters representing the fatigue curves are also listed in the Table 3-3. As expected, the fatigue strength of the as-built material is lower than surface finished one. The fatigue fitting curve of as-built sample shows a knee around the 1×10^6 cycles. However, the fatigue curve for the finished surface condition steadily declines with the fatigue life. Furthermore, the scatter in fatigue data is also remarkable, showing the higher scattering of the data in the high-cycle fatigue range ,which may stem from the presence of internal defects. These results are consistent with the results of as-built Ti-6Al-4V additively manufactured (Li et al., 2016), but in comparison of the heat-treated Ti-6Al-4V alloy (Benedetti et al. 2017) the fatigue properties should improve. This might stem from the internal defects, even in low amount, and columnar structure oriented along the building direction (BD) of the β - Ti21 alloy which are very detrimental for the fatigue properties (DebRoy et al. 2018). More studies are needed to improve the fatigue resistance and understanding the fatigue behavior of this alloy in the different surface roughness conditions.

Table 3-2 : Surface roughness properties.

Alloy	R_a (µm)	R_z (µm)	R_{max} (µm)
As-built surface	4.4	26	26
Finished surface	0.2	2.3	0.3

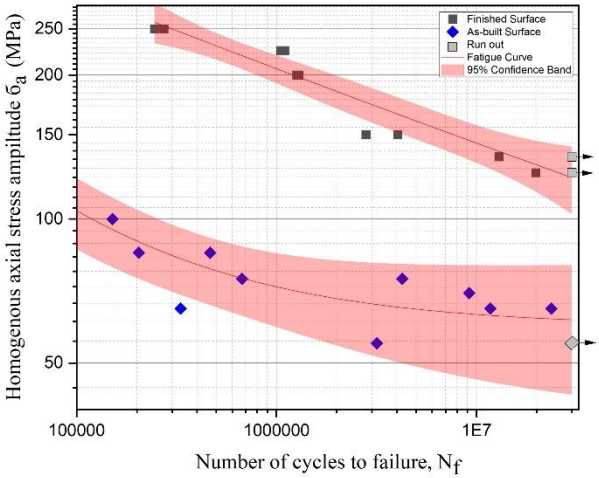

Figure 3-9 : SN curves of as-built and surface finished of L-PBF Ti-21S alloy.

Table 3-3 : Principal results of the fatigue tests.

Condition	C1 (MPa)	C_2	m	S (MPa)
As-built surface	59.62	25142	0.55	3.50
Finished surface	15.97	2034	0.17	3.19

The fracture surfaces of the fatigued components investigated by SEM shown in Figure 3-10. The failure types detected are different for the as-built and finished surface conditions. The local site of crack initiation for the as-built surface (see arrow), is a pore found at or in the vicinity of the surface and, in its near locations. Fracture surface of the surface finished samples evidences crack initiation also near the surface locations, but mostly lack of fusion defects. Typically, surface voids, lack of fusions, and porosities causes stress concentration that promotes the early stages of crack propagation, hence reducing the fatigue resistance of the additively manufactured components (Benedetti et al. 2017).

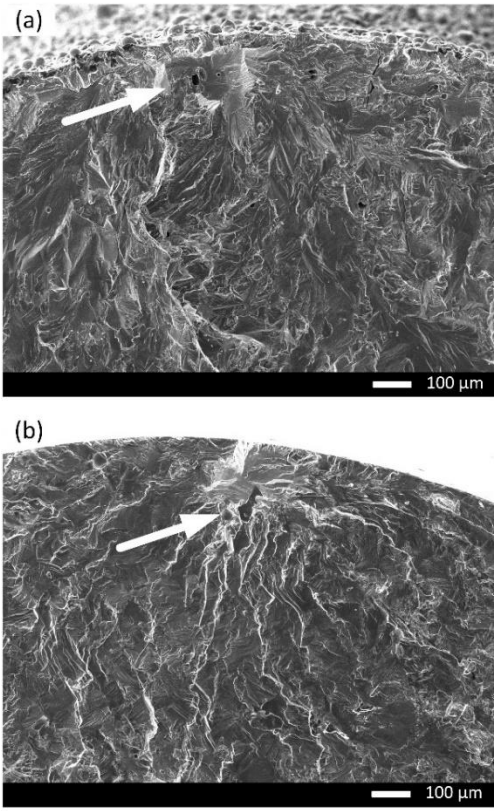

Figure 3-10 : SEM micrographs of L-PBF beta-Ti21S fracture surfaces around the fatigue crack initiation sites of a) as-built and b) surface finished samples after 10 million cycles (the withe arrows point the crack initiation sites).

3.2.4 In Vitro Cytotoxicity

The results on the evaluation of MG63 cultured with experimental materials, reference materials, and controls are summarized in Figure 3-11 (viability test), Figure 3-12 (LDH), Figure 3-13 (Neutral Red uptake), and Figure 3-14 (Phalloidin and Neutral Red staining). The viability results showed that β-Ti21S (test) and Ti–6Al–4V ELI (reference) samples had higher significant viability than CTR+ ($p < 0.0005$) without any difference in comparison with CTR− and with a percentage of viability over 70%; therefore, no cytotoxicity was detected. Moreover, test and reference materials released a lower amount of LDH than CTR+ ($p < 0.0005$) without any difference in

comparison with CTR−; the test sample showed a significantly lower release of LDH even than reference S1 and CTR− ($p < 0.005$). Cytoplasmic membranes of cells exposed to test and reference materials were able to actively uptake Neutral Red vital stain with significantly increased values than CTR+ ($p < 0.0005$); β-Ti21S showed a significantly lower uptake than reference and CTR− ($p < 0.05$). Figure 3-14 shows microscopic images of Phalloidin and Neutral Red vital stainings, performed to highlight cell morphology in the presence of materials. Phalloidin specifically binds to actin filaments of the cell cytoskeleton (Mei et al. 2008), while Neutral Red is actively incorporated within cytoplasmic lysosomes only in vital cells (Borenfreund and Puerner 1985). As for CTR−, experimental and reference samples showed that MG63 had a normal elongated morphology without cell detachment, lysis, or cytoplasmic vacuolization; the integrity and permeability of membranes by means of active transport systems were confirmed by the uptake of the Neutral Red vital stain. By contrast, CTR+ was markedly less in number, presented a rounded morphology, and did not take up the vital dye.

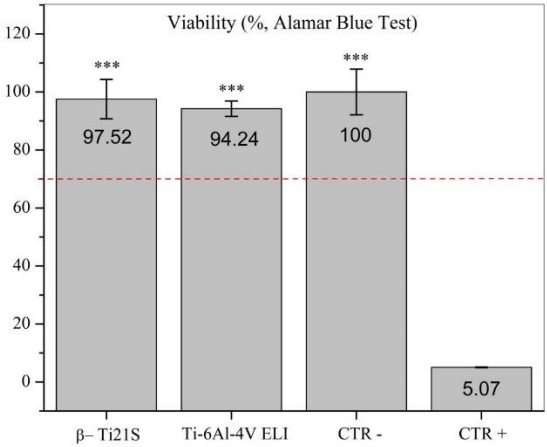

Figure 3-11 : Viability results of the β-Ti21S (test), Ti–6Al–4V ELI (reference), and CTR− (cells without material) and CTR+ (cells with a cytotoxic substance) controls measured by Alamar Blue test and expressed as a percentage of CTR−. Red-dashed line represents 70% of negative control, which is a cut-off line between cytotoxic and non-cytotoxic effects. Kruskal–Wallis followed by the Mann–Whitney U test: β-Ti21S, Ti–6Al–4V ELI , and CTR− *vs.* CTR+, *** $p < 0.0005$.

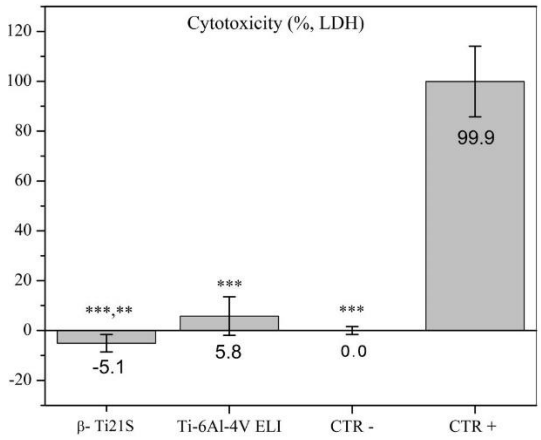

Figure 3-12 : Lactate dehydrogenase (LDH) released by the β-Ti21S(test), Ti–6Al–4V ELI (reference), and CTR− (cells without material) and CTR+ (cells with a cytotoxic substance) controls. Kruskal–Wallis followed by the Mann–Whitney U test: *: β-Ti21S , Ti–6Al–4V ELI and CTR− *vs.* CTR+, $p < 0.0005$; **: β-Ti21S *vs.* Ti–6Al–4V ELI and CTR−, $p < 0.005$.**

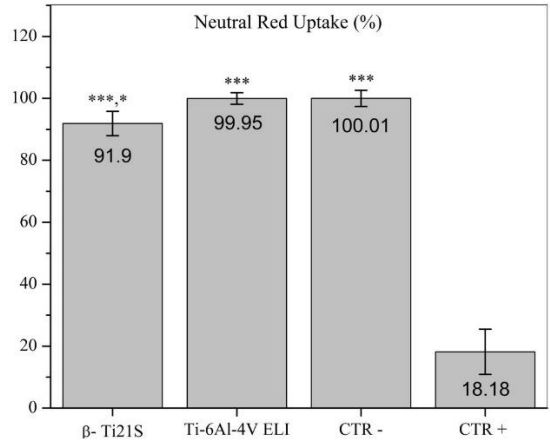

Figure 3-13 : Neutral red uptake quantification of cells exposed to the β-Ti21S (test), Ti–6Al–4V ELI (reference), and CTR− (cells without material) and CTR+ (cells with a cytotoxic substance) controls and expressed as a percentage of CTR−. (Kruskal–Wallis followed by the Mann–Whitney U test. *: β-Ti21S, Ti–6Al–4V ELI, and CTR− *vs.* CTR+, $p < 0.0005$. *: β-Ti21S, *vs.* Ti–6Al–4V ELI and CTR−, $p < 0.05$).**

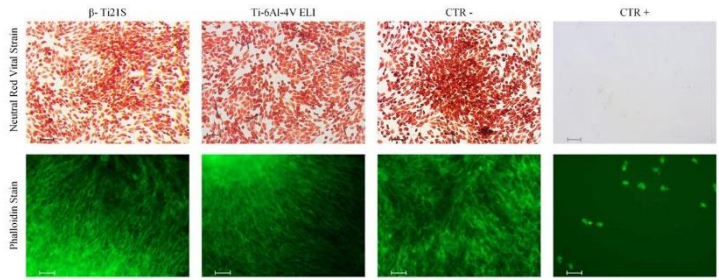

Figure 3-14 : Microscopic images of cells seeded with the β-Ti21S (test), Ti–6Al–4V ELI (reference), and CTR− (cells without material) and CTR+ (cells with a cytotoxic substance) controls. Upper row: cells stained with Neutral Red vital stain (magnification 10×, bar = 100 µm). Lower row: cells stained with Fluorescein Isothiocyanate FITC-conjugate Phalloidin stain (magnification 20×, bar = 10 µm).

3.3 Conclusion of part 1

The results obtained for bulk β-Ti21S alloy highlight that it could be successfully produced by additive manufacturing. The achievement of near full density, low defectiveness, and fine full β-microstructure confirm the suitability of the L-PBF parameters. The suppression of martensitic transformation allows the achievement of a metastable β-structure, thus avoiding the inherent brittle structure observed in the as-built state for $\alpha+\beta$ alloys like Ti–6A–4V. This is made possible by the presence of 15%Mo, which plays a twofold role on the martensitic transformation: first, the critical cooling rate to retain β is decreased, second, the martensitic start temperature is lowered drastically (Vrancken et al. 2014).

Mechanical properties are very encouraging compared with those of similar alloys investigated so far in the technical literature (see Table 3-1). It is worthy to remark that the alloy displays an ultra-low Young's modulus (52 ± 0.3 GPa), less than half of that of Ti–6Al–4V, widely used for biomedical applications. Moreover, it shows good mechanical strength and excellent ductility without the need of heat treatments. This fact is not of secondary importance considering the costs and the critical issues related to the heat treatment of Ti alloys. The experience of some of the present authors evidenced that oxygen as well as nitrogen and carbon pick-up during vacuum annealing of Ti–6Al–4V may lead to low and poorly reliable mechanical properties. An acceptable anisotropy degree could be determined by compression tests, evidencing slightly higher elastic modulus and lower strength perpendicularly to the building direction. The results are promising, looking to the manufacturing of parts undergoing multiaxial loading. Nevertheless, anisotropy should be also verified under tensile

stress conditions, to emphasize any possible influence of the solidification structure, texturing, and defects orientation on mechanical properties.

Considering the detrimental effects of residual stresses in as-built components, those associated to phase transformations are obviously not present in this alloy. On the other hand, thermal stresses can be also reduced owing to the accommodation permitted by the relatively low yield strength and the good ductility of this β-alloy. This is particularly important looking to the future production of larger components than those tested in this paper, as well as to the production of cellular structures, typically used to produce orthopaedic implants.

In vitro cytotoxicity tests results are good, not worse than those of Ti–6Al–4V. The absence of V contributes to the very good biocompatibility attested by *in vitro* cytotoxicity experiments, conducted following the international standard UNI EN ISO 10993-5. In fact, the cell viability was maintained without statistically significant differences with the reference material, without any morphological alterations, and in the absence of the release of cell damage mediators.

Further research is currently underway to investigate the fatigue performance of the present material and its suitability to manufacture cellular lattice structures. Moreover, deeper investigations on biological competence in bioactivity assays using advanced in vitro models and preclinical evaluations of the β-Ti alloy safety and efficacy are mandatory in view of its clinical use for 3D printed implant materials to be used in orthopedic applications with a fully oriented personalized medicine.

Part 2: Laser Powder Bed Fusion of cellular lattice structures

4.1 Introduction

Lattice structures are topologically ordered, three-dimensional open-celled structures composed of one or more repeating unit cells (Zadpoor 2019; Zhang et al. 2018). Lattice materials differ from traditional bulk materials because their properties do not only depend on the base material, but also on the architecture of the unit cell (L. Gibson, Ashby, and Harley 2010; Ashby 2006). Light-weight, superior thermal insulation, high impact response, and numerous other properties have contributed to make cellular materials attractive to the aerospace, biomedical, automotive, and naval industries (Fleck, Deshpande, and Ashby 2010; Maconachie et al. 2019; Rashed et al. 2016; L. J. Gibson and Ashby 1997). For instance, integrating into orthopedic implants tailored porosity gradients of a low modulus lattice at the interface with the bone tissue can mitigate stress-shielding, a frequent cause of implant failure (Sumner 2015; Arabnejad et al. 2016; Tan et al. 2017; A. Zadpoor 2017). Such applications require lattices with tailored architecture: additive manufacturing (AM), as a layer-by-

layer process, has a clear advantage over traditional technologies in the fabrication of such structures. Laser powder bed fusion (L-PBF) is one of the most important metal additive manufacturing processes, consisting of building up a metal part by locally melting a metal powder with a focused laser beam (Murr et al. 2012; DebRoy et al. 2018b).

Despite L-PBF was proved to be suitable to produce high quality complex lattices (A. Zadpoor 2017; Arabnejad et al. 2017), the properties of printed parts can deviate significantly from those predicted assuming an ideal geometry and homogeneous properties of the base material (Pasini and Guest 2019). Indeed, the manufacturing process markedly affects material microstructure and micro-architecture with an outcome that impacts mechanical and biological performance (Dong, Tang, and Zhao 2017; A. A. Zadpoor 2017). The microstructure of additively manufactured parts is affected by high cooling rates and preferential grain growth direction caused by the directional heat flow, which lead to the formation of low ductility metastable phases in many metallic alloys and to anisotropy (Weißmann et al. 2017; 2016; Wauthle et al. 2015; Zhang, Li, and Bai 2017). High temperatures and fast cooling are also the origin of residual stresses that, besides altering the mechanical properties, can also cause distortion of the lattice (A. A. Zadpoor 2017; Dallago et al. 2019a). In addition, internal porosity can arise due to entrapped gas and lack of fusion defects (Herzog et al. 2016).

The micro-architecture of a lattice produced by AM can be altered by several types of geometrical defects and imperfections (Maconachie et al. 2019; Melancon et al. 2017; Takano et al. 2017; Bagheri et al. 2017; L. Liu et al. 2017). The defects in the lattice material can be divided into i) bulk defects (i.e., internal porosities, geometrical deviation) and ii) surface defects (i.e., surface irregularities and attached unmelted powder). Attached unmelted powder particles increase the surface roughness (Dong, Tang, and Zhao 2017). On a larger dimensional scale, the size of the melt pool, which is determined by the laser energy input and by the local heat transfer properties of the solid/powder system (Qiu et al. 2015; Sing, Wiria, and Yeong 2018) significantly affects the geometry of the lattice, e.g., strut thickness, strut straightness, junction alignment and junction shape (Dallago et al. 2019a; Bagheri et al. 2017). In general, such defects or imperfections are not uniformly distributed over the lattice but, due to gravity effects, mostly affect the struts built at a low inclination angle with respect to the building plane (Bagheri et al. 2017; Wauthle et al. 2015; S. Murchio et al. 2021).

Studying the geometrical defects and imperfections in the lattice structures is challenging. For example, 2D characterization methods like microscopic investigation have in-plane limitations and cannot reveal all manufacturing-related issues. Thus, the use of 3D characterization techniques, like Micro-CT scanning, is steadily

increasing for the investigation of lattice structures (du Plessis et al. 2018). The data gathered by this method contributed to a better understanding of bulk and surface flaws introduced by additive manufacturing processes. CT data can be transferred, as STL files, to other platforms for metrological analyses. Moreover, CT data can be also used as input for the numerical analyses by FE modeling (Dallago et al. 2019b). However, this approach is not fully mature, yet, since the input model built using Micro-CT data involves many fine features, especially on the surface, which cannot be accurately described by the meshes. This results in the loss of important information on the surface, and opens a new challenge for researchers, viz. extending the ability of FE models to predict the perturbations caused by surface imperfections on the stress field of lattices. Until now, to reduce the long computational time associated with complex FE modelling, researchers simplify the problem by modelling a representative volume element (RVE) with the periodic boundary condition instead of the entire lattice CT data (Lozanovski et al. 2020; Raghavendra, Molinari, Dallago, et al. 2021b). On one hand, this reduces the computational cost of the problem, but, on the other hand, the adopted boundary conditions do not well represent the real situation, mainly due to the impossibility to correctly reproduce geometrical deviation caused by the manufacturing process.

The effect of manufacturing defects and imperfections on the quasi-static mechanical properties (elastic modulus and strength) has been addressed experimentally by several studies (L. Liu et al. 2017; Qiu et al. 2015; Lozanovski et al. 2019; Dallago et al. 2019b). A poor strut straightness (waviness) and misalignment of the nodes cause a loss of stiffness and strength due to the enhanced bending actions, particularly in stretching dominated lattices (Benedetti et al. 2021), whose real static mechanical behavior significantly deviates from the theoretical one predicted by Gibson and Ashby equation (Gibson and Ashby 1997). In contrast to the elastic modulus and other monotonic properties, fatigue, a highly localized phenomenon, is very sensitive to the microstructural and morphological quality of a component and thus is extremely sensitive to the manufacturing process and such defects (Benedetti et al. 2021). For example, the low fatigue strength of as-built L-PBF parts compared to machined or wrought parts is partly determined by the poorly homogeneous solidification microstructure, but even more by high surface defectiveness (Vayssette et al. 2018; Fotovvati, Namdari, and Dehghanghadikolaei 2018). In particular, the fatigue behavior of L-PBF lattices is negatively impacted by the high roughness, as well as by irregularities in the strut cross-sections that act as notches (Ren et al. 2019; Dallago et al. 2018; 2019b). α+β Ti alloys, such as Ti-6Al-4V, are especially sensitive to stress raisers due their high notch sensitivity (Niinomi 1998a). An effective design measure to attenuate stress concentration effects is to provide the lattice with filleted nodes: recent investigations reported in (Dallago et al. 2021) attested an increment by a factor 2 in the fatigue strength of a lattice with filleted

cubic unit cells with respect to its non-filleted counterpart. In addition, the authors demonstrated in (Dallago et al. 2021) that lattices of cubic unit cell smaller than 2 mm are more affected by geometrical imperfections and consequently by poor fatigue properties, thus suggesting the existence of a manufacturing threshold in the unit cell size, below which the fatigue properties become unacceptably poor. Such limits depend on the material, powder size and process parameters used, and require careful studies to be determined. In the case of biomedical implants, unit cell size larger than 2 mm leads to too large pore sizes that are not ideal for the application. This drawback can be overcome or at least mitigated by filling the large voids left by the metallic lattice with a porous osteoconductive foam therein inserted. The feasibility of this approach is a matter of ongoing investigations in our research group.

The present work is aimed at extending the above-described investigations to the fabrication of cellular lattice structures made of a β-Ti alloy, namely β-Ti21S, originally devised for aeronautical applications where it is processed through conventional forming and subtractive processes (Lütjering and Williams 2007), and here applied for the first time to additively manufacture lattice materials. The reasons for the interest in this alloy as a replacement of the conventional golden standard Ti-6Al-4V alloy are manifold: (i) β-Ti alloys display a lower bulk Young's modulus (typically 50 GPa < E < 100 GPa (Pellizzari et al. 2020)), thus are more suitable to fabricate low stiffness orthopedic implants with reduced stress shielding issues; (ii) the chemical formulation of many β-Ti alloys permits to either avoid or reduce the presence of potentially cytotoxic alloying elements, thus ensuring improved biocompatibility properties (K. Vanmeensel et al. 2018); (iii) in suitably formulated β-Ti alloys, the martensitic transformation, inevitably occurring in Ti-6Al-4V due to the fast cooling rates typical of L-PBF, can be suppressed, thus reducing the associated volumetric expansion responsible for undesired residual stresses and distortions (Ahmed and Rack 1998b); (iv) β-Ti alloys display very high ductility, even without the necessity of a post-fabrication heat treatment (which is instead mandatory for Ti-6Al-4V) (Pellizzari et al. 2020). Clearly, this is an advantage, as a high ductility permits to attenuate stress concentrations and therefore to fabricate fatigue-resistant cellular lattice materials (Benedetti et al. 2021). In addition to the lack of martensitic transition, resulting in less residual stress formation for this alloy compared to Ti6Al4V, in this study the samples are manufactured with an optimized scan strategy to minimize the formation of thermal residual stress, allowing the as-built condition to be used without a need for further heat treatment.

The existing literature about the use of β-Ti alloys in the fabrication of cellular lattice structures is very limited (Y. J. Liu et al. 2017a; Luo et al. 2020). Liu et al. (Y. J. Liu et al. 2017a) investigated the compression-compression fatigue strength of porous structures of β-Ti alloy Ti2448 additively fabricated via electron beam powder

bed fusion (EB-PBF) and compared it with that of counterparts made of Ti-6Al-4V. Comparing the fatigue strength at equal stiffness, the porous structures made of β-Ti alloy exhibited superior performance. However, the lower manufacturing accuracy of EB-PBF in comparison to L-PBF and the absence of filleted nodes resulted in preferential fatigue crack initiation at the strut junctions and in a low value of the fatigue strength normalized to the yield strength (0.17). Luo (Luo et al. 2020) tested the compression-compression fatigue resistance of cellular lattice specimens of a Ti-Nb-Ta-Zr alloy additively manufactured via L-PBF. The good manufacturing accuracy permitted to achieve a higher normalized fatigue strength of 0.33, still low in comparison with the fatigue performance exhibited by metamaterials made of other ductile metallic materials, like CoCr alloy and stainless steels (Benedetti et al. 2021).

To overcome the above-discussed manufacturing-related fatigue issues, the following part of this thesis is aimed at assessing the manufacturability of metamaterials made of β-Ti21S additively manufactured via L-PBF. For this purpose, cubic cellular lattice structures of different unit cell size and different strut thickness have been firstly fabricated and characterized through microstructural analyses and computed tomography scans combined with linear elastic finite element simulations to identify the minimum cell size that can be printed with adequate geometrical accuracy. Samples of the selected unit cell size were also physically tested to determine their static and fatigue properties. Finally, an octet truss structure with suitable cell size was designed and characterized.

4.2 Result and discussion

Part 2-1: Manufacturability

4.2.1 Geometrical deviation and morphological investigation of RVEs

To evaluate the overall manufacturing accuracy, the reconstructed Micro-CT data of the RVE samples were compared to the design file and the deviations were mapped in color coding in 3D (Figure 4-1). The overall overlap is good with low deviations: the deviations were mainly less than 0.2 mm, with limited unexpected features. The largest positive deviations (0.1 mm - 0.2 mm excess material) for all RVE samples were often recorded in the downward surface of the joints facing the build platform (red color). This variance seems to be ascribed to the agglomeration of the powder attached to the joint, typically called “dross” (DebRoy et al. 2018). The possible impact of this defect on mechanical properties will be discussed in the FEM section. Comparing the two samples in Figure 4-1 (a) and (b), i.e., LPS 0.26 and NPS 0.26, having the same size, the sample with contouring better fitted the CAD design. Figure 4-1 (c) and (d) related to the two larger samples NPM 0.68 and NPL 1.06, show some blue regions in NPL 1.06, which indicate lack of material in specific locations of the larger cell (L=6mm) and thicker struts (t=1.06mm).

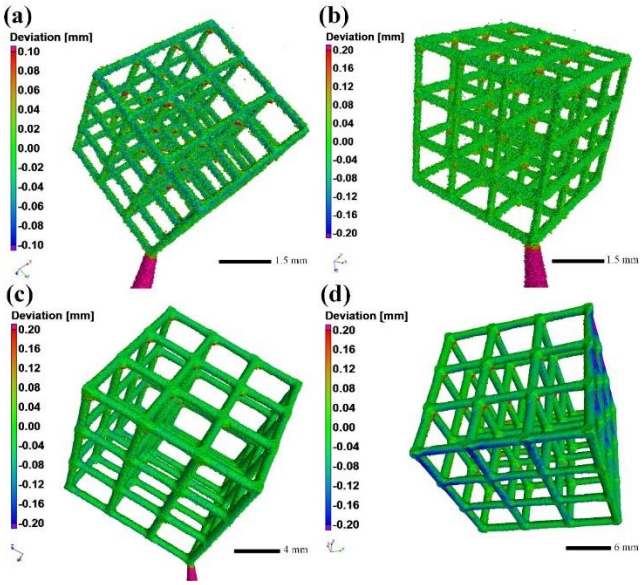

Figure 4-1. Reconstructed Miro-CT data showing the CAD deviation based on the X-ray absorption. (a) LPS 0.26, (b) NPS 0.26, (c) NPM 0.68, and (d) NPL 1.06.

A cross-sectional plane similar to the metallographic one was also singled out in CT data, to evaluate the deviations in more detail (Figure 4-2). In this figure, the CT data is shown in greyscale while the CAD design is overlapped in solid color. All samples had slightly less material overall compared to the design, particularly for the smallest cell size (Figure 4-2a and 5b). Comparing the same cell size geometry (Figure 4-2a and 5b), the sample fabricated with lower laser energy had a more irregular surface with thinner struts present and some critical defects primarily visible in the node regions. The sample with the internal porosities (LPS 0.26) was additionally scanned at a higher resolution (2 µm voxel size) with the result shown in Figure 4-3. It can be observed that the porosities are quite uniformly distributed, but the accumulation of the bigger pores is mostly localized on the node region. Increasing the laser energy reduced the formation of these defects to a great extent and the printed part geometry reached a closer adherence to the CAD design (Figure 4-2b). Increasing the cell size leads to improved fabrication response, leading to less prominent surface irregularities and acceptably low CAD deviation (Figure 4-2c and d).

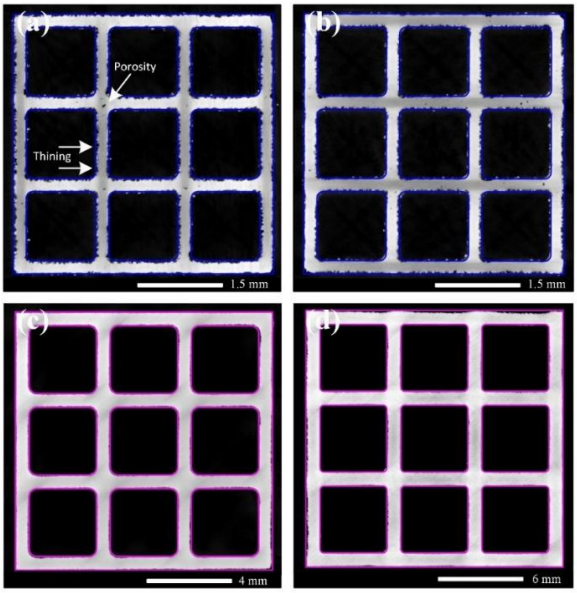

Figure 4-2. The cross-section plane from the reconstructed Micro-CT data for (a) LPS 0.26, (b) NPS 0.26, (c) NPM 0.68, and (d) NPL 1.06 samples. The arrows indicate local thinning and porosity locations. Solid color indicates the design CAD geometry.

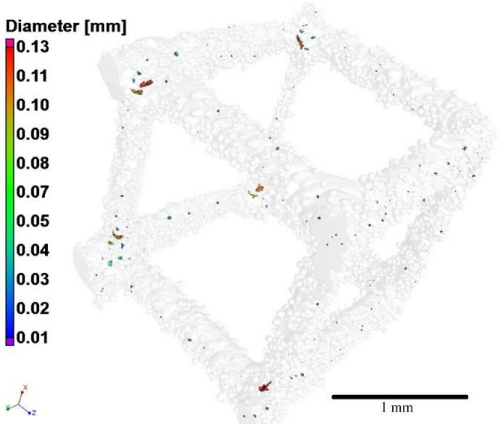

Figure 4-3. The reconstructed high resolution Micro-CT scan data of the sample fabricated with low energy of the laser beam (LPS 0.26) showing the accumulation of porosities on the junction.

The building direction influences the location of attached powder particles and surface morphology. This can be seen in the high-resolution Micro-CT data of single junctions for all the unit cells (Figure 4-4) on which the excessive materials were clearly exposed on corners of nodes and on certain local sides of struts, parallel to the building direction (note building direction diagonal in the image). This parasitic mass was localized (in the lower volume) only at the downskin side of junction of larger cell size (Figure 4-4c and 4-4d). The cross-section shape of struts was elliptical shape with the main axis oriented along the build direction (Figure 4-4a and 4-4b). Smaller deviations can be discerned when the unit cell size increased to manufacturable sizes (Figure 4-4c and 4-4d). For purpose of comparison, Figure 4-4e illustrates the Micro-CT reconstruction of a single junction additively manufactured using a conventional Ti-6Al-4V powder (detail about the fabrication process can be found in (Murchio et al., n.d.)) and having the same nominal geometrical characteristics as NPM 0.68 shown in Figure 4-4b. Even though some discrepancies may be ascribed to differences in building direction and L-PBF machine, it is unquestionable that the use of β-Ti21S allows much better dimensional accuracy, especially in terms of cross-section circularity, uniformity in strut thickness and absence of parasitic mass altering the fillet surfaces at the node. Evidently, the absence of martensitic transformation and the ductility even in the as-built condition contribute to the better manufacturability of β-Ti21S. A systematic metrological comparison between structures fabricated with Ti-6Al-4V and b-Ti21S is postponed to a dedicated future investigation. In this paper, we focus on the metrological characterization of β-Ti21S, only.

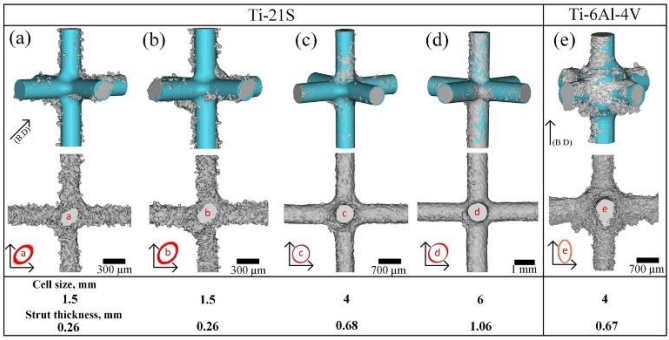

Figure 4-4. Reconstructed Micro-CT data of (a) LPS 0.26, (b) NPS 0.26, (c) NPM 0.68, and (d) NPL 1.06 samples showing the CAD deviation inclination in 3D by overlapping data to the CAD design (first row) and in-plane (second row) views. (e) junction fabricated via L-PBF using conventional Ti-6Al-4V alloy with geometrical parameters similar to NPM 0.68 (c).

There has been speculation about the effect of waviness and CAD deviation on the mechanical properties of additively manufactured lattice structures (Seiler et al. 2020; Moussa et al. 2021). Analytical models have also evidenced that the strut waviness has a direct influence on the mechanical properties (Dallago et al. 2019c). The result of the waviness factor normalized to its nominal strut length is depicted in Figure 4-5a. Increasing the cell size and the strut thickness had a direct positive effect on struts waviness, which reduced below 0.1 for cell length above 4 mm and strut thickness higher than 0,68 mm, i.e. for samples NPM 0.68 and NPL 1.06.Generally, it can be observed that the AM specimens fabricated for this study have an insignificant degree of waviness (close to zero) along the different strut directions, horizontal and vertical axes (see the Figure 2-4 for better understanding of the axes and building direction). Also, the results of eccentricity measurements confirm the beneficial effect of a bigger cell size and strut thickness (Figure 4-5b), i.e., for samples NPM 0.68 and NPL 1.06. These plots also depict that the 45-building direction had almost same fabrication response for various struts directions (X, Y, and Z).

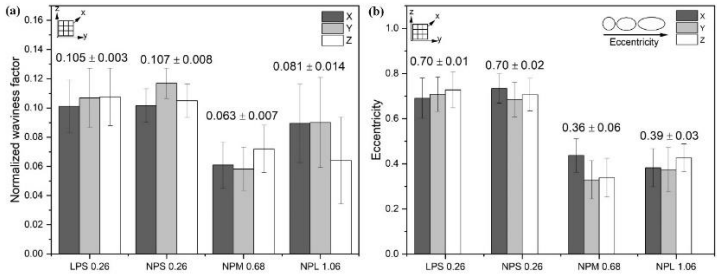

Figure 4-5. Normalized waviness factor respect to the nominal strut length and eccentricity for various samples cell sizes. X, Y, and Z are representing the strut direction. Note that an ideal value for the perfectly straight and round struts should be zero.

The measured morphological properties of various cell sizes are listed in Table 4-1. The actual values of Relative Density (RD), measured by dry weighing and Micro-CT imaging, were lower than designed value (0.097). The RD values ranged between 0.072 and 0.090, showing that the discrepancy between the experimental value and the designed one reduced by increasing the cell size because laser resolution is limited for applying both hatching and contouring scan strategies for the small cell sizes (LPS 0.26 and NPS 0.26), led to the higher CAD deviation.

The strut thickness values, measured by spherical method and 2D imaging (SEM), were all slightly lower than CAD design, and more precise than those measured with the Micro-CT scanning (Figure 4-6a), although the spherical method has been known as a more reliable approach in 3D-imaging (Dallago et al. 2019b),

due to the difficulty of sectioning the exact middle of the strut and incorporating asymmetry. The nodal size, calculated by fitting the sphere, is strictly attributed to the slumping defect formed on the corner of the junction. The spherical thickness measurement method in 3D allowed the quantification of attached powder particles. From Figure 4-6b, it is clear that CT-scan is better method for nodal size measurement, particularly by increasing cell size/strut thickness and SEM seems to be more precise for strut thickness measurement.

This section, reporting a detailed characterization of different lattices structures, suggests that a strut thickness of more than approximately 0.5 mm is necessary for good manufacturability of this alloy.

Table 4-1 : The morphological properties of various cell sizes.

Sample	RD[1] (-)		Strut size (mm)			Node size (mm)			Surface imperfections[2] (mm)
	Dry weighing	Micro-CT	CAD	Micro-CT	SEM	CAD	Micro-CT	SEM	Micro-CT
LPS 0.26	0.072 ± 0.04	0.076 ± 0.10	0.26	0.137 ± 0.01	0.238 ± 0.01	0.38	0.170 ± 0.06	0.456 ± 0.59	0.034 ± 0.007
NPS 0.26	0.084 ± 0.01	0.091 ± 0.09	0.26	0.182 ± 0.01	0.245 ± 0.01	0.38	0.297 ± 0.01	0.566 ± 0.12	0.036 ± 0.006
NPM 0.68	0.083 ± 0.01	0.087 ± 0.06	0.68	0.570 ± 0.01	0.615 ± 0.05	1.01	0.920 ± 0.02	1.26 ± 0.01	0.11 ± 0.05
NPL 1.06	0.087 ± 0.01	0.090 ± 0.03	1.06	0.920 ± 0.03	1.03 ± 0.01	1.41	1.37 ± 0.04	1.79 ± 0.01	0.13 ± 0.05

1. The as-designed Relative Density (RD) for all geometries was 0.097,

2. This is herein named the attached powder to the surface

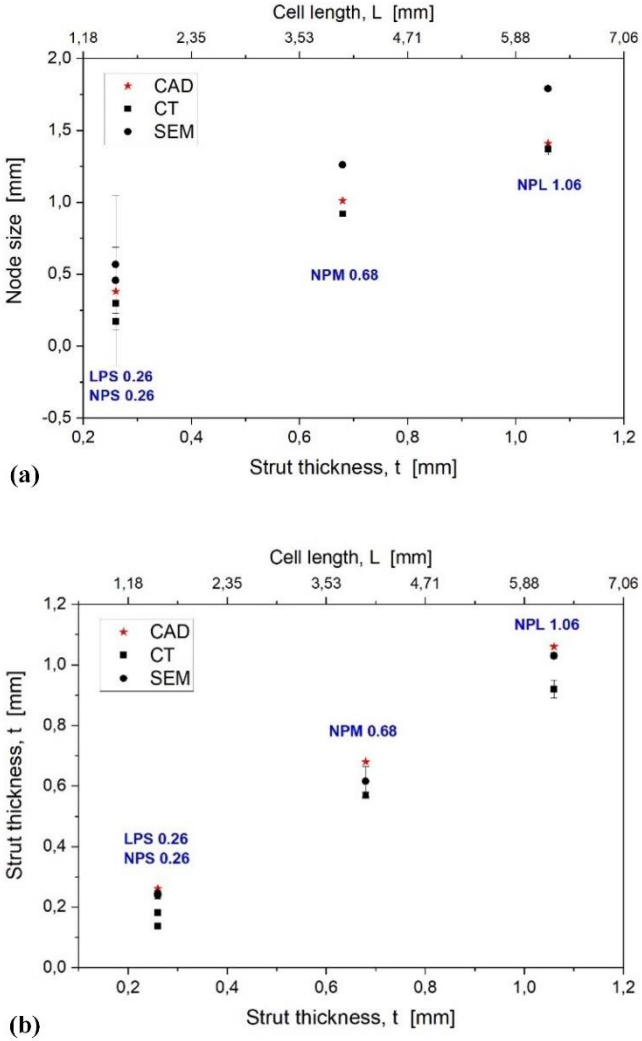

Figure 4-6. Comparative morphological properties of various cell size measured by CT scan and SEM. (a) nodal measurement and (b) strut thickness.

4.2.2 Microstructural analysis

The microstructural characterization on a metallographic cross section of cellular structure was useful to investigate the influence of processing parameters (e.g., the laser energy and contouring) on some important microstructural features such as the melting pool shape, surface quality (partially melted powders, notches) and bulk defects (pores, lack of fusion).

A first general observation can be made comparing the microstructure of initial powder (Figure 4-7a) with that of the L-PBF lattice material (Figure 4-7b). In particular, these two micrographs emphasize the solidification microstructure in the (1) starting powder, (2) partially melted powder, (3) completely melted powder, and (4) fully solidified β-Ti21S lattice material. In all cases the microstructure is cellular, but with a cell size decreasing, for instance from 5 ± 1.8 μm to 0.5 ± 0.3 μm for the sample size 0.26 mm strut thickness (NPS 0.26), in agreement with the stronger refinement caused by rapid solidification during the L-PBF process, as also reported previously for the bulk samples (Pellizzari et al. 2020). The boundaries of partially melted powders as well as the melt pool boundaries evidence the epitaxial growth, as confirmed by the crystals growing across them.

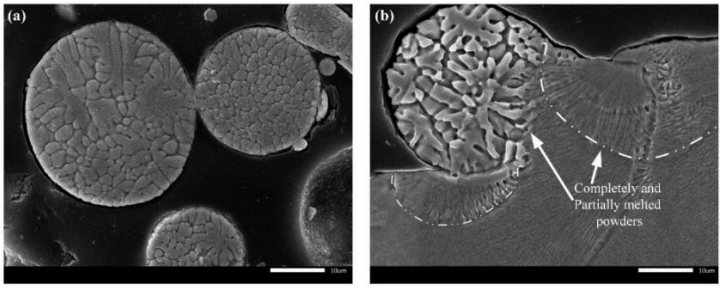

Figure 4-7. SEM micrograph cross section of (a) initial powder and (b) the surface of lattice material showing the solidification development.

4.2.2.1 Influence of laser energy

The micrographs of the two cellular structures fabricated with low laser energy (LPS 0.26) and normal laser energy (NPS 0.26) (Figure 4-8) highlight the influence of laser power. The white lines, resuming the theoretical CAD profile, show a general thinning of both, strut sections and junctions of the structure produced with low power (Figure 4-8a). A slightly better aspect is observed for that produced using normal power (Figure 4-8b).

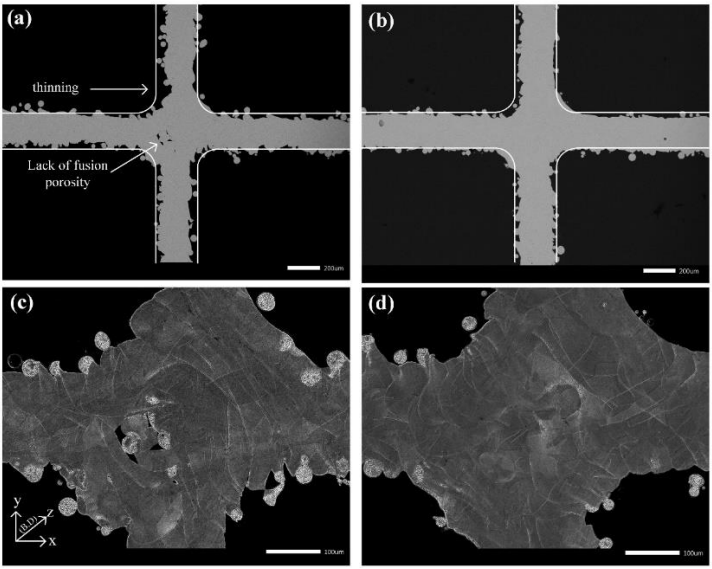

Figure 4-8. Metallographic cross sections of samples fabricated with low and normal energy of laser (a and c) LPS 0.26 (b and d) NPS 0.26 in the same cell size. The arrows show the thinning and Lack of fusion (LOF) porosity.

The geometrical CAD deviation in LPS sample can be ascribed to the small melting pool size caused by the insufficient energy input. The view at higher magnification (Figure 4-8c) also revealed lack of fusion porosity and the presence of unmelted powder particles, particularly in the center of junctions where the cross-sectional area is larger and the volume of powder to be melted is higher.

Lack of fusion appeared as large cavities perpendicular to the building direction with sharp edges (Tang, Pistorius, and Beuth 2017). Their detrimental effect can be described in terms of a local reduction of the load-bearing surface and of the local stress intensification due to the notch-effect of edges. Both, lack of fusions and geometrical precision could be removed by improving the laser energy density (Figure 4-8d).

To investigate the influence of laser energy on surface quality of fabricated parts, the micrographs of two horizontal struts samples were compared (Figure 4-9). These give a general overview of all struts. It is worthy to note that due to the symmetric 45°orientation respect to the building direction, the microstructural quality of horizontal and vertical struts was the same, so that horizontal struts were selected.

In general, the lower laser energy in LPS 0.26 (Figure 4-9a) leads to a higher surface irregularity than in NPS 0.26 (Figure 4-9b), as confirmed by the higher number of notches. Moreover, in LPS 0.26, the difference between upward and downward surface is less evident compared to NPS 0.26. The higher irregularity of downward surface is to be expected based on its relative position with respect to the building direction, as already discussed in the thickness measurement section (Table 4-1). Present results permit to conclude that the lower laser energy power used to improve geometric precision and surface quality in small parts did not lead to positive results, thus confirming that the normal power can be efficiently used also for cellular structures with very thin struts.

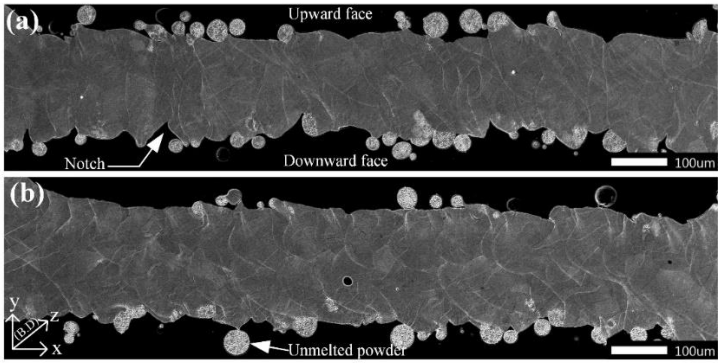

Figure 4-9. SEM micrographs from strut of (a) LPS 0.26, (b) NPS 0.26, showing the effect of laser energy on the surface quality of upward and downward faces.

The role of attached powder particles on the mechanical properties of AM components has been largely debated and led to controversial conclusions (Lee et al. 2021; Maleki et al. 2021). To add a contribution to the discussion, the LPS 0.26 sample was selected for more detailed investigation (Figure 4-10). Attached powders were observable mainly in the downward faces (Figure 4-10a). They may cover surface imperfections such as notches (Figure 4-10b) which may have a direct influence on the local stress concentration and the initiation of cracks in AM components (Afkhami et al. 2021).

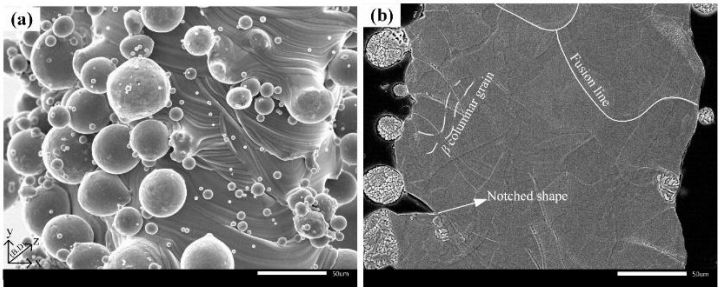

Figure 4-10. SEM images of attached powder over the surface of LPS 0.26 sample, before (a) and after (b) cross sectioning, showing the role of those powders to create surface imperfections.

4.2.2.2 Influence of contouring

By changing the cell size the outer contour appeared quite different in small (LPS 0.26, NPS 0.26, Figure 4-8) and large (NPM 0.68, NPL 1.06, Figure 4-11) cells. In smaller struts (Figure 4-9), the contour is barely visible due to its relatively large thickness compared to that of the cross section. It becomes slightly more evident in nodes (Figure 4-8a and 9d), where the cross section is wider. On the other hand, the contour is clearly visible in large struts and nodes, as highlighted by the dashed lines in Figure 4-11c, 12d and 12e. A comparison with the CAD profile of NPM 0.68, NPL 1.06 evidences a good dimensional accuracy for all features, strut and node thickness, fillet radius curvature and symmetry.

Compared to LPS 0.26, NPS 0.26 samples, LOF are smaller and mostly located at the contour interface, plausibly due to the poor overlap between melt pools printed with different scan strategies. According to micrographs in Figure 4-9a and 10b, it seems that increasing the cell size pores are reduced.

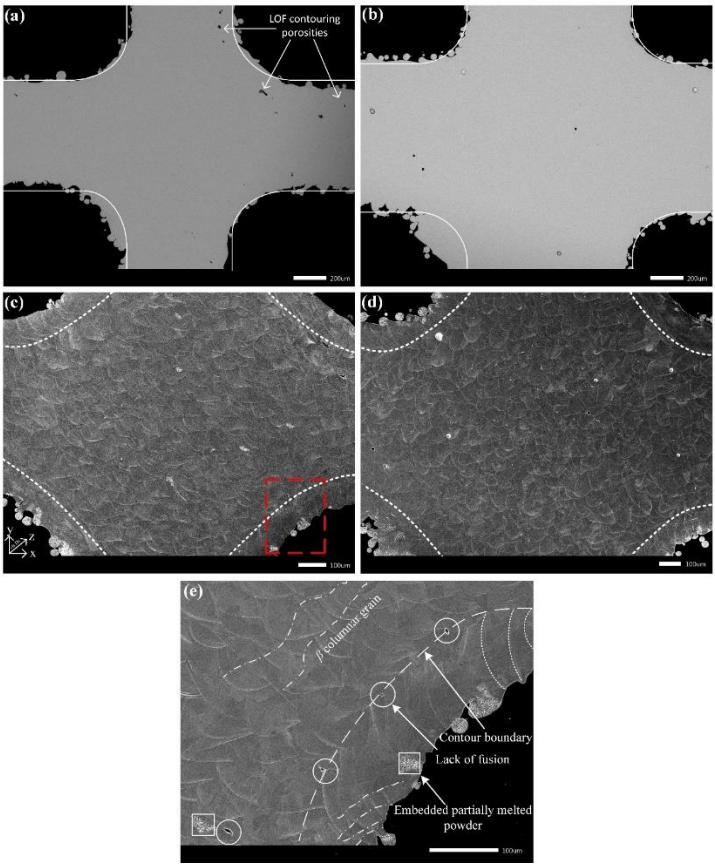

Figure 4-11. Metallographic cross sections of (a,c) NPM 0.68 and (b,d) NPL 1.06 samples, (e) magnified location of red box in (c). The arrows show the lack of fusion (LOF) porosity along the contouring boundary interface (dashed white lines).

The magnified micrograph of the contour boundary region in NPM 0.68 sample (Figure 4-11e) shows two types of defects, namely embedded partially melted powder, mostly located inside the contour, and lack of fusions, at the contour boundary, respectively. This has been reported also by other authors (du Plessis 2021; du Plessis and le Roux 2018). Moreover, even if contouring could remelt powder particles attached to the surface, the micrographs confirm that they could not be completely removed. This can be explained considering that, in spite of the different laser parameters used for the contour, its surface is hot as it solidifies, and

nearby powders can be attached during L-PBF process (Y. J. Liu et al. 2017b; Bari and Arjunan 2019; Leary et al. 2021). Indeed, a lower amount of some isolated unmelted attached powder particles could be also observed in the bulk of samples, suggesting that the printing strategy could be further optimized.

The cross sections of the two representative struts samples of NPM 0.68 (Figure 4-12a) and NPL 1.06 (Figure 4-12b) confirm the higher irregularity of the downward surface already observed in smaller samples, where the inner contour boundary was less evident (Figure 4-10). As expected, both the number of unmelted particles attached powder particles and notches, is reduced by contouring, while there is no apparent influence of the larger strut section.

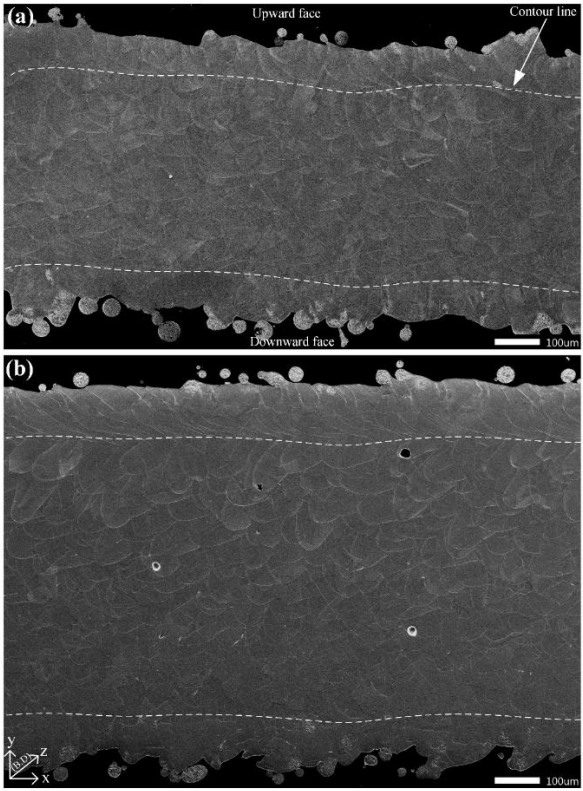

Figure 4-12. SEM micrographs from strut of (a) NPM 0.68, and (b) NPL 1.06, showing the effect of laser parameter and strut thickness on the surface quality of upward and downward skins.

Usually, optimizing of AM process parameters such as layer thickness, hatch spacing, and scanning speed can improve the surface quality, particularly for smaller and thinner structures. On the other hand, the need to fabricate thinner struts to replicate bone scaffold properties is pushing towards post-processing treatment to reduce roughness. Electro-chemical etching has been claimed as the most favorable post-processing technique for lattice structures (Maleki et al. 2021). It has been reported that the surface roughness of AM parts is controlled by the contour and the parameters for its realization such as laser power and laser speed (Leary et al. 2021). However, in this study, a different contouring could not improve the surface quality. The point is that due to the higher strut thickness for the medium and large samples, the effect of surface quality would be probably less critical than the small sample size. It is plausible that Rz value (vertical distance from the highest peak to lowest valley) relative to the strut thickness is the key parameter to describe a suitable surface quality. Comparing Figure 4-9 and Figure 4-12 it can be observed that in the thinner structures the notch depth/strut thickness ratio is higher, leading to a stronger detrimental effect. For this reason, the finite element modeling was carried out using the Micro-CT data to evaluate the influence of surface defectiveness on stress distribution under external loading.

4.2.3 FE modeling

The stress distribution at the junction for ideal CAD 0.26 and as-built LPS 0.26 geometries is shown in Figure 4-13. The vertical load produced by the vertical displacement is almost completely borne by the struts aligned in the same direction, while the horizontal ones are nearly completely unloaded. Therefore, vertical struts and junctions acting as a site of stress concentration are the most critical stress locations. The comparison of the stress field in the as-designed (Figure 4-13a) and as-built (Figure 4-13b) geometries gives a visual and intuitive representation of the role exerted by AM process-induced imperfections in altering the stress state. The orthotropic symmetry in stress distribution displayed by the ideal CAD geometry (Figure 4-13a) is completely lost in the micro-CT model based on the real morphology (Figure 4-13b). This deviation can be mainly ascribed to the deposition of extra material on one of the fillets, to the sharp/incomplete fillet geometry and to surface irregularities. These geometrical imperfections might act as a critical stress raiser when the specimen is subjected to fatigue loading, they experience higher bending stresses and eventually lead to failure at the junction. The extrapolated view of the strut shown in Figure 4-13c shows the presence of another maximum stress location in the strut, far from the junction. It can be seen that surface depressions induce a moderate stress concentration effect. Furthermore, attached powder particles do not seem to act as critical failure locations compared to imperfections that create sharp notches on the surface (Figure 4-13d).

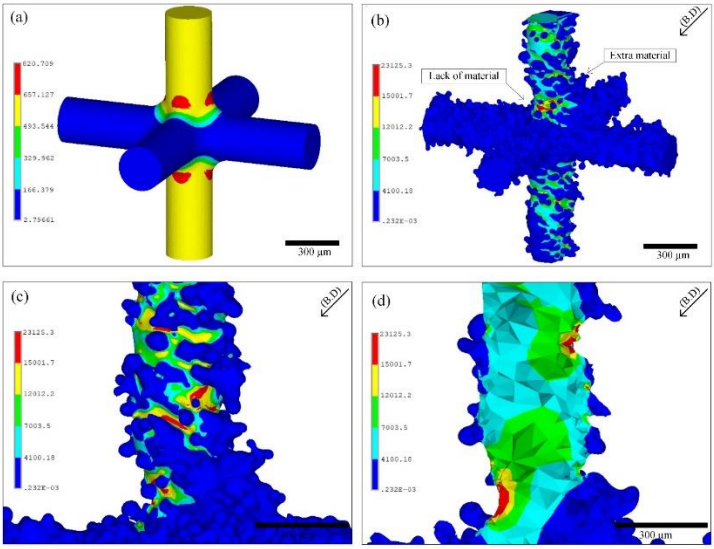

Figure 4-13. Von Mises stress (MPa) contour plot obtained from samples with 1.5 mm cell size. (a) the CAD design, (b) the LPS 0.26 sample, (c) detailed location of LPS 0.26 sample, and its cropped view of the inside stress (d), showing the stress distribution on the junction and struts and the hidden stress concentration location under surface irregularities i.e., attached powder.

To clearly present and quantify the effect of the above-described geometrical imperfections, the stress concentration factor (SCF) was evaluated from the numerically estimated stress fields shown in Figure 4-14. This Figure compares the stress distribution calculated for the four different cell models, and the average SCF values are listed in Table 4-2.

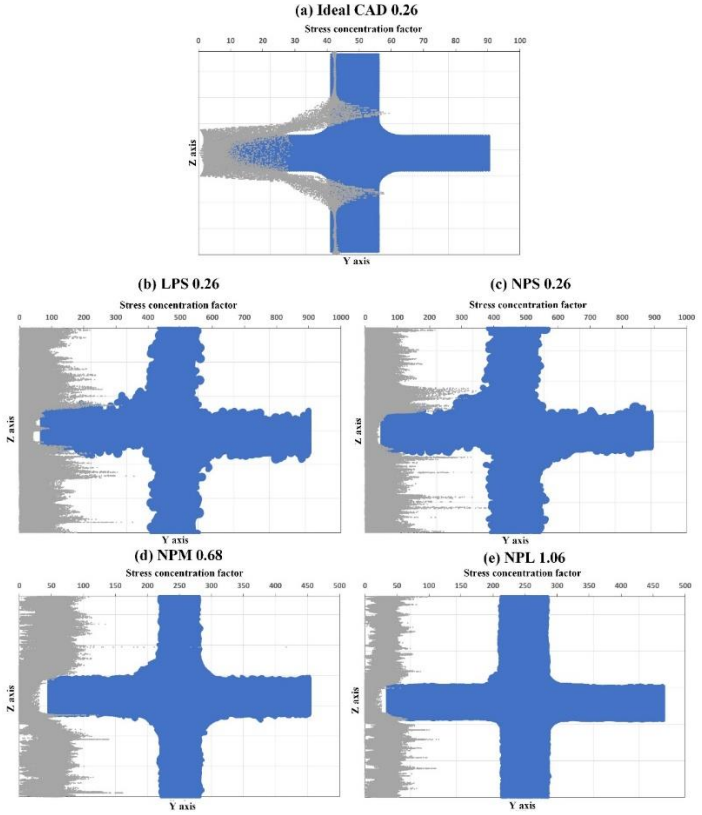

Figure 4-14. Statistical analysis of stress concentration factor distribution moving toward a) an ideal CAD 0.26 junction and the real L-BBF junctions of (b) LPS 0.26, (c) NPS 0.26, (d) NPM 0.68, and (e) NPL 1.06.

Table 4-2. Stress concentration factor investigated for various CAD and Micro-CT models.

Sample	K_t* CAD	K_t* Micro-CT
LPS 0.26	59	169.18 ± 25
NPS 0.26	59	130.17 ± 18
NPM 0.68	54	77.01 ± 5
NPL 1.06	63	75.68 ± 3

The SCF was calculated by normalizing the von Mises to the nominal stress acting on the vertical struts. For the ideal CAD geometry with a smooth surface, the SCF value drastically increases to 59 closes to the junction (Figure 4-14a). Comparing the SCF value of samples produced in the same size (LPS 0.26 and NPS 0.26), the SCF value was lower for the sample fabricated with the normal laser power (NPS 0.26). Increasing the cell size leads to the reduction of the SCF value to the 75.68 for the NPL 1.06 sample. The SCF reported in this study was slightly lower than SCF reported for convex fillets in our previous work (Dallago et al. 2019a). The as-built geometries are characterized by a remarkably higher (up to almost 3 times for LPS 0.26) SCF compared to the ideal CAD configuration. In addition, due to the presence of surface irregularities, the SCF value varies along the entire length of the strut and reaches a maximum value closer to the junction. The SCF was the highest at the junctions for smaller cell size specimens (Figure 4-14b and c) compared to larger cell size specimens (Figure 4-14d and e) due to the presence of sharp/incomplete fillets in the former ones. In the larger cell size specimens, the SCF was closer to the corresponding ideal CAD model thanks to an improved fabrication accuracy made possible by the larger dimensional scale. This is further confirmed by the node size measured by CT, approaching the design one for larger cell size. These values further highlight the stress distribution around the ntches in the actual geometries discussed previously.

From the above discussion, it is clear that geometrical imperfections and surface irregularities detrimentally impact on the stress field and that this negative effect is more pronounced for the smaller strut thickness and unit cell size (Figure 4-14d and e). The specimens manufactured using lower power, LPS 0.26 (Figure 4-14b) has slightly higher surface imperfection compared to NPS 0.26 (Figure 4-14c), as it is affected by critically stressed notch-like surface irregularities. These observations are fully consistent with the outcomes of the metallographic analyses, which attested that increasing the strut thickness results in better geometrical accuracy and lower surface irregularities. Looking at Table 4-2, it can be noted that the SCF in the as-built condition remains approximately constant for unit cell sizes comprised between 4 and 6 mm (viz. strut thickness comprised between 0.68 and 1.06 mm), being about 50% higher than that expected from the as-designed geometry. Conversely, if the cell size is reduced to 1.5 mm (strut thickness 0.26 mm), the SCF increases dramatically, up to almost 3 times the theoretical one. These findings confirm previous outcomes on cubic cellular structures made of Ti-6Al-4V (Dallago et al. 2021) and indicate the presence of a manufacturing threshold, below which the geometrical imperfections lead to unacceptably high stress concentration effects. For this reason, the mechanical characterization described in the next sections will be carried out on lattices employing cubic unit cells with 4 mm side, viz. the smallest unit cell size that proved to be manufactured with adequate geometrical accuracy.

4.2.4 Mechanical tests

A representative monotonic stress-strain curve of NPM 0.68 cellular structure is shown in Figure 4-15a. The curve can be divided into three regions, (i) linear elastic (ii) plateau, and (iii) densification. The curve is in good agreement with the typical stress-strain curve of a stretching dominated cellular material, predicted by Gibson – Ashby model (Gibson and Ashby 1997). However, depending on the base material properties and the cell topology, the regions of the curve (mainly yielding and plateau regions) change accordingly (Raghavendra, Molinari, Dallago, et al. 2021a; Yuan et al. 2018). In the current study, despite the good ductility of base material, a steep decrease in the stress is observed after yielding. This is probably due to the cubic cell topology, which consists of struts only in the loading direction, leading to a buckling/bending deformation of the loaded struts (Raghavendra et al. 2020). This is confirmed by the sample deformation in Figure 4-15c, where the vertical struts at the center of the specimen undergo a bending/buckling deformation after a strain value corresponding to the yield point. Beyond this point, the struts collapse horizontally without complete fracture, thanks to the high ductility β-Ti21S as-built material. To this regard, it can be noted that similar cubic lattices made of Ti-6Al-4V and tested in (Raghavendra et al. 2020) failed after compressive monotonic loading at 10% compression strain, thus much lower than that displayed by the present alloy. Further loading the specimen leads to an increase in the compressive stress as shown by the region beyond the densification of the stress-strain curve. This increase in stress is because the remaining unit cells tend to bear the load until a new layer undergoes yielding. For this specimen failure of a new layer was observed at the top of the specimen (Figure 4-15c), at a lower yield stress compared to the first peak observed in Figure 4-15a. Various studies have indicated such layer-by-layer failure for different cell topologies. Nevertheless, the type of cell topology also plays a major role in such failure and densification mechanism (Qiu et al. 2015; Ahmadi et al. 2015; Kadkhodapour et al. 2015).

The stress-strain curve recorded under cyclic loading-unloading condition for the specimen NPM 0.68 is shown in Figure 4-15b and the mechanical properties are tabulated in Table 4-3. The curve clearly indicates that the slope of the first loading cycle is lower than those of the following unloading and loading cycles. This is because of the local plasticization that occurs at locations like junctions and surface defects, leading to stabilization of the specimen (McKown et al. 2008; C. Yan et al. 2012). The stabilization is confirmed by the overlapping of the curve for the cycles following the first one.

Table 4-3. Mechanical properties of simple cubic lattice design 0.68-4 cell size, reported according to the ISO13314.

Maximum compressive stress (MPa)	16.59 ± 0.28
Yield stress of lattice design *(MPa)	15.47 ± 0.68
Quasi-elastic gradient (MPa)	1949
Elastic gradient (MPa)**	2038
Yield stress of base material (MPa)	709 ± 6
Normalized by yield stress	0.021

Compressive offset stress

****Elastic modulus***

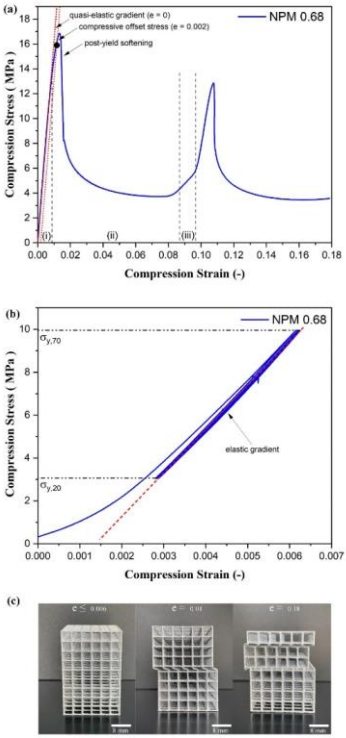

Figure 4-15. Monotonic stress-strain curve of β-Ti21S alloy in simple cubic geometry (a), the loading-unloading condition (b), and the appearance of tested sample in the linear elastic regime (e ≤ 0.006), post-yield stress (e ≈ 0.01), and densification (e ≈ 0.18) (c).

The results of compression – compression high cycle fatigue tests are plotted in Figure 4-16a. The data was fitted with the parameters listed on the Figure 4-16a and the standard deviation S as well calculated from the root square of estimated regression variance S^2. Figure 4-16b plots the SN data in terms of stress amplitude normalized to yield strength of the same lattice structure. It can be noted that the SN has a very low slope and that the normalized fatigue strength at 10^7 cycles is close to 0.8. A similar trend was found in (Raghavendra, Molinari, Cao, et al. 2021) for cubic lattices made of Ti-6Al-4V. This fatigue behavior can be attributed to the fact that the structure is stretching dominated and that the compressive load is almost completely borne by the struts orientated along the loading direction. In this way, the struts are subjected to compressive stresses only, which are known to be less critical in triggering the fatigue damage, even retarding the fatigue crack propagation stage (Amin Yavari et al. 2015).

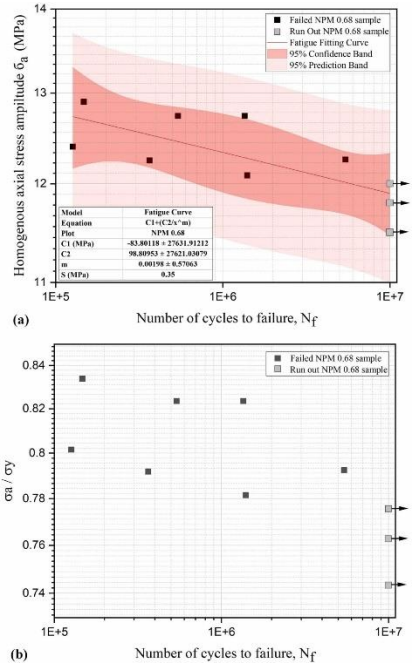

Figure 4-16. Stress vs number of cycles to failure for β-Ti21S simple cubic lattice material (a) and normalized fatigue strength with respect to the yield strength of static compression strength (b).

Figure 4-17 shows a typical cross section micrograph of a fatigued sample. In contrast to most of the fractographic analyses published in the literature on fatigued lattice materials in which the fatigue cracks preferentially nucleated in the vicinity of lattice nodes, it can be noted that in the present case the lattice specimen displays multiple crack initiation. In particular, cracks are found starting from surface imperfections located both in the filleted node but also along the struts far from the junctions. This means that the design of the filleted specimen and the choice of the unit cell size above the manufacturability threshold made in this work rendered the structure uniformly critical against the fatigue damage mechanism. It can be also observed that most of the cracks found on the strut nucleated preferentially from notch-like valleys rather than from satellite powder particles (affecting to a larger extent the downward face of the strut), thus confirming the FEM analyses that attested their less detrimental effect on the stress distribution. Moreover, an interesting observation can be made by observing the fatigue crack propagation behavior at higher magnification (Figure 4-18), i.e., the formation of persistent slip bands (characteristics of ductile materials under fatigue loading (Suresh 1998)) in the region surrounding cracks emanating from surface notches. A deeper study is needed to confirm the effect of these features on the fatigue behavior.

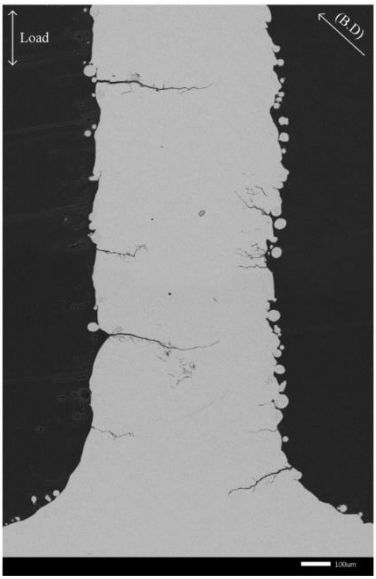

Figure 4-17. SEM cross section micrograph of the fatigue sample failed at 1.4 E + 5 cycles, showing the fatigue crack location with respect to the surface. imperfections.

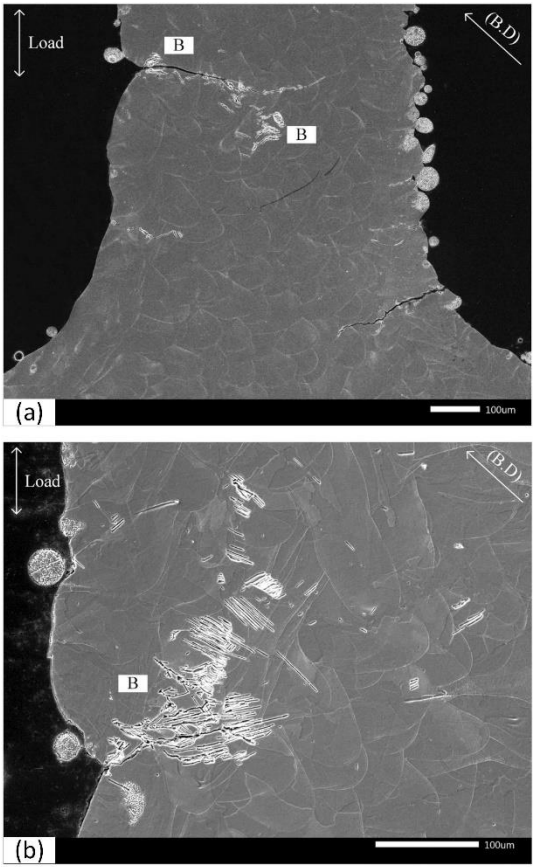

Figure 4-18. SEM cross section micrographs of the fatigue samples failed at 1.4 E + 5 cycles, showing the fatigue propagation behavior around the fatigue initiation sites, B refers to the lateral plane defects caused by varying-loading.

Part 2-2: Manufacturing of octet truss design

4.2.5 Microstructural analysis of the octet truss sample

The cross-section micrograph of the octet truss sample is shown in Figure 4-19. The printed octet truss lattices had nearly defect-free microstructure and the grains elongated toward the building direction are in the order of a few millimeters' length. The geometrical deviation was found to be similar to the simple cubic design, whose

structures followed the as-designed geometry in an appropriate accuracy. The effect of the outer contour applied to improve the surface quality is obvious. Dross formation was observed on the downward face skin of the unit cell, as shown by the arrow in Figure 4-19b. The central part of the unit cell had the thickness size of t_1=1360±106 µm and strut thickness of t_2=375±29 µm. Comparing the CAD dimensions (central part thickness = 1300 µm and strut thickness 540 µm) with the results of the 2D thickness measurement it es evident that the printed sample had lower thickness.

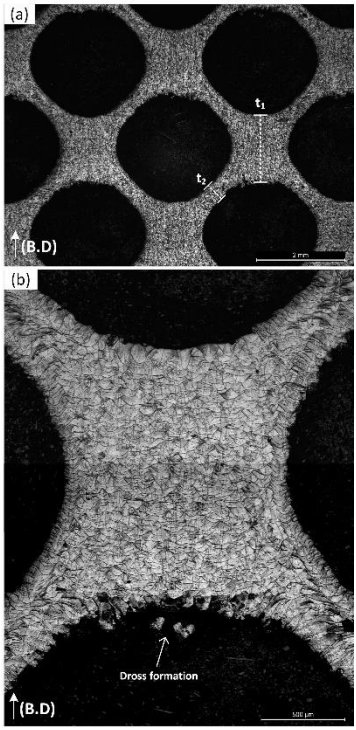

Figure 4-19. Cross section micrographs as-built octet truss cellular sample, t_x (x= 1 and 2) refers to the thickness of the middle part of cell and the arm part, respectively.

4.2.6 Mechanical properties

A representative monotonic stress-strain curve of the as-built octet truss sample design is shown in Figure 4-20a. The curve can be divided into two regions, a first (i) linear elastic, and a (ii) plateau one. The curve is in good agreement with the typical stress-strain curve of a bending dominated cellular material, predicted by Gibson – Ashby model (Gibson and Ashby 1997). This is clearly due to the octet truss cell

topology, which consists of struts vertical and angular to the loading direction, leading to a bending deformation of the loaded struts. This is further confirmed by Figure 4-20c, where the component undergoes a bending deformation beyond a strain value corresponding to the yield point. The similar trend was reported by (Arabnejad et al. 2016) for the Ti-6Al-4V alloy, showing a much lower ductility than present β-Ti21S alloy. This shows that the unit cell topology has persuasive influence on the mechanical behavior of lattice material regardless of the material used for printing.

The stress-strain curve in the loading-unloading condition for the component is shown in Figure 4-20b and the mechanical properties attained from the compression tests are listed in Table 4-4. The slope of unloading curve clearly implies the stable linear condition opposing to the non-linear slope of the first loading, mainly caused by the local plasticization.

Table 4-4. Mechanical properties of octet truss lattice design 0.54-4 cell size , reported according to the ISO13314.

Maximum compressive stress (MPa)	67.4 ± 0.51
Yield stress of lattice design *(MPa)	50.91 ± 0.88
Quasi-elastic gradient (MPa)	2915 ± 275
Elastic gradient (MPa)**	3555 ± 100
Yield stress of base material (MPa)	709 ± 6
Normalized yield stress	0.073
Plateau compressive stress (MPa)	61.97 ± 0.76

Compressive offset stress

****Elastic modulus***

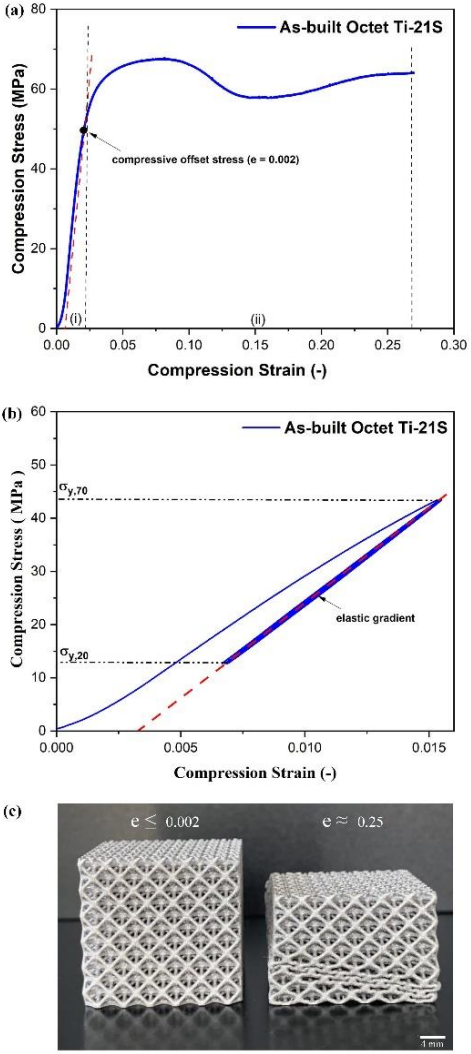

Figure 4-20. Monotonic stress-strain curve of β-Ti21S alloy in a octet truss geometry (a), the loading-unloading condition (b), and the appearance of tested sample in the linear elastic regime (e ≤ 0.002), and densification (e ≈ 0.25) (c).

Important considerations can be drawn from Figure 4-21a and b, where the quasi-elastic gradient and the maximum compressive strength of simple cubic and octet truss designs are plotted together with a collection of experimental data published in the literature as a function of the relative density (Benedetti et al. 2021). The data of the present work lie in the upper band of the diagram and are in much better agreement with the trends predicted by Ashby and Gibson (Gibson and Ashby 1997) for stretch-dominated lattice materials in the case of simple cubic design (*) and bending dominated lattice materials in the case of octet truss design (#), especially in the case of the quasi-elastic gradient. This improvement can be ascribed to the adequate manufacturing accuracy of L-PBF specimens, limiting a lot the spurious bending effects introduced by manufacturing imperfections (like strut misalignments and waviness), which in contrast affect most of the ideal stretching-dominated lattices tested in the literature, making their mechanical behavior essentially bending-dominated.

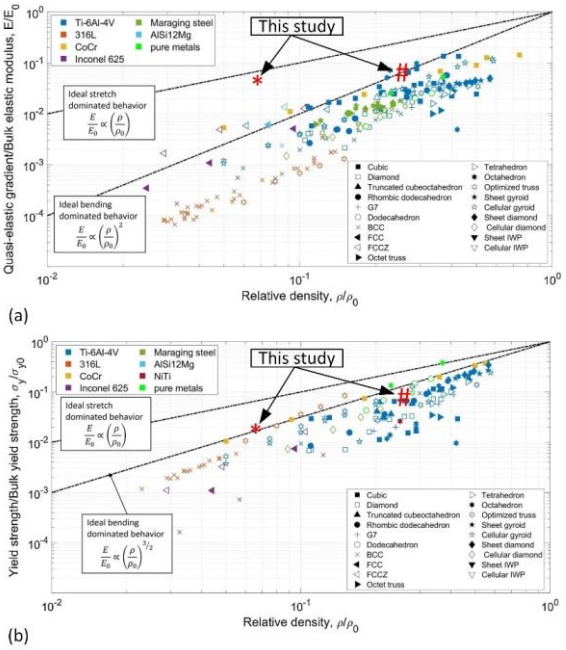

Figure 4-21. Relative quasi-static elastic gradient (a) and relative yield strength (b) as a function of relative density for cellular lattice materials investigated in the literature (Benedetti et al. 2021) **with various unit cell architecture. The star and hashtag refer to the simple cubic and octet truss designs in this study, respectively.**

The results of compression – compression high cycle fatigue tests are plotted in Figure 4-22a. The data was fitted with the parameters listed within the Figure 4-22a and the standard deviation S as well calculated from the root square of estimated regression variance S^2. It is clear that the SN data has the Knee around the 10 E+6 cycles, showing that the fatigue resistance for this topology is around 6MPa. Figure 4-22b plots the SN data in terms of stress amplitude normalized to yield strength of the same lattice structure. The normalized fatigue strength at 10^7 cycles is close to 0.1. This low value could be associated to the fact that, unlike simple cubic cell, in this cell topology no strut is oriented along the loading direction, i.e., the most favorable direction in retarding fatigue failure (Amin Yavari et al. 2015).

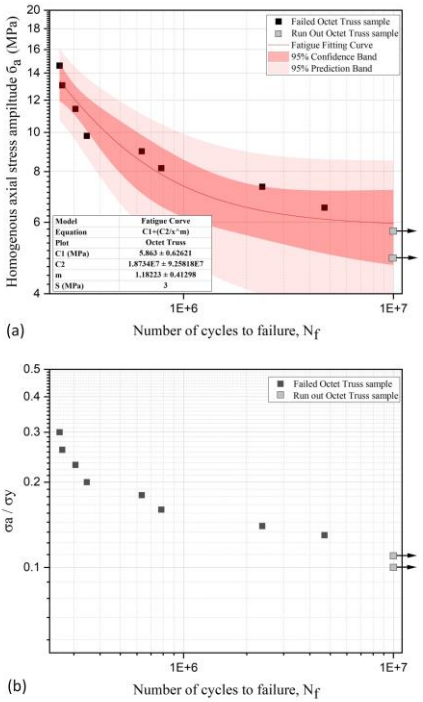

Figure 4-22. Stress vs number of cycles to failure for β-Ti21S octet truss lattice material (a) and normalized fatigue strength with respect to the yield strength of static compression strength (b).

Table 1-6 compares the mechanical properties of the cancellous bone with the results of this study. This comparison indicates that the mechanical properties of lattice Ti-21S alloy could get close to those values for the bones.

Table 4-5. Comparison of the mechanical properties of cancellous bone and L-PBF processed lattices Ti-21S alloy (Lindahl 1976; Burstein, Reilly, and Martens 1976; Sevilla et al. 2007; Luo et al. 2019)**.**

	$\sigma_{y0.2}$ (Mpa)	σ_{emax} (Mpa)	E (Gpa)	Porosity (%)
Cancellous bone	15.2 ± 8	25 ± 8.1	1.08 ± 0.86	65-75
Simple cubic	15.47 ± 0.68	16.59 ± 0.28	2.03 ± 0.56	93
Octet truss	50.91 ± 0.88	67.4 ± 0.51	3.5 ± 1.0	73

$\sigma_{y0.2}$: 0.2% yield compression stress; E : elastic modulus; σ_{emax}: fatigue strength limit.

4.3 Conclusion of part 2

The manufacturability of lattice structures fabricated by laser powder bed fusion using a novel β-Ti alloy was investigated. The as-built β-Ti21S alloy has a remarkably lower elastic modulus and higher fracture elongation than Ti-6Al-4V, while maintaining acceptably high values of yield stress and ultimate tensile strength. To evaluate the printability of cellular structures using this material, metrological and metallurgical investigations were carried out on small specimens consisting of a 3x3x3 arrangement of regular cubic cells. Three different unit cell sizes were investigated, whose parameters were adjusted to achieve a theoretical elastic modulus along the cube side direction of about 1 GPa and an open porosity of 93%. The influence of process parameters, namely laser energy was evaluated. The main results can be summarized in the following points:

- Suitable manufacturing quality is obtained for strut thickness above 0.5 mm.
- FE modeling highlighted that geometrical imperfections and surface irregularities detrimentally impact on the local stress field and that this negative effect is more pronounced at smaller strut thickness and unit cell size.
- The quasi-elastic gradient and the maximum compressive strength measured by compression tests, place the present cellular structures among the best stretching dominated cellular lattice materials investigated to date in the literature.
- The S-N curve resulting from compression – compression high cycle fatigue tests showed a normalized fatigue strength at 10^7 cycles of close

to 0.8, similar to cubic lattices made of Ti-6Al-4V, and higher than most cellular structures in the literature.

After finding the manufacturable cell size, the more intricate lattice structure, octet truss, was fabricated. The microstructural analysis of the components showed the same good manufacturability response observed for the manufacturable 4 mm cubic cell size. The mechanical behavior was in agreement with the Gibson-Ashby model for bending-dominated mechanism. The elastic modulus of 3 GPa was estimated from the unloading slope of the stress-strain curve. The mechanical properties of octet truss design were similar to those values for the bone structure, showing the promising potential of using this alloy for the biomedical implants.

The present results of simple cubic and octet truss designs can be the base for more studies of lattice structure of Ti-21S alloy in the future.

4.4 References

Abu-Amer, Yousef, Isra Darwech, and John C Clohisy. 2007. "Aseptic Loosening of Total Joint Replacements: Mechanisms Underlying Osteolysis and Potential Therapies." *Arthritis Research & Therapy* 9 (1): S6. https://doi.org/10.1186/ar2170.

Afkhami, Shahriar, Edris Dabiri, Kalle Lipiäinen, Heidi Piili, and Timo Björk. 2021. "Effects of Notch-Load Interactions on the Mechanical Performance of 3D Printed Tool Steel 18Ni300." *Additive Manufacturing* 47 (November): 102260. https://doi.org/10.1016/J.ADDMA.2021.102260.

Agarwal, N, A Bhattacharjee, P Ghosal, T K Nandy, and P K Sagar. 2008. "Heat Treatment, Microstructure and Mechanical Properties of a Metastable β Titanium Alloy Timetal® 21s." *Transactions of the Indian Institute of Metals* 61 (5): 419–25. https://doi.org/10.1007/s12666-008-0074-6.

Ahmadi, Seyed, Saber Yavari, Ruebn Wauthle, Behdad Pouran, Jan Schrooten, Harrie Weinans, and Amir Zadpoor. 2015. "Additively Manufactured Open-Cell Porous Biomaterials Made from Six Different Space-Filling Unit Cells: The Mechanical and Morphological Properties." *Materials* 8 (4): 1871–96. https://doi.org/10.3390/ma8041871.

Ahmed, T., and H. J. Rack. 1998a. "Phase Transformations during Cooling in A+β Titanium Alloys." *Materials Science and Engineering: A* 243 (1–2): 206–11. https://doi.org/10.1016/S0921-5093(97)00802-2.

Ahmed, T., and H.J. Rack. 1998b. "Phase Transformations during Cooling in A+β Titanium Alloys." *Materials Science and Engineering: A* 243 (1–2): 206–11. https://doi.org/10.1016/S0921-5093(97)00802-2.

Amin Yavari, S., S. M. Ahmadi, R. Wauthle, B. Pouran, J. Schrooten, H. Weinans, and A. A. Zadpoor. 2015. "Relationship between Unit Cell Type and Porosity and the Fatigue Behavior of Selective Laser Melted Meta-Biomaterials." *Journal of the Mechanical Behavior of Biomedical Materials* 43: 91–100. https://doi.org/10.1016/j.jmbbm.2014.12.015.

Arabnejad, Sajad, R. Burnett Johnston, Jenny Ann Pura, Baljinder Singh, Michael Tanzer, and Damiano Pasini. 2016. "High-Strength Porous Biomaterials for Bone Replacement: A Strategy to Assess the Interplay between Cell Morphology, Mechanical Properties, Bone Ingrowth and Manufacturing Constraints." *Acta Biomaterialia* 30 (January): 345–56. https://doi.org/10.1016/J.ACTBIO.2015.10.048.

Bari, Klaudio, and Arun Arjunan. 2019. "Extra Low Interstitial Titanium Based Fully Porous Morphological Bone Scaffolds Manufactured Using Selective Laser Melting." *Journal of the Mechanical Behavior of Biomedical Materials* 95 (July): 1–12. https://doi.org/https://doi.org/10.1016/j.jmbbm.2019.03.025.

Benedetti, M., V. Fontanari, G. Lütjering, and J. Albrecht. 2008. "The Effect of Notch Plasticity on the Behaviour of Fatigue Cracks Emanating from Edge-Notches in High-Strength β-Titanium Alloys." *Engineering Fracture Mechanics* 75 (2): 169–87. https://doi.org/10.1016/J.ENGFRACMECH.2007.03.037.

Benedetti, M., A. du Plessis, R.O. Ritchie, M. Dallago, S.M.J. Razavi, and F. Berto. 2021. "Architected Cellular Materials: A Review on Their Mechanical Properties towards Fatigue-Tolerant Design and Fabrication." *Materials Science and Engineering: R: Reports* 144 (April): 100606. https://doi.org/10.1016/j.mser.2021.100606.

Benedetti, M., E. Torresani, M. Leoni, V. Fontanari, M. Bandini, C. Pederzolli, and C. Potrich. 2017. "The Effect of Post-Sintering Treatments on the Fatigue and Biological Behavior of Ti-6Al-4V ELI Parts Made by Selective Laser Melting." *Journal of the Mechanical Behavior of Biomedical Materials* 71 (July): 295–306. https://doi.org/10.1016/J.JMBBM.2017.03.024.

Borenfreund, Ellen, and James A. Puerner. 1985. "Toxicity Determined in Vitro by Morphological Alterations and Neutral Red Absorption." *Toxicology Letters* 24 (2–3): 119–24. https://doi.org/10.1016/0378-4274(85)90046-3.

Burstein, A H, D T Reilly, and M Martens. 1976. "Aging of Bone Tissue: Mechanical Properties." *JBJS* 58 (1). https://journals.lww.com/jbjsjournal/Fulltext/1976/58010/Aging_of_bone_tissue__mechanical_properties.15.aspx.

Carroll, Beth E., Todd A. Palmer, and Allison M. Beese. 2015. “Anisotropic Tensile Behavior of Ti–6Al–4V Components Fabricated with Directed Energy Deposition Additive Manufacturing.” *Acta Materialia* 87 (April): 309–20. https://doi.org/10.1016/J.ACTAMAT.2014.12.054.

Chen, L. Y., J. C. Huang, C. H. Lin, C. T. Pan, S. Y. Chen, T. L. Yang, D. Y. Lin, H. K. Lin, and J. S.C. Jang. 2017. “Anisotropic Response of Ti-6Al-4V Alloy Fabricated by 3D Printing Selective Laser Melting.” *Materials Science and Engineering: A* 682 (January): 389–95. https://doi.org/10.1016/J.MSEA.2016.11.061.

Collings, E.W. 1988. *Physical Metallurgy of Titanium Alloys*. https://inis.iaea.org/search/search.aspx?orig_q=RN:20059516.

Dallago, M., V. Fontanari, E. Torresani, M. Leoni, C. Pederzolli, C. Potrich, and M. Benedetti. 2018. “Fatigue and Biological Properties of Ti-6Al-4V ELI Cellular Structures with Variously Arranged Cubic Cells Made by Selective Laser Melting.” *Journal of the Mechanical Behavior of Biomedical Materials* 78 (October 2017): 381–94. https://doi.org/10.1016/j.jmbbm.2017.11.044.

Dallago, M., S. Raghavendra, V. Luchin, G. Zappini, D. Pasini, and M. Benedetti. 2021. “The Role of Node Fillet, Unit-Cell Size and Strut Orientation on the Fatigue Strength of Ti-6Al-4V Lattice Materials Additively Manufactured via Laser Powder Bed Fusion.” *International Journal of Fatigue* 142 (January): 105946. https://doi.org/10.1016/j.ijfatigue.2020.105946.

Dallago, M., B. Winiarski, F. Zanini, S. Carmignato, and M. Benedetti. 2019a. “On the Effect of Geometrical Imperfections and Defects on the Fatigue Strength of Cellular Lattice Structures Additively Manufactured via Selective Laser Melting.” *International Journal of Fatigue* 124 (November 2018): 348–60. https://doi.org/10.1016/j.ijfatigue.2019.03.019.

———. 2019b. “On the Effect of Geometrical Imperfections and Defects on the Fatigue Strength of Cellular Lattice Structures Additively Manufactured via Selective Laser Melting.” *International Journal of Fatigue* 124 (July): 348–60. https://doi.org/10.1016/J.IJFATIGUE.2019.03.019.

———. 2019c. “On the Effect of Geometrical Imperfections and Defects on the Fatigue Strength of Cellular Lattice Structures Additively Manufactured via Selective Laser Melting.” *International Journal of Fatigue* 124 (July): 348–60. https://doi.org/10.1016/J.IJFATIGUE.2019.03.019.

DebRoy, T., H. L. Wei, J. S. Zuback, T. Mukherjee, J. W. Elmer, J. O. Milewski, A. M. Beese, A. Wilson-Heid, A. De, and W. Zhang. 2018. “Additive

Manufacturing of Metallic Components – Process, Structure and Properties." *Progress in Materials Science* 92 (March): 112–224. https://doi.org/10.1016/J.PMATSCI.2017.10.001.

Facchini, Luca, Emanuele Magalini, Pierfrancesco Robotti, Alberto Molinari, Simon Höges, and Konrad Wissenbach. 2010. "Ductility of a Ti-6Al-4V Alloy Produced by Selective Laser Melting of Prealloyed Powders." *Rapid Prototyping Journal* 16 (6): 450–59. https://doi.org/10.1108/13552541011083371.

Fischer, M., D. Joguet, G. Robin, L. Peltier, and P. Laheurte. 2016. "In Situ Elaboration of a Binary Ti–26Nb Alloy by Selective Laser Melting of Elemental Titanium and Niobium Mixed Powders." *Materials Science and Engineering: C* 62 (May): 852–59. https://doi.org/10.1016/J.MSEC.2016.02.033.

Fotovvati, Behzad, Navid Namdari, and Amir Dehghanghadikolaei. 2018. "Fatigue Performance of Selective Laser Melted Ti6Al4V Components: State of the Art." *Materials Research Express* 6 (1): 012002. https://doi.org/10.1088/2053-1591/aae10e.

Gibson, Lorna J., and Michael F. Ashby. 1997. *Cellular Solids*. Cambridge University Press. https://doi.org/10.1017/CBO9781139878326.

Gross, Bethany C, Jayda L Erkal, Sarah Y Lockwood, Chengpeng Chen, and Dana M Spence. 2014. "Evaluation of 3D Printing and Its Potential Impact on Biotechnology and the Chemical Sciences." *Analytical Chemistry* 86 (7): 3240–53. https://doi.org/10.1021/ac403397r.

Hitzler, Leonhard, Johann Hirsch, Burkhard Heine, Markus Merkel, Wayne Hall, and Andreas Öchsner. 2017. "On the Anisotropic Mechanical Properties of Selective Laser-Melted Stainless Steel." *Materials* 10 (10). https://doi.org/10.3390/ma10101136.

Ho, W. F., C. P. Ju, and J. H. Chern Lin. 1999. "Structure and Properties of Cast Binary Ti–Mo Alloys." *Biomaterials* 20 (22): 2115–22. https://doi.org/10.1016/S0142-9612(99)00114-3.

HUISKES, R I K, HARRIE WEINANS, and BERT V A N RIETBERGEN. 1992. "The Relationship Between Stress Shielding and Bone Resorption Around Total Hip Stems and the Effects of Flexible Materials." *Clinical Orthopaedics and Related Research®* 274: 124–34. https://journals.lww.com/clinorthop/Fulltext/1992/01000/The_Relationship_Between_Stress_Shielding_and_Bone.14.aspx.

Ishimoto, Takuya, Koji Hagihara, Kenta Hisamoto, Shi-Hai Sun, and Takayoshi

Nakano. 2017. “Crystallographic Texture Control of Beta-Type Ti–15Mo–5Zr–3Al Alloy by Selective Laser Melting for the Development of Novel Implants with a Biocompatible Low Young’s Modulus.” *Scripta Materialia* 132: 34–38. https://doi.org/https://doi.org/10.1016/j.scriptamat.2016.12.038.

Kadkhodapour, J., H. Montazerian, A.Ch. Darabi, A.P. Anaraki, S.M. Ahmadi, A.A. Zadpoor, and S. Schmauder. 2015. “Failure Mechanisms of Additively Manufactured Porous Biomaterials: Effects of Porosity and Type of Unit Cell.” *Journal of the Mechanical Behavior of Biomedical Materials* 50 (October): 180–91. https://doi.org/10.1016/j.jmbbm.2015.06.012.

Kang, Nan, Yunlong Li, Xin Lin, Enhao Feng, and Weidong Huang. 2019. “Microstructure and Tensile Properties of Ti-Mo Alloys Manufactured via Using Laser Powder Bed Fusion.” *Journal of Alloys and Compounds* 771 (January): 877–84. https://doi.org/10.1016/J.JALLCOM.2018.09.008.

Kang, Nan, Xin Lin, Christian Coddet, Xiaoli Wen, and Weidong Huang. 2020. “Selective Laser Melting of Low Modulus Ti-Mo Alloy: α/β Heterogeneous Conchoidal Structure.” *Materials Letters* 267 (May): 127544. https://doi.org/10.1016/J.MATLET.2020.127544.

Khorasani, Amir Mahyar, Moshe Goldberg, Egan H Doeven, and Guy Littlefair. 2015. “Titanium in Biomedical Applications-Properties and Fabrication: A Review.” *Journal of Biomaterials and Tissue Engineering* 5 (8): 593–619. https://www.ingentaconnect.com/content/asp/jbte/2015/00000005/00000008/art00001.

Kumar, S. S.Satheesh, B. Pavithra, Vajinder Singh, P. Ghosal, and T. Raghu. 2019. “Tensile Anisotropy Associated Microstructural and Microtextural Evolution in a Metastable Beta Titanium Alloy.” *Materials Science and Engineering: A* 747 (February): 1–16. https://doi.org/10.1016/J.MSEA.2019.01.053.

Leary, Martin, Mahyar Khorasani, Avik Sarker, Johnathan Tran, Kate Fox, David Downing, and Anton du Plessis. 2021. “Surface Roughness.” *Fundamentals of Laser Powder Bed Fusion of Metals*, January, 179–213. https://doi.org/10.1016/B978-0-12-824090-8.00023-8.

Lee, Seungjong, Behnam Rasoolian, Daniel F. Silva, Jonathan W. Pegues, and Nima Shamsaei. 2021. “Surface Roughness Parameter and Modeling for Fatigue Behavior of Additive Manufactured Parts: A Non-Destructive Data-Driven Approach.” *Additive Manufacturing* 46 (October): 102094. https://doi.org/10.1016/J.ADDMA.2021.102094.

Li, Peipei, Derek Warner, Ali Fatemi, and Nam D Phan. n.d. “On the Fatigue Performance of Additively Manufactured Ti-6Al-4V to Enable Rapid Qualification for Aerospace Applications.” In *57th AIAA/ASCE/AHS/ASC Structures, Structural Dynamics, and Materials Conference*. https://doi.org/10.2514/6.2016-1656.

Lindahl, Olov. 1976. “Mechanical Properties of Dried Defatted Spongy Bone.” *Acta Orthopaedica Scandinavica* 47 (1): 11–19. https://doi.org/10.3109/17453677608998966.

Liu, Lu, Paul Kamm, Francisco García-Moreno, John Banhart, and Damiano Pasini. 2017. “Elastic and Failure Response of Imperfect Three-Dimensional Metallic Lattices: The Role of Geometric Defects Induced by Selective Laser Melting.” *Journal of the Mechanics and Physics of Solids* 107: 160–84. https://doi.org/10.1016/j.jmps.2017.07.003.

Liu, Y. J., X. P. Li, L. C. Zhang, and T. B. Sercombe. 2015. “Processing and Properties of Topologically Optimised Biomedical Ti–24Nb–4Zr–8Sn Scaffolds Manufactured by Selective Laser Melting.” *Materials Science and Engineering: A* 642 (August): 268–78. https://doi.org/10.1016/J.MSEA.2015.06.088.

Liu, Y. J., H. L. Wang, S. J. Li, S. G. Wang, W. J. Wang, W. T. Hou, Y. L. Hao, R. Yang, and L. C. Zhang. 2017a. “Compressive and Fatigue Behavior of Beta-Type Titanium Porous Structures Fabricated by Electron Beam Melting.” *Acta Materialia* 126 (March): 58–66. https://doi.org/10.1016/J.ACTAMAT.2016.12.052.

———. 2017b. “Compressive and Fatigue Behavior of Beta-Type Titanium Porous Structures Fabricated by Electron Beam Melting.” *Acta Materialia* 126 (March): 58–66. https://doi.org/https://doi.org/10.1016/j.actamat.2016.12.052.

Liu, Z, and G Welsch. 1988. “Effects of Oxygen and Heat Treatment on the Mechanical Properties of Alpha and Beta Titanium Alloys.” *Metallurgical Transactions A* 19 (3): 527–42. https://doi.org/10.1007/BF02649267.

Lozanovski, Bill, David Downing, Rance Tino, Anton du Plessis, Phuong Tran, John Jakeman, Darpan Shidid, et al. 2020. “Non-Destructive Simulation of Node Defects in Additively Manufactured Lattice Structures.” *Additive Manufacturing* 36 (December): 101593. https://doi.org/10.1016/J.ADDMA.2020.101593.

Lozanovski, Bill, Martin Leary, Phuong Tran, Darpan Shidid, Ma Qian, Peter Choong, and Milan Brandt. 2019. “Computational Modelling of Strut Defects in SLM

Manufactured Lattice Structures." *Materials and Design* 171: 107671. https://doi.org/10.1016/j.matdes.2019.107671.

Luo, J. P., Y. J. Huang, J. Y. Xu, J. F. Sun, M. S. Dargusch, C. H. Hou, L. Ren, R. Z. Wang, T. Ebel, and M. Yan. 2020. "Additively Manufactured Biomedical Ti-Nb-Ta-Zr Lattices with Tunable Young's Modulus: Mechanical Property, Biocompatibility, and Proteomics Analysis." *Materials Science and Engineering: C* 114 (September): 110903. https://doi.org/10.1016/J.MSEC.2020.110903.

Luo, J. P., J. F. Sun, Y. J. Huang, J. H. Zhang, D. P. Zhao, M. Yan, and Y. D. Zhang. 2019. "Low-Modulus Biomedical Ti–30Nb–5Ta–3Zr Additively Manufactured by Selective Laser Melting and Its Biocompatibility." *Materials Science and Engineering: C* 97 (April): 275–84. https://doi.org/10.1016/J.MSEC.2018.11.077.

Lütjering, Gerd, and James C Williams. 2007. "Beta Alloys." In *Titanium*, 283–336. Berlin, Heidelberg: Springer Berlin Heidelberg. https://doi.org/10.1007/978-3-540-73036-1_7.

Maleki, Erfan, Sara Bagherifard, Michele Bandini, and Mario Guagliano. 2021. "Surface Post-Treatments for Metal Additive Manufacturing: Progress, Challenges, and Opportunities." *Additive Manufacturing* 37 (January): 101619. https://doi.org/10.1016/J.ADDMA.2020.101619.

McKown, S., Y. Shen, W.K. Brookes, C.J. Sutcliffe, W.J. Cantwell, G.S. Langdon, G.N. Nurick, and M.D. Theobald. 2008. "The Quasi-Static and Blast Loading Response of Lattice Structures." *International Journal of Impact Engineering* 35 (8): 795–810. https://doi.org/10.1016/j.ijimpeng.2007.10.005.

Mei, Ying, Christopher Cannizzaro, Hyoungshin Park, Qiaobing Xu, Said R Bogatyrev, Kevin Yi, Nathan Goldman, Robert Langer, and Daniel G Anderson. 2008. "Cell-Compatible, Multicomponent Protein Arrays with Subcellular Feature Resolution." *Small* 4 (10): 1600–1604. https://doi.org/https://doi.org/10.1002/smll.200800363.

Moussa, Ahmed, David Melancon, Asma el Elmi, and Damiano Pasini. 2021. "Topology Optimization of Imperfect Lattice Materials Built with Process-Induced Defects via Powder Bed Fusion." *Additive Manufacturing* 37 (January): 101608. https://doi.org/10.1016/J.ADDMA.2020.101608.

Murchio, Simone, Michele Dallago, Andrea Rigatti, Valerio Luchin, Filippo. Berto, Devid Maniglio, and Matteo Benedetti. n.d. "On the Effect of the Node and Building Orientation on the Fatigue Behavior of L-PBF Ti6Al4V Lattice

Structure Sub-Unital Elements." *Material Design \& Processing Communications* n/a (n/a): e258. https://doi.org/https://doi.org/10.1002/mdp2.258.

Ni, J., H. Ling, S. Zhang, Z. Wang, Z. Peng, C. Benyshek, R. Zan, et al. 2019. "Three-Dimensional Printing of Metals for Biomedical Applications." *Materials Today Bio* 3 (June): 100024. https://doi.org/10.1016/J.MTBIO.2019.100024.

Niinomi, Mitsuo. 1998a. "Mechanical Properties of Biomedical Titanium Alloys." *Materials Science and Engineering: A* 243 (1–2): 231–36. https://doi.org/10.1016/S0921-5093(97)00806-X.

———. 1998b. "Mechanical Properties of Biomedical Titanium Alloys." *Materials Science and Engineering: A* 243 (1–2): 231–36. https://doi.org/10.1016/S0921-5093(97)00806-X.

———. 2003. "Fatigue Performance and Cyto-Toxicity of Low Rigidity Titanium Alloy, Ti–29Nb–13Ta–4.6Zr." *Biomaterials* 24 (16): 2673–83. https://doi.org/10.1016/S0142-9612(03)00069-3.

Niinomi, Mitsuo, Masaaki Nakai, and Junko Hieda. 2012. "Development of New Metallic Alloys for Biomedical Applications." *Acta Biomaterialia* 8 (11): 3888–3903. https://doi.org/10.1016/J.ACTBIO.2012.06.037.

Parthasarathy, Jayanthi, Binil Starly, Shivakumar Raman, and Andy Christensen. 2010. "Mechanical Evaluation of Porous Titanium (Ti6Al4V) Structures with Electron Beam Melting (EBM)." *Journal of the Mechanical Behavior of Biomedical Materials* 3 (3): 249–59. https://doi.org/10.1016/J.JMBBM.2009.10.006.

Pellizzari, Massimo, Alireza Jam, Matilde Tschon, Milena Fini, Carlo Lora, and Matteo Benedetti. 2020. "A 3D-Printed Ultra-Low Young's Modulus β-Ti Alloy for Biomedical Applications." *Materials* 13 (12). https://doi.org/10.3390/ma13122792.

Peters, J O, and G Lütjering. 2001. "Comparison of the Fatigue and Fracture of A+β and β Titanium Alloys." *Metallurgical and Materials Transactions A* 32 (11): 2805–18. https://doi.org/10.1007/s11661-001-1031-8.

Plessis, Anton du. 2021. "Porosity in Laser Powder Bed Fusion." *Fundamentals of Laser Powder Bed Fusion of Metals*, January, 155–78. https://doi.org/10.1016/B978-0-12-824090-8.00007-X.

Plessis, Anton du, and Stephan G. le Roux. 2018. "Standardized X-Ray Tomography Testing of Additively Manufactured Parts: A Round Robin Test." *Additive*

Manufacturing 24 (December): 125–36. https://doi.org/10.1016/J.ADDMA.2018.09.014.

Plessis, Anton du, Igor Yadroitsev, Ina Yadroitsava, and Stephan G le Roux. 2018. "X-Ray Microcomputed Tomography in Additive Manufacturing: A Review of the Current Technology and Applications." *3D Printing and Additive Manufacturing* 5 (3): 227–47. https://doi.org/10.1089/3dp.2018.0060.

Porter, DA, and K. E Easterling. 2009. *Phase Transformations in Metals and Alloys.* https://doi.org/https://doi.org/10.1201/9781439883570.

Qiu, Chunlei, Sheng Yue, Nicholas J.E. Adkins, Mark Ward, Hany Hassanin, Peter D. Lee, Philip J. Withers, and Moataz M. Attallah. 2015. "Influence of Processing Conditions on Strut Structure and Compressive Properties of Cellular Lattice Structures Fabricated by Selective Laser Melting." *Materials Science and Engineering: A* 628 (March): 188–97. https://doi.org/10.1016/j.msea.2015.01.031.

Raghavendra, Sunil, Alberto Molinari, Anni Cao, Chao Gao, Filippo Berto, Gianluca Zappini, and Matteo Benedetti. 2021. "Quasi-static Compression and Compression–Compression Fatigue Behavior of Regular and Irregular Cellular Biomaterials." *Fatigue & Fracture of Engineering Materials & Structures* 44 (5): 1178–94. https://doi.org/10.1111/ffe.13422.

Raghavendra, Sunil, Alberto Molinari, Michele Dallago, Gianluca Zappini, Filippo Zanini, Simone Carmignato, and Matteo Benedetti. 2021a. "Uniaxial Static Mechanical Properties of Regular, Irregular and Random Additively Manufactured Cellular Materials: Nominal vs. Real Geometry." *Forces in Mechanics* 2 (July): 100007. https://doi.org/10.1016/j.finmec.2020.100007.

———. 2021b. "Uniaxial Static Mechanical Properties of Regular, Irregular and Random Additively Manufactured Cellular Materials: Nominal vs. Real Geometry." *Forces in Mechanics* 2 (July): 100007. https://doi.org/10.1016/J.FINMEC.2020.100007.

Raghavendra, Sunil, Alberto Molinari, Vigilio Fontanari, Michele Dallago, Valerio Luchin, Gianluca Zappini, and Matteo Benedetti. 2020. "Tension-Compression Asymmetric Mechanical Behaviour of Lattice Cellular Structures Produced by Selective Laser Melting." *Proceedings of the Institution of Mechanical Engineers, Part C: Journal of Mechanical Engineering Science* 234 (16): 3241–56. https://doi.org/10.1177/0954406220912786.

Rehme, Olaf, and Claus Emmelmann. 2006. "Rapid Manufacturing of Lattice

Structures with Selective Laser Melting." In *Laser-Based Micropackaging*, edited by Friedrich G Bachmann, Willem Hoving, Yongfeng Lu, and Kunihiko Washio, 6107:192–203. Society of Photo-Optical Instrumentation Engineers (SPIE) Conference Series. https://doi.org/10.1117/12.645848.

Ren, Dechun, Shujun Li, Hao Wang, Wentao Hou, Yulin Hao, Wei Jin, Rui Yang, R. Devesh K. Misra, and Lawrence E. Murr. 2019. "Fatigue Behavior of Ti-6Al-4V Cellular Structures Fabricated by Additive Manufacturing Technique." *Journal of Materials Science and Technology* 35 (2): 285–94. https://doi.org/10.1016/j.jmst.2018.09.066.

Ryan, Garrett, Abhay Pandit, and Dimitrios Panagiotis Apatsidis. 2006. "Fabrication Methods of Porous Metals for Use in Orthopaedic Applications." *Biomaterials* 27 (13): 2651–70. https://doi.org/10.1016/J.BIOMATERIALS.2005.12.002.

Sansoz, F, M Almesallmy, and H Ghonem. 2004. "Ductility Exhaustion Mechanisms in Thermally Exposed Thin Sheets of a Near-β Titanium Alloy." *Metallurgical and Materials Transactions A* 35 (10): 3113–27. https://doi.org/10.1007/s11661-004-0056-1.

Schwab, H., F. Palm, U. Kühn, and J. Eckert. 2016. "Microstructure and Mechanical Properties of the Near-Beta Titanium Alloy Ti-5553 Processed by Selective Laser Melting." *Materials & Design* 105 (September): 75–80. https://doi.org/10.1016/J.MATDES.2016.04.103.

Schwab, Holger, Konda Gokuldoss Prashanth, Lukas Löber, Uta Kühn, and Jürgen Eckert. 2015. "Selective Laser Melting of Ti-45Nb Alloy." *Metals* 5 (2): 686–94. https://doi.org/10.3390/met5020686.

Seiler, Philipp E, Kan Li, Vikram S Deshpande, and Norman A Fleck. 2020. "The Influence of Strut Waviness on the Tensile Response of Lattice Materials." *Journal of Applied Mechanics* 88 (3). https://doi.org/10.1115/1.4049140.

Sercombe, Tim, Noel Jones, Rob Day, and Alan Kop. 2008. "Heat Treatment of Ti-6Al-7Nb Components Produced by Selective Laser Melting." *Rapid Prototyping Journal*. https://doi.org/10.1108/13552540810907974.

Sevilla, P., C. Aparicio, J. A. Planell, and F. J. Gil. 2007. "Comparison of the Mechanical Properties between Tantalum and Nickel–Titanium Foams Implant Materials for Bone Ingrowth Applications." *Journal of Alloys and Compounds* 439 (1–2): 67–73. https://doi.org/10.1016/J.JALLCOM.2006.08.069.

Sing, Swee Leong, Wai Yee Yeong, and Florencia Edith Wiria. 2016. "Selective Laser Melting of Titanium Alloy with 50 Wt% Tantalum: Microstructure and

Mechanical Properties." *Journal of Alloys and Compounds* 660 (March): 461–70. https://doi.org/10.1016/J.JALLCOM.2015.11.141.

Stráský, J., M. Janeček, P. Harcuba, D. Preisler, and M. Landa. 2018. "Biocompatible Beta-Ti Alloys with Enhanced Strength Due to Increased Oxygen Content." *Titanium in Medical and Dental Applications*, January, 371–92. https://doi.org/10.1016/B978-0-12-812456-7.00017-2.

Sundfeldt, Mikael, Lars v Carlsson, Carina B Johansson, Peter Thomsen, and Christina Gretzer. 2006. "Aseptic Loosening, Not Only a Question of Wear: A Review of Different Theories." *Acta Orthopaedica* 77 (2): 177–97. https://doi.org/10.1080/17453670610045902.

Suresh, S. 1998. *Fatigue of Materials*. Cambridge University Press. https://doi.org/10.1017/CBO9780511806575.

Tan, X. P., Y. J. Tan, C. S.L. Chow, S. B. Tor, and W. Y. Yeong. 2017. "Metallic Powder-Bed Based 3D Printing of Cellular Scaffolds for Orthopaedic Implants: A State-of-the-Art Review on Manufacturing, Topological Design, Mechanical Properties and Biocompatibility." *Materials Science and Engineering: C* 76 (July): 1328–43. https://doi.org/10.1016/J.MSEC.2017.02.094.

Tang, Ming, P. Chris Pistorius, and Jack L. Beuth. 2017. "Prediction of Lack-of-Fusion Porosity for Powder Bed Fusion." *Additive Manufacturing* 14 (March): 39–48. https://doi.org/10.1016/J.ADDMA.2016.12.001.

Vanmeensel, K., K. Lietaert, B. Vrancken, S. Dadbakhsh, X. Li, J.-P. Kruth, P. Krakhmalev, I. Yadroitsev, and J. Van Humbeeck. 2018. "Additively Manufactured Metals for Medical Applications." In *Additive Manufacturing*, 261–309. Oxford, UK: Butterworth-Heinemann.

Vanmeensel, Kim, Karel Lietaert, Bey Vrancken, Sasan Dadbakhsh, Xiaopeng Li, Jean Pierre Kruth, Pavel Krakhmalev, Igor Yadroitsev, and Jan van Humbeeck. 2018. "Additively Manufactured Metals for Medical Applications." In *Additive Manufacturing: Materials, Processes, Quantifications and Applications*, 261–309. Butterworth-Heinemann. https://doi.org/10.1016/B978-0-12-812155-9.00008-6.

Vayssette, Bastien, Nicolas Saintier, Charles Brugger, Mohamed Elmay, and Etienne Pessard. 2018. "Surface Roughness of Ti-6Al-4V Parts Obtained by SLM and EBM: Effect on the High Cycle Fatigue Life." *Procedia Engineering* 213: 89–97. https://doi.org/10.1016/j.proeng.2018.02.010.

Veronesi, Francesca, Matilde Tschon, and Milena Fini. 2017. "Gene Expression in Osteolysis: Review on the Identification of Altered Molecular Pathways in

Preclinical and Clinical Studies." *International Journal of Molecular Sciences* 18 (3): 499. https://doi.org/10.3390/ijms18030499.

Vilaro, T, C Colin, and J D Bartout. 2011. "As-Fabricated and Heat-Treated Microstructures of the Ti-6Al-4V Alloy Processed by Selective Laser Melting." *Metallurgical and Materials Transactions A* 42 (10): 3190–99. https://doi.org/10.1007/s11661-011-0731-y.

Vrancken, B., L. Thijs, J. P. Kruth, and J. van Humbeeck. 2014. "Microstructure and Mechanical Properties of a Novel β Titanium Metallic Composite by Selective Laser Melting." *Acta Materialia* 68 (April): 150–58. https://doi.org/10.1016/J.ACTAMAT.2014.01.018.

Wang, Qian, Changjun Han, Tomasz Choma, Qingsong Wei, Chunze Yan, Bo Song, and Yusheng Shi. 2017. "Effect of Nb Content on Microstructure, Property and in Vitro Apatite-Forming Capability of Ti-Nb Alloys Fabricated via Selective Laser Melting." *Materials & Design* 126 (July): 268–77. https://doi.org/10.1016/J.MATDES.2017.04.026.

Wang, Yingjun, Sajad Arabnejad, Michael Tanzer, and Damiano Pasini. 2018. "Hip Implant Design With Three-Dimensional Porous Architecture of Optimized Graded Density." *Journal of Mechanical Design* 140 (11): 111406–13. https://doi.org/10.1115/1.4041208.

Wooley, P H, and E M Schwarz. 2004. "Aseptic Loosening." *Gene Therapy* 11 (4): 402–7. https://doi.org/10.1038/sj.gt.3302202.

Xu, T. W., S. S. Zhang, F. S. Zhang, H. C. Kou, and J. S. Li. 2016. "Effect of ω-Assisted Precipitation on B→α Transformation and Tensile Properties of Ti–15Mo–2.7Nb–3Al–0.2Si Alloy." *Materials Science and Engineering: A* 654 (January): 249–55. https://doi.org/10.1016/J.MSEA.2015.12.052.

Yan, Chunze, Liang Hao, Ahmed Hussein, and David Raymont. 2012. "Evaluations of Cellular Lattice Structures Manufactured Using Selective Laser Melting." *International Journal of Machine Tools and Manufacture* 62 (November): 32–38. https://doi.org/10.1016/j.ijmachtools.2012.06.002.

Yan, Lamei, Youwei Yuan, Linjun Ouyang, Hong Li, Alireza Mirzasadeghi, and Li Li. 2016. "Improved Mechanical Properties of the New Ti-15Ta-XZr Alloys Fabricated by Selective Laser Melting for Biomedical Application." *Journal of Alloys and Compounds* 688 (December): 156–62. https://doi.org/10.1016/J.JALLCOM.2016.07.002.

Yuan, Wei, Wentao Hou, Shujun Li, Yulin Hao, Rui Yang, Lai Chang Zhang, and Yue Zhu. 2018. "Heat Treatment Enhancing the Compressive Fatigue Properties of Open-Cellular Ti-6Al-4V Alloy Prototypes Fabricated by

Electron Beam Melting." *Journal of Materials Science and Technology* 34 (7): 1127–31. https://doi.org/10.1016/j.jmst.2017.12.003.

Zadpoor, Amir A. 2019. "Mechanical Performance of Additively Manufactured Meta-Biomaterials." *Acta Biomaterialia* 85: 41–59. https://doi.org/https://doi.org/10.1016/j.actbio.2018.12.038.

Zafari, Ahmad, Edward Wen Chiek Lui, Mogeng Li, and Kenong Xia. 2022. "Enhancing Work Hardening and Ductility in Additively Manufactured β Ti: Roles Played by Grain Orientation, Morphology and Substructure." *Journal of Materials Science & Technology* 105 (April): 131–41. https://doi.org/10.1016/J.JMST.2021.08.006.

Zhang, X Z, M Leary, H P Tang, T Song, and M Qian. 2018. "Selective Electron Beam Manufactured Ti-6Al-4V Lattice Structures for Orthopedic Implant Applications: Current Status and Outstanding Challenges." *Current Opinion in Solid State and Materials Science* 22 (3): 75–99. https://doi.org/https://doi.org/10.1016/j.cossms.2018.05.002.

Zhou, Libo, Tiechui Yuan, Ruidi Li, Jianzhong Tang, Minbo Wang, and Fangsheng Mei. 2018. "Microstructure and Mechanical Properties of Selective Laser Melted Biomaterial Ti-13Nb-13Zr Compared to Hot-Forging." *Materials Science and Engineering: A* 725 (May): 329–40. https://doi.org/10.1016/J.MSEA.2018.04.001.

Zhou, Ying Long, and Mitsuo Niinomi. 2008. "Microstructures and Mechanical Properties of Ti–50 Mass% Ta Alloy for Biomedical Applications." *Journal of Alloys and Compounds* 466 (1–2): 535–42. https://doi.org/10.1016/J.JALLCOM.2007.11.090.

Zhuravleva, Ksenia, Matthias Bönisch, Konda Gokuldoss Prashanth, Ute Hempel, Arne Helth, Thomas Gemming, Mariana Calin, et al. 2013. "Production of Porous β-Type Ti–40Nb Alloy for Biomedical Applications: Comparison of Selective Laser Melting and Hot Pressing." *Materials* 6 (12): 5700–5712. https://doi.org/10.3390/ma6125700.

Chapter Ⅳ
Conclusion and future perspectives

This study aimed at investigating the physical, mechanical, and biological properties of the β-metastable Ti-21S alloy additively manufactured by L-PBF both as bulk as well as lattices structure. The first part of the study focused on investigating the potential of additively manufactured Ti-21S alloy for biomedical applications. The physical and mechanical properties of the bulk samples (D=12 mm and L=80 mm) fabricated by L-PBF were investigated and this was followed by studying the In vitro biological behavior of coupons samples (D=4 mm and L=10 mm). The main results can be summarized as follows:

- A fully metastable β-structure could be obtained in the as-built state;
- Microstructure analysis highlights the achievement of a near fully dense and defects free material showing a columnar structure oriented along the building direction (BD);
- The elastic modulus measured by tensile test along the building direction is 52 ± 0.3 GPa, i.e., very close to that of bone (30 GPa), and among the lowest reported in literature;
- Quasi-static mechanical properties show a good mechanical strength ($\sigma_{y0.2}$ =709 ± 6 MPa) and excellent ductility (EI =21 ± 1.2 %) along the building direction without the need of heat treatments;
- Fatigue properties improved by reducing the surface roughness so that the fatigue strength of the as-built surface material is lower than surface finished one;
- Viability results showed that experimental and reference samples had higher significant viability than CTR+, and no cytotoxicity was detected.

The second part of the work was addressed to the investigation of the manufacturability of cubic lattice structured in Ti-21S alloy. In this way, the geometrical deviation and morphological investigation were made using the Micro-CT analysis, microstructural investigation, and finite element modeling. The quasi-static and cyclic loading mechanical testing was performed for the manufacturable cell size. Finally, the more complex lattice topology, the octet truss, to be suitable for the biomedical applications fabricated in the same unit cell and the mechanical properties of octet truss topology were investigated. The main conclusions of this part of the work are summarized in the following points:

- The manufacturability was shown that the suitable manufacturing quality is obtained for strut thickness above 0.5 mm and cell size above 4 mm;
- The microstructure of lattice material was similar to that found for the bulk material;
- Main printing defects were reduced by increasing the strut size and cell size;
- FE modeling of the lattice structures highlighted that geometrical imperfections and surface irregularities detrimentally impact the local stress field and that this negative effect is more pronounced at smaller strut thickness (0.26 mm) and unit cell size (1.5 mm);
- The mechanical behavior of the simple cubic and octet truss designs was in good agreement with the stretching dominated and bending dominated mechanism according to the Gibson-Ashby model, respectively;
- The measured elastic modulus for the fixed unit cell size of 4 mm was 2 GPa for the simple cubic (porosity 93%) and 3.5 GPa for the octet truss (porosity 73%) designs, respectively.
- The measured yield stress was 15.47 ± 0.68 MPa for the simple cubic and 50. 91± 0. 88MPa for the octet truss designs, respectively.
- The measured fatigue test was 12 MPa for the simple cubic and 7 MPa for the octet truss designs at the 10^6 cycles, respectively.

In view of results obtained in this study, the potential of Ti-21S alloy as a possible substitute of reference Ti-6Al-4V alloy in biomedical applications could be verified. Both, mechanical and fatigue strength in the as-built state is slightly lower than heat-treated Ti-6Al-4V, while ductility is considerably higher.

Another type of the unit cell topology of the lattice structure of this material should be fabricated for a better understanding of the behavior of this material for the lattices design. In this regard, the TPMS and auxetic topologies aim to fabricate as a future perspective of this study to obtain better properties in the as-built condition. The fatigue behavior of additively manufactured Ti-21S alloy might be of great interest also for some applications, especially for energy absorption applications.

Scientific production

Journal articles

A. Jam, A. du Plessis, C. Lora, S. Raghavendra, M. Pellizzari and M. Benedetti, 2022. *Manufacturability of lattice structures fabricated by laser powder bed fusion: a novel biomedical application of the beta Ti-21S alloy*, Additive Manufacturing, 50, p.102556.

Pellizzari, M., Jam, A., Tschon, M., Fini, M., Lora, C. and Benedetti, M., 2020. *A 3D-printed ultra-low Young's modulus β-Ti alloy for biomedical applications*. Materials, 13(12), p.2792.

Jam, A., Pellizzari, M. and Benedetti, M., 2019. *Laser metal fusion of beta Ti 21S alloy*. Transactions on Additive Manufacturing Meets Medicine, 1(S1), (Abstract).

Pellizzari, M., Jam, A., Tonon, V., Benedetti, M. and Lora, C., 2021. *Ageing behavior of Beta-Ti21S produced by laser powder bed fusion.* Metallurgia Italiana, 113(2), pp. 42–49.

Conferences

A. Jam, A. du Plessis, C. Lora, M. Dellago, M. Pellizzari and M. Benedetti. Non-destructive manufacturability evaluation of additively manufactured β-Ti 21S lattice structures: metrological characterization and image-based simulation. The ASTM International Conference on Additive Manufacturing (ICAM 2021), Invited Talk, Anaheim, USA, November 2021.

Jam, A., Pellizzari, M. and Benedetti, M. *Laser metal fusion of beta Ti 21S alloy*. Additive Manufacturing Meets Medicine Conference, Presentation, Germany, Lubeck, September 2019.

Acknowledgments

I would like to thank my supervisors Prof. Massimo Pellizzari and Prof. Matteo Benedetti for their guidance, mentorship and for sharing their knowledge with me. I am deeply indebted to Prof. Anton Du Plessis who supervised me in this project for the lattice structure section. I would like to extend my sincere thanks to Dr. Carlo Lora and SISMA company for fabricating samples for my PhD project and for dealing with process optimization with extraordinary competence. I gratefully acknowledge the Ntopology and Volume Graphic companies for providing me their softwares which helped me to deeply studied my samples.

I would like to acknowledge the assistance of Dr. Michele Dallago and Dr. Sunil Raghavendra for the simulation part of my project. A special thanks to ing. Lorena Emanuelli and Sasan Amirabdollahian, for their precious assistance during laboratory works, and to all friends who supported me during my PhD program.

Finally, I am extremely grateful to my parents, my sister, and my brothers for their continuous support.

Winter 2022

Ali